

# Study of Nuclear Viscosity and Isospin Mixing utilizing Isovector Giant Dipole Resonance

*By*

DEBASISH MONDAL  
PHYS04201404004

Variable Energy Cyclotron Centre, Kolkata

*A thesis submitted to the  
Board of Studies in Physical Sciences*

*In partial fulfillment of requirements  
for the Degree of*

DOCTOR OF PHILOSOPHY

*of*

HOMI BHABHA NATIONAL INSTITUTE



July, 2017



# Homi Bhabha National Institute

## Recommendations of the Viva Voce Board

As members of the Viva Voce Board Committee, we certify that we have read the dissertation prepared by Shri Debasish Mondal entitled '*Study of Nuclear Viscosity and Isospin Mixing Utilizing Isovector Giant Dipole Resonance*' and recommend that it may be accepted as fulfilling the thesis requirement for the award of Degree of Doctor of Philosophy.

---

Chairman: Dr. D. N. Basu

Date:



09/01/2018

---

Guide/Convener: Dr. S. R. Banerjee

Date:



09/1/2018

---

Member: Dr. C. Bhattacharya

Date:



9.1.2018

---

Member: Prof. Subinit Roy

Date: 9.1.2018



---

External Examiner: Prof. Samit Kumar Mandal

Date: 09/01/2018



Final approval and acceptance of this thesis is contingent upon the candidate's submission of the final copies of the thesis to HBNI.

I hereby certify that I have read this thesis prepared under my direction and recommend that it may be accepted as fulfilling the thesis requirement.

Date: 09/1/2018

Time: 11:30 AM

Guide: \_\_\_\_\_

(Dr. S. R. Banerjee)





## STATEMENT BY AUTHOR

This dissertation has been submitted in partial fulfillment of requirements for an advanced degree at Homi Bhabha National Institute (HBNI) and is deposited in the Library to be made available to borrowers under rules of the HBNI.

Brief quotations from this dissertation are allowable without special permission, provided that accurate acknowledgement of source is made. Requests for permission for extended quotation from or reproduction of this manuscript in whole or in part may be granted by the Competent Authority of HBNI when in his or her judgment the proposed use of the material is in the interests of scholarship. In all other instances, however, permission must be obtained from the author.

DEBASISH MONDAL



## DECLARATION

I, hereby declare that the investigation presented in the thesis has been carried out by me. The work is original and has not been submitted earlier as a whole or in part for a degree / diploma at this or any other Institution / University.

DEBASISH MONDAL



## List of Publications

1. \*‘*Experimental Determination of  $\eta/s$  for Finite Nuclear Matter*’, **Debasish Mondal**, Deepak Pandit, S. Mukhopadhyay, Surajit Pal, Balaram Dey, Srijit Bhattacharya, A. De, Soumik Bhattacharya, S. Bhattacharyya, Pratap Roy, K. Banerjee, and S.R. Banerjee.  
**Phys. Rev. Lett.** **118** (2017) **192501**.
2. ‘*Giant dipole resonance studies in Ba isotopes at  $E/A \sim 5$  MeV*’, C. Ghosh, A.K. Rhine Kumar, Balaram Dey, V. Nanal, R.G. Pillay, P. Arumugam, K.V. Anoop, N. Dokania, Abhijit Garai, Ghnashyam Gupta, E. T. Mirgule, G. Mishra, **Debasish Mondal**, S. Pal, M.S. Pose, and P.C. Rout.  
**Phys. Rev. C** **96** (2017) **014309**.
3. ‘*Signature of clustering in quantum many-body systems probed by the giant dipole resonance*’, Deepak Pandit, **Debasish Mondal**, Balaram Dey, Srijit Bhattacharya, S. Mukhopadhyay, Surajit Pal, A. De, and S.R. Banerjee.  
**Phys. Rev. C** **95** (2017) **034301**.
4. ‘*VECC array for Nuclear fast Timing and angular correlation studies (VENTURE)*’, S.S. Alam, T. Bhattacharjee, D. Banerjee, A. Saha, Deepak Pandit, **Debasish Mondal**, S. Mukhopadhyay, Surajit Pal, P. Bhaskara, S.K. Das, S.R. Banerjee.  
**Nucl. Instr. and Meth. A** **874** (2017) **103**.
5. ‘*Level density and thermodynamics in the hot rotating  $^{96}\text{Tc}$* ’, Balaram Dey, Deepak Pandit, Srijit Bhattacharya, N. Quang Hung, N. Dinh Dang, L. Tan Phuc, **Debasish Mondal**, S. Mukhopadhyay, Surajit Pal, A. De, and S.R. Banerjee.  
**Phys. Rev. C** **96** (2017) **054326**.
6. \*‘*Exclusive Measurement of isospin mixing at high temperature in  $^{32}\text{S}$* ’, **Debasish Mondal**, Deepak Pandit, S. Mukhopadhyay, Surajit Pal, Srijit Bhattacharya, A. De, Soumik Bhattacharya, S. Bhattacharyya, Balaram Dey, Pratap Roy, K. Banerjee, S.R. Banerjee.  
**Phys. Lett. B** **763** (2016) **422**.
7. ‘*Characterization of PARIS  $\text{LaBr}_3(\text{Ce})\text{-NaI}(\text{Tl})$  phoswich detectors up to  $E_\gamma \sim 22$  MeV*’, C. Ghosh, V. Nanal, R.G. Pillay, Anoop K.V., N. Dokania, Sanjoy Pal, M.S. Pose, G. Mishra, P.C. Rout, Suresh Kumar, Deepak

---

\*Related to the thesis

- Pandit, **Debasish Mondal**, Surajit Pal, S.R. Banerjee, Pawel J. Napiorkowski, Oliver Dorvaux, S. Kihel, C. Mathieu, A. Maj.  
**JINST 11 (2016) 05023.**
8. ‘*Experimental investigation of the temperature dependence of nuclear level density parameter*’, Balaram Dey, Deepak Pandit, Srijit Bhattacharya, K. Banerjee, N. Quang Hung, N. Dinh Dang, **Debasish Mondal**, S. Mukhopadhyay, Surajit Pal, A. De, and S. R Banerjee.  
**Phys. Rev. C 91 (2015) 044326.**
  9. ‘*Probing the critical behavior in the evolution of GDR width at very low temperatures at  $A \sim 100$  mass region*’, Balaram Dey, **Debasish Mondal**, Deepak Pandit, S. Mukhopadhyay, Surajit Pal, Srijit Bhattacharya, A. De, K. Banerjee, N Dinh Dang, N Quang Hung and S.R. Banerjee.  
**Phys. Lett. B 731 (2014) 92.**
  10. ‘*Examination of level density prescriptions for the interpretation of high-energy  $\gamma$ -ray spectra*’, Srijit Bhattacharya, Deepak Pandit, Balaram Dey, **Debasish Mondal**, S. Mukhopadhyay, Surajit Pal, A. De and S.R. Banerjee.  
**Phys. Rev. C 90 (2014) 054319.**
  11. ‘*Giant dipole resonance width and the universality of a fluctuation model including critical temperature*’, Deepak Pandit, Srijit Bhattacharya, Balaram Dey, **Debasish Mondal**, S. Mukhopadhyay, Surajit Pal, A. De, and S.R. Banerjee.  
**Phys. Rev. C 88 (2013) 054327.**
  12. ‘*Giant dipole resonance width as a probe for nuclear deformation at finite excitation*’, Deepak Pandit, Balaram Dey, **Debasish Mondal**, S. Mukhopadhyay, Surajit Pal, Srijit Bhattacharya, A. De, and S.R. Banerjee.  
**Phys. Rev. C 87 (2013) 044325.**
  13. ‘*Neutron response of the LAMBDA spectrometer and neutron interaction length in  $BaF_2$* ’, Balaram Dey, **Debasish Mondal**, Deepak Pandit, S. Mukhopadhyay, Surajit Pal, K. Banerjee, Srijit Bhattacharya, A. De, and S.R. Banerjee.  
**Nucl. Instr. and Meth. A 727 (2013) 7.**

DEBASISH MONDAL

## DEDICATIONS

To My Teachers



## ACKNOWLEDGEMENTS

I would like to extend my sincere gratitude to my thesis supervisor Prof. Sudhee Ranjan Banerjee for his constant support, guidance and encouragement throughout the course of this work. His logical way of tackling the problems helped me a lot in circumventing the difficulties with ease.

I owe the most sincere thanks to my laboratory colleagues cum elder brothers Dr. Surajit Pal, Dr. Supriya Mukhopadhyay, Dr. Deepak Pandit, Dr. Balaram Dey, Dr. Alok Kumar De and Dr. Srijit Bhattacharya for presenting me a scientific and friendly ambience without which the work would not have been possible.

I thankfully appreciate the contributions of my other collaborators Dr. Sarmistha Bhattacharyya, Dr. Kaushik Banerjee and Dr. Pratap Roy and Soumik Bhattacharya.

I thankfully acknowledge the inputs of Dr. D. N. Basu, Dr. Chandana Bhattacharya and Dr. Subinit Roy during the course of the work.

I would like to express my sincere gratitude to Shri Amitava Roy, Director, VECC, for his continuous support. My special thanks Dr. Sailajananda Bhattacharya, Dr. V. S. Pandit, Dr. Gopal Mukherjee, Dr. Tilak Kumar Ghosh, Dr. Tumpa Bhattacharya, Dr. Samir Kundu, Dr. Tapan K. Rana, Dr. Jhilam Sadhukhan, Ratnesh Pandey, Santu Manna and Asim Pal for their valuable inputs and suggestions.

I appreciate the assistance of Partha Dhara, Partha Bhaskar, Anindita Choudhury and Imran Shaik throughout the course of the work.

I thankfully acknowledge the discussions with Prof. Dinesh K. Srivastava, Prof. Jan-e Alam and Dr. Shashi C. L. Srivastava regarding the viscosity of finite nuclear matter.

I deeply appreciate the contributions of Dr. D. P. Chowdhury, Dr. Jagannath Datta, Rathin Saha, A. A. Mallick, Jaykiran Meena and Ratan Barai in preparation and thickness measurement of Silicon target.

I thank the VECC cyclotron operators, scientific and technical staffs for uninterrupted supply of beams during the experiments.

I tender my thanks to Dr. Anna Maria Corsi for providing the isospin included CASCADE code originally obtained from Prof. M. Kicinska-Habior. I also owe sincere gratitude to Dr. John Behr for providing me with his PhD thesis which has helped me a lot in understanding the topic of isospin mixing in detail. I sincerely acknowledge the discussions via e-mail with Prof. M. N. Harakeh regarding isospin mixing in nuclei.

I take this opportunity to express my heartfelt gratitude to my teachers Pradeep sir, Uttam sir, Bhaskar sir, Jasim sir, Maleque sir, Dulal sir and Shibu sir, Rajen sir and Sharad sir for inculcating the scientific attitudes which helped me in achieving my goal.

Finally, it is needles to mention that without the unconditional love and support of my parents and my sister, it would not have been possible to achieve my goal. I heartily thank my wife Supriya for her continuous love, support and encouragement.

# Contents

<b>SYNOPSIS</b>	<b>xvii</b>
<b>LIST OF FIGURES</b>	<b>xxxix</b>
<b>LIST OF TABLES</b>	<b>xxxv</b>
<b>1 Introduction</b>	<b>1</b>
1.1 The concept of nuclear temperature . . . . .	4
1.2 Giant resonances and their classifications . . . . .	6
1.3 The isovector giant dipole resonance (IVGDR) . . . . .	8
1.3.1 IVGDR built on ground state of nucleus . . . . .	8
1.3.2 IVGDR built on excited state of nucleus . . . . .	11
<b>2 Viscosity and Entropy Density</b>	<b>15</b>
2.1 Viscosity of a fluid . . . . .	15
2.2 Entropy and entropy density . . . . .	17
2.3 Ratio of shear viscosity to the entropy density ( $\eta/s$ ) . . . . .	18
2.3.1 Importance of ( $\eta/s$ ) . . . . .	19
2.4 $\eta/s$ for finite nuclear matter . . . . .	22
2.4.1 Shear viscosity and giant resonances . . . . .	23
2.5 Motivation of the present work . . . . .	27
<b>3 Isospin Formalism and Isospin Mixing</b>	<b>29</b>
3.1 Isospin formalism . . . . .	29

3.2	Isospin mixing . . . . .	30
3.2.1	Expected variation of isospin mixing with excitation energy or temperature . . . . .	31
3.2.2	Calculations of isospin mixing . . . . .	33
3.2.3	Importance of isospin mixing . . . . .	36
3.2.4	Tools for measurement of isospin mixing . . . . .	39
3.3	Isospin selection rule for IVGDR $\gamma$ ray transitions . . . . .	39
3.4	Isospin splitting and Pauli blocking of GDR strength . . . . .	40
3.5	Previous experimental works and motivation for the present work	42
<b>4</b>	<b>Statistical Model Calculations</b>	<b>45</b>
4.1	Compound nucleus formation . . . . .	46
4.2	Compound nucleus decay . . . . .	47
4.3	Nuclear level density . . . . .	49
4.4	Isospin and parity in statistical model calculations . . . . .	51
4.4.1	Isospin dependence of nuclear level density . . . . .	52
4.4.2	Isospin mixing in the statistical model calculations . . . . .	52
<b>5</b>	<b>Experimental Details and Simulation Studies</b>	<b>55</b>
5.1	High-energy $\gamma$ ray detectors . . . . .	56
5.2	The LAMBDA spectrometer . . . . .	58
5.2.1	Fabrication and properties of individual detectors . . . . .	59
5.2.2	Calibration of the LAMBDA spectrometer . . . . .	59
5.2.3	Response of the LAMBDA spectrometer . . . . .	61
5.3	Multiplicity filter . . . . .	63
5.3.1	Mapping of fold distribution into angular momentum space	65
5.4	Neutron time of flight detector . . . . .	67
5.5	Experimental details . . . . .	68
5.5.1	Detector set-up . . . . .	69
5.5.2	Electronics set-up for $\gamma$ ray measurements . . . . .	70
5.5.3	Electronics set-up for neutron measurements . . . . .	73

5.6	Data reduction for high-energy $\gamma$ rays . . . . .	74
5.6.1	Rejection of neutron background . . . . .	74
5.6.2	Rejection of pile-up events . . . . .	75
5.6.3	Rejection of cosmic backgrounds . . . . .	76
5.6.4	Data reconstruction . . . . .	78
5.7	Data reduction for neutrons . . . . .	80
<b>6</b>	<b><math>\eta/s</math> for Finite Nuclear Matter: Experiments, Results, and Discussions</b>	<b>83</b>
6.1	Experimental details and data reduction . . . . .	84
6.2	Extraction of NLD and GDR parameters . . . . .	86
6.3	Determination of the shear viscosity . . . . .	91
6.4	Determination of the entropy density . . . . .	93
6.5	Results and discussions . . . . .	94
<b>7</b>	<b>Isospin Mixing in <math>^{32}\text{S}</math>: Experiments, Results, and Discussions</b>	<b>99</b>
7.1	Preparation of Silicon target . . . . .	100
7.2	Experimental details and data reduction . . . . .	101
7.3	Extraction of NLD, GDR and isospin mixing parameters . . . . .	101
7.4	Results and discussions . . . . .	108
7.4.1	Comparison with the calculation at high temperature . . . . .	111
<b>8</b>	<b>Summary, Conclusion and Outlook</b>	<b>115</b>
	<i>Bibliography</i> . . . . .	119



# SYNOPSIS

Atomic nucleus is a many body quantum system, which, by the virtue of its intrinsic complexity, mystery and practical applications, remains an exciting entity for physicists. Over the years, various tools have been unearthed to explore deep into the nucleus and study its properties. The isovector giant dipole resonance (IVGDR), a member of a broader family of collective resonances known as giant resonances, is an excellent tool to explore the nuclear properties at extreme conditions. Macroscopically described as the out of phase oscillation of proton and neutron fluids, the IVGDR is a highly damped motion characterized by very short lifetime ( $\sim 10^{-21}$ - $10^{-22}$  sec). The resonance relaxes by the emission of high-energy  $\gamma$  rays in 10-25 MeV region depending on the mass of the system. Viscosity of the nuclear matter provides the main mechanism for the damping of IVGDR and it is inherently related to the width ( $\Gamma$ ) and energy of the resonance [Aue75]. Also, these  $\gamma$ -transitions, being isovector in nature, are inhibited between the states of the same isospin ( $I$ ) in self-conjugate nuclei [Wil69]. This thesis presents two crucial properties of the nucleus at finite temperature utilizing the above mentioned aspects of the IVGDR. The first part presents the crucial ratio of shear viscosity ( $\eta$ ) to entropy density ( $s$ ) for equilibrated finite nuclear matter from  $A \sim 30$  to  $A \sim 208$  at different temperatures, while the second part deals with the experimental study of isospin mixing at high temperature in  $^{32}\text{S}$ .

The ratio of shear viscosity ( $\eta$ ) to entropy volume density ( $s$ ) has been the subject of intense investigations in different areas of physics. It is well defined for both relativistic and non-relativistic fluids and is important in connection with the physics of black hole, quark-gluon plasma and the low temperature quantum

fluids. The ratio  $\eta/s$  provides the crucial signature of liquid-gas phase transition in matter. String theoretical calculations have put a universal lower bound, known as the Kovtun-Son-Starinets (KSS) bound, such that  $\eta/s \geq \hbar/4\pi k_B$ ,  $k_B$  being the Boltzmann constant [Kov05]. The KSS conjecture has attracted a lot of theoretical and experimental efforts in different areas of physics. People have tried to find out whether there exists a perfect fluid and whether they follow the KSS conjecture. Although, there are some theoretical counterexamples [Coh07, Cre11], no fluid that violates the KSS conjecture has been found experimentally. Moreover, it is observed that strongly coupled systems such as low-temperature quantum fluids and high-temperature quark-gluon plasma (QGP) have very small  $\eta/s$  ( $\sim 5-10 \hbar/4\pi k_B$ ) characteristic of a near-perfect fluid [Sch09].

The nucleons in the nucleus are governed by strong interaction and show highly correlated behavior. Finite nucleus, therefore, is an ideal system to search for near perfect fluidity in matter. Different model dependent calculations for  $\eta/s$  have been performed earlier at intermediate-energy heavy ion collisions in search for a liquid-gas phase transition [Pal10, Li11, Zho13, Fan14, Den16]. The first theoretical study for  $\eta/s$ , in relation to the damping of giant resonances in nuclei, was done by Auerbach and Shlomo [Aue09] within the frame work of Fermi liquid drop model (FLDM). They showed that  $\eta/s$  values for heavy and light nuclei were  $\sim (4-19) \hbar/4\pi k_B$  and  $(2.5-12.5) \hbar/4\pi k_B$ , respectively. Recently, Dang has proposed a formalism, based on the Green-Kubo relation and the fluctuation dissipation theorem, relating the shear viscosity to the width and the energy of giant dipole resonance (GDR) in hot finite nuclei [Dan11]. The empirically calculated values of  $\eta/s$  for different systems have been compared by the author with various model dependent calculations. A model independent high temperature limit of  $\eta/s$  has also been proponed for finite nuclear systems.

According to this formalism

$$\eta(T) = \eta(0) \frac{\Gamma_{\text{GDR}}(T)}{\Gamma_{\text{GDR}}(0)} \left\{ \frac{E_{\text{GDR}}(0)^2}{E_{\text{GDR}}(0)^2 - [\Gamma_{\text{GDR}}(0)/2]^2 + [\Gamma_{\text{GDR}}(T)/2]^2} \right\}^2 \quad (1)$$

where  $\eta(0)$  is the shear viscosity at zero temperature,  $\Gamma_{\text{GDR}}(0)$  and  $E_{\text{GDR}}(0)$  are the ground state GDR width and energy, respectively and  $\Gamma_{\text{GDR}}(T)$  is width of the GDR built on the state of excitation energy corresponding to temperature  $T$ .

According to the Fermi gas model the entropy density is given by

$$s(T) = \frac{\rho}{A} S(T) \quad (2)$$

where  $A$  is the nuclear mass number, nuclear density  $\rho = 0.16 \text{ fm}^{-3}$ , and the entropy  $S(T) = 2a(T)T$ . Here  $T$  is the nuclear temperature and  $a(T)$  is the nuclear level density (NLD) parameter at temperature  $T$ .

In this thesis, simultaneous measurements of the GDR widths and energies, required for the determination of  $\eta(T)$ , with the NLD parameters and nuclear temperatures, required for the extraction of  $s$  are presented at four different mass regions, namely  $^{31}\text{P}$ ,  $^{97}\text{Tc}$ ,  $^{119}\text{Sb}$ , and  $^{201}\text{Tl}$ . A set of experiments were performed at the Variable Energy Cyclotron Centre (VECC), Kolkata using  $\alpha$  beams from the K-130 cyclotron. The nuclei  $^{31}\text{P}$ ,  $^{97}\text{Tc}$ ,  $^{119}\text{Sb}$  and  $^{201}\text{Tl}$  were populated at different excitation energies by bombarding  $\alpha$  beam of energies 28-50 MeV on  $^{27}\text{Al}$ ,  $^{93}\text{Nb}$ ,  $^{115}\text{In}$ ,  $^{197}\text{Au}$  targets, respectively. The high-energy  $\gamma$  rays from the decay of the GDR were measured by a part of the LAMBDA spectrometer [Sup07]. A 50-element multiplicity filter [Dee10] was used to measure the compound nuclear angular momentum (by measuring the number of low-energy  $\gamma$  ray multiplicity or fold) in an event-by-event mode. Proper determination of angular momentum is crucial for a precise evaluation of nuclear temperature which, in turn, is important for extraction of entropy density. The cyclotron RF

time spectrum was also recorded with respect to the multiplicity filter to ensure the selection of beam-related events. The angular distributions of high-energy  $\gamma$  spectra were also measured for  $^{31}\text{P}$  and  $^{119}\text{Sb}$  at  $E_{\text{beam}} = 42$  MeV. Different angular-momentum-gated high-energy  $\gamma$  spectra were reconstructed in the off-line analysis by the cluster summing technique. The neutron and the pile-up events were rejected by time of flight (TOF) and pulse shape discrimination (PSD) techniques, respectively. Evaporated neutron energy spectra were measured, in coincidence with the multiplicity  $\gamma$  rays, by a liquid-scintillator-based neutron TOF detector [Kau09]. The  $n - \gamma$  discrimination was accomplished following the PSD technique comprising of TOF and zero cross-over time (ZCT). The measured TOF spectra were converted to neutron energy spectra by taking the prompt  $\gamma$  peak as a time reference.

The measured fold distributions were mapped onto the angular momentum space by a realistic technique based on GEANT4 simulations. Different fold-gated angular momentum distributions were simulated and incorporated in a modified version of the statistical model code CASCADE [Pul77]. It has experimentally been observed that the asymptotic NLD parameter ( $\tilde{a}$ ) depends on the angular momentum [Pra13]. Therefore,  $\tilde{a}$  were extracted by comparing the different fold-gated neutron energy spectra, with the CASCADE predictions properly corrected for detector efficiency. Simultaneously, the calculated high-energy  $\gamma$  spectra, along with a bremsstrahlung component parameterized as  $\sigma = \sigma_0 \exp(-E_\gamma/E_0)$ , were folded with the detector response function and compared with the experimental spectra to extract the GDR parameters. The center of mass (c.m.)  $\gamma$ -ray angular distribution was assumed to have the form  $W(E_\gamma, \theta) = W_0(E_\gamma)[1 + a_1(E_\gamma)P_1(\cos \theta) + a_2(E_\gamma)P_2(\cos \theta)]$  and the bremsstrahlung slope parameter  $E_0$  was deduced by comparing the experimentally measured  $a_1(E_\gamma)$  with the theoretically calculated ones. The extracted slope parameters were consistent with

the systematics  $E_0 = 1.1[(E_{\text{beam}} - V_c)/A_p]^{0.72}$ , where  $V_c$  is the Coulomb barrier and  $A_p$  is the projectile mass [Nif90]. This systematics was utilized at other beam energies for which angular distributions were not measured. The shear viscosity was deduced from measured GDR parameters by using Eq. (1).  $\eta(0)$  was taken  $1u$  where  $u = 10^{-23}$  MeV·s·fm<sup>-3</sup>. The justification for taking this value for  $\eta(0)$  lies in the fact that the ground state GDR widths for the four nuclei studied were reproduced well by the formulation of Auerbach *et al.* [Aue75] which was derived using  $\eta(0) = 1u$ . An uncertainty in  $\eta(0)$  has also been derived from the mass dependence of the ground state GDR width. The entropy density was extracted from measured level density parameter and nuclear temperature by using Eq. (2). Nuclear temperature was calculated by using the relation  $T = \sqrt{U/a(T)}$ , where  $U = E^* - E_{\text{GDR}} - E_{\text{rot}} - \Delta P$ ;  $E^*$ ,  $E_{\text{GDR}}$ ,  $E_{\text{rot}}$ , and  $\Delta P$  being the initial excitation energy, GDR energy, average rotational energy, and the pairing energy, respectively. Thus, by calculating  $\eta$  and  $s$  at a given temperature,  $\eta/s$  was deduced by taking the ratio of these two quantities.

The deduced shear viscosities are well reproduced for the systems by the calculations based on the generalized Fermi liquid drop model (FLDM) [Aue09, Kol04]. The model directly calculates  $\eta$  by utilizing two-body collisional approach and gives  $\eta(T) = \frac{2}{5}\rho\epsilon_F\tau_{\text{coll}}/[1 + (\omega\tau_{\text{coll}})^2]$ , where  $\epsilon_F$  is the Fermi energy,  $\omega$  is the angular frequency of excitation and  $\tau_{\text{coll}}$  is the collision relaxation time given by  $\tau_{\text{coll}} = \tau_0/[1 + (\hbar\omega/2\pi T)^2]$ ,  $\tau_0 = \hbar\alpha/T^2$ . The parameter  $\alpha$  depends on in-medium nucleon-nucleon scattering cross section and for isovector resonances, its value is 4.6 MeV. The theoretical results are obtained using the values of  $\epsilon_F = 37$  MeV corresponding to  $\rho = 0.16$  fm<sup>-3</sup> and considering  $\hbar\omega$  as the average GDR energy. It is observed that at low temperatures,  $\eta$  increases with the increase in  $T$ , which can be understood qualitatively by the following arguments. For an equilibrated nucleus, the momentum is transported by the

nucleons. The kinetic theoretical calculations give  $\eta \sim \bar{v}\lambda$ , where  $\bar{v}$  is the average velocity of the nucleons and the mean free path  $\lambda \sim \bar{v}/N_{\text{coll}}$ . In rare collision region, which corresponds to the giant resonances, the collision frequency  $N_{\text{coll}}$  does not change much with temperature, while  $\bar{v} \sim \sqrt{T}$ . Therefore, the mean free path as well as the nucleon momentum increases with temperature. That means the momentum can be transported more efficiently over a large distance, thereby increasing  $\eta$  with temperature. The measured entropy densities are well reproduced by the calculations.  $s(T)$  is estimated utilizing the relation  $s(T) = -\frac{\rho}{A} \times \sum_i [f_i \ln(f_i) + (1 - f_i) \cdot \ln(1 - f_i)]$ , where  $f_i$  is the occupation probability of the state with energy  $e_i$  given by  $f_i = [1 + \exp\{(e_i - \mu)/T\}]^{-1}$ . The chemical potential  $\mu$  is calculated from particle conservation, and the single particle energies  $e_i$  are calculated using the deformed Wood Saxon potential with the universal parameters [Cwi87]. As the temperature increases, the distortion of the Fermi surface becomes larger, thereby increasing the number of accessible microstates. This results in the increase of entropy density with temperature.

The deduced  $\eta/s$  shows a mild decrease with the increase in temperature. Moreover, it is confined in the range (2.5-6.5)  $\hbar/4\pi k_B$  for the finite nuclear matter within the temperature range  $\sim$  (0.8-2.1) MeV. Therefore, it could be concluded that nuclear matter obeys the KSS conjecture. Also, the measured values of  $\eta/s$  are comparable to that of the QGP. It, therefore, could be reaffirmed experimentally, that the strong fluidity is a universal characteristic feature of the strong interaction of the many-body nuclear systems and not just of the state created in the relativistic collisions. Although  $\eta$  shows a slight increase with the mass number at the highest available temperature for heavier nuclei,  $\eta/s$  remains within (5.1-6.5)  $\hbar/4\pi k_B$  and (4.6-6.1)  $\hbar/4\pi k_B$  at the lowest and highest available temperatures, respectively, for all nuclei. This indicates that  $\eta/s$  is approximately independent of the nuclear size and the neutron-proton

asymmetry at a given temperature. However, it could be the artefact of incorporating the same  $\eta(0)$  for all nuclei. Also owing to large errors, the data are not sensitive enough to draw any conclusion.

The second part of the present thesis deals with the experimental study of isospin mixing at high temperature in  $^{32}\text{S}$ . The hadronic part of nuclear interactions preserves the isospin quantum number. However, the presence of electromagnetic interactions and the charge dependent short range potential breaks the isospin symmetry. The prime isospin violating term is the isovector Coulomb interaction that mixes states separated by  $\Delta I = 1$ . The importance of isospin mixing lies in connection with two basic phenomena in physics. The first one is the spreading width of the isobaric analog states, which is directly related to the isospin mixing in parent nuclei [Suz96, Sag98]. The second and most important one is the experimental determination of isospin symmetry breaking correction ( $\delta_c$ ) in the measured  $ft$  value of  $J^\pi = 0^+ \rightarrow 0^+$  superallowed Fermi  $\beta$ -decay. The measured  $ft$  value, after correcting for the isospin symmetry breaking and radiative corrections, is utilized to extract the up quark to down quark transition matrix element ( $V_{ud}$ ) in the Cabibbo-Kobayashi-Maskawa (CKM) matrix [Har05a, Tow10, Har15] and hence plays a crucial role in determining the unitarity of CKM matrix.

In general, isospin mixing can be studied by utilizing the transitions that would have been forbidden in the absence of isospin mixing. The E1  $\gamma$ -transition originating from the decay of IVGDR is one such transition that have been employed to study isospin mixing in self-conjugate compound nuclei populated through the self-conjugate entrance channel. Since the lifetime of the compound nucleus is large compared to the time scale of IVGDR, it can probe the evolution of compound nuclear state in the isospin degree of freedom. At

moderate excitations, the  $\gamma$  rays associated with the decay of the IVGDR are emitted from the first few stages of the compound nuclear decay. So, if a self-conjugate nucleus is populated by bombarding a self-conjugate projectile on a self-conjugate target, only  $I = 0$  states are populated in the compound nucleus with the assumption that isospin is fully conserved. Since the E1  $\gamma$ -transitions between the states of the same isospin are prohibited in self-conjugate nuclei, only the transitions between  $I = 0$  to  $I = 1$  states are allowed. However, at moderate excitation energies the density of  $I = 1$  states to be populated by the IVGDR  $\gamma$ -decay are small. This results in the suppression of the yield of IVGDR  $\gamma$  rays decaying from self-conjugate nuclei populated through  $I = 0$  entrance channel as compared to  $I \neq 0$  nuclei for which all transitions are allowed. However, in presence of an admixture of  $I = 1$  states in the initial compound nucleus, the IVGDR  $\gamma$ -yield is enhanced as these  $I = 1$  states can decay to  $I = 0$  states.

The above technique was first utilized by Harakeh *et al.* [Har86] and later it was modified by Behr *et al.* [Beh93]. The statistical model code CASCADE was modified to include the isospin mixing according to the formalism of Harney *et al.* [Hrn86] who parameterized the isospin mixing probability in terms of Coulomb spreading width ( $\Gamma^\downarrow$ ) and compound nuclear decay width ( $\Gamma^\uparrow$ ). By inclusive measurement of IVGDR  $\gamma$  rays, Behr could infer that for  $^{28}\text{Si}$ , isospin becomes a good quantum number with the increase in excitation energy ( $E^*$ ). However, for  $^{26}\text{Al}$ , though with large errors, reverse phenomenon was observed. Recently, isospin mixing has been measured in  $^{80}\text{Zr}$  in exclusive experiments by Corsi *et al.* [Cor11] and Ceruti *et al.* [Cer15]. They concluded that isospin indeed becomes a good quantum number with the increase in temperature and the Coulomb spreading width remains constant with temperature. The result matches well with the only available calculation of Sagawa *et al.* [Sag98] at fi-

nite temperature; also when extrapolated to zero temperature, the result is well reproduced by the recent calculation of Satula *et al.* [Sat09]. However, at lower mass region the measured isospin mixing seems to be large at higher temperature. It should be pointed out that in all previous measurements heavy ion fusion reactions were used to ensure the statistical nature of the evaporated  $\gamma$  rays. However, in such reactions the compound nuclei are populated at higher angular momentum which affect the high-energy  $\gamma$  ray spectrum, particularly at lower mass region. In addition, in the previous measurements at lower mass region the nuclear level density (NLD) parameter which is vital for statistical model calculation and for precise determination of nuclear temperature was not measured. This calls for more advanced, exclusive experiments to be performed at lower mass region to have a comprehensive picture of the temperature variation of isospin mixing at low mass region.

In this thesis, we present exclusive measurement of isospin mixing at  $T = 2.6$  MeV for  $^{32}\text{S}$ . The compound nucleus populated with light ion ( $\alpha$ ) induced fusion reaction to minimize the angular momentum effect. The compound nuclear angular momentum was measured by measuring the low-energy  $\gamma$  ray multiplicity in coincidence with the high-energy IVGDR  $\gamma$  rays. The NLD parameter was also extracted by measuring the evaporated neutron energy spectrum. The simultaneous measurements of angular momentum and NLD parameter enabled us to determine the precise nuclear temperature. Finally, our result was compared with the calculations of Sagawa *et al.* and was extrapolated to zero temperature.

The experiments were performed at the Variable Energy Cyclotron Centre (VECC), Kolkata. The compound nuclei  $^{31}\text{P}$  and  $^{32}\text{S}$  were populated at the same excitation energy ( $E^* = 40.2$  MeV) and angular momentum ( $\langle J \rangle = 12\hbar$ )

through  $I = 1/2$  and  $I = 0$  entrance channels by bombarding self-supporting  $^{27}\text{Al}$  ( $I = 1/2$ ) and  $^{28}\text{Si}$  ( $I = 0$ ) target nuclei with  $\alpha$ -beam ( $I = 0$ ) of energies 35 MeV and 38 MeV, respectively from K-130 Cyclotron. Here  $^{31}\text{P}$  was populated as a reference nucleus (populated through different entrance channel isospin but at the same  $E^*$  and  $\langle J \rangle$ ) to find the IVGDR parameters to be used for the analysis of  $^{32}\text{S}$ . As the masses of the two compound nuclei are nearly the same and they are populated at the same excitation energy and angular momentum, IVGDR parameters are expected to be the same for both the nuclei. It should also be mentioned that the critical angular momentum ( $J_c$ ) [Kus98], above which noticeable effect of  $J$  on IVGDR width is observed, is  $11\hbar$  for  $^{32}\text{S}$ . Consequently, the high-energy  $\gamma$  ray spectra are expected to be sensitive to temperature only.

The experimental procedure and data reduction technique were the same as mentioned earlier. The experimentally measured fold distribution was mapped onto angular momentum space with Monte Carlo GEANT4 simulations and the simulated fusion cross section was incorporated in the a modified version of statistical model code CASCADE in which isospin quantum number was properly taken care of. Two types of pure isospin states  $I_< \equiv |I, I = I_z\rangle$  and  $I_> \equiv |I + 1, I = I_z\rangle$  were considered where  $I_z = (N-Z)/2$  and mixing was performed between them. The fraction of  $\supseteq$  states that mixes with  $\lesseqgtr$  states was defined as

$$\alpha_{\supseteq}^2 = \frac{\Gamma_{\supseteq}^{\downarrow}/\Gamma_{\supseteq}^{\uparrow}}{1 + \Gamma_{\supseteq}^{\downarrow}/\Gamma_{\supseteq}^{\uparrow} + \Gamma_{\lesseqgtr}^{\downarrow}/\Gamma_{\lesseqgtr}^{\uparrow}} \quad (3)$$

The mixed populations of the compound nuclear states were defined as

$$\tilde{\sigma}_{<} = (1 - \alpha_{<}^2)\sigma_{<} + \alpha_{>}^2\sigma_{>} \quad (4)$$

$$\tilde{\sigma}_{>} = (1 - \alpha_{>}^2)\sigma_{>} + \alpha_{<}^2\sigma_{<} \quad (5)$$

where  $\sigma_{<}$  and  $\sigma_{>}$  are the population of the pure isospin states. The level density of each type of isospin states was accounted for and the isospin Clebsch-Gordan

was multiplied with the transmission coefficient. The calculation contains only  $\Gamma_{>}^{\downarrow}$  as the free parameter which has to be derived from the experimental data.

The statistical model analysis for  $^{31}\text{P}$  was performed with the assumption that the isospin is fully conserved ( $\Gamma_{>}^{\downarrow} = 0$ ). The CASCADE neutron spectrum (after correcting for detector efficiency calculated using GEANT4 simulations) was compared with the experimental spectrum and  $\chi^2$  minimization was done in the energy range 4.0 - 10.0 MeV. The Reisdorf level density prescription was used and the best fit was obtained for  $\tilde{a} = 4.2 \pm 0.3 \text{ MeV}^{-1}$ . Similar analysis resulted in  $\tilde{a} = 3.9 \pm 0.1 \text{ MeV}^{-1}$  for  $^{32}\text{S}$ . In the next step, the IVGDR parameters were extracted by comparing the high-energy  $\gamma$  ray spectrum of  $^{31}\text{P}$  with the CASCADE calculations along with a small bremsstrahlung component parameterized as  $\sigma = \sigma(0)e^{-E_{\gamma}/E_0}$ . The slope parameter  $E_0 = 4.9 \text{ MeV}$  is consistent with the parameterization  $E_0 = 1.1[(E_{\text{beam}} - V_c)/A_p]^{0.72}$  [Nif90]. The deduced parameters were  $E_{\text{GDR}} = 17.8 \pm 0.2 \text{ MeV}$ ,  $\Gamma_{\text{GDR}} = 8.0 \pm 0.4 \text{ MeV}$  and  $S_{\text{GDR}} = 1.00 \pm 0.03$ . The uncertainties were obtained by  $\chi^2$  minimization procedure in the energy range 14 - 21 MeV. Finally, the isospin mixing parameters were deduced utilizing the IVGDR parameters extracted from  $^{31}\text{P}$ . In order to increase the sensitivity of isospin mixing and minimize the effects of statistical model parameters, isospin mixing was deduced from the ratio of  $\gamma$  ray cross sections of  $^{32}\text{S}$  and  $^{31}\text{P}$  in the GDR region. We remark here that though we could simulate the response function of LAMBDA spectrometer, the absolute efficiency ( $\epsilon_{in}$ ) of the array is not known. Therefore, we have taken the ratio of  $[\sigma_{\gamma} \times \epsilon_{in}]$  for both the nuclei and compared with the ratio of CASCADE cross-sections properly folded with the detector response function. The absolute values input channel fusion cross sections were calculated using PACE4 code. It should be highlighted here that  $\Gamma_{>}^{\downarrow}$  was the only parameter that was varied to match the experimental ratio with the CASCADE prediction. As  $\Gamma_{>}^{\downarrow}$  remains nearly temperature inde-

pendent, the same  $\Gamma_{>}^{\downarrow}$  was used for all the decay steps. The best value for  $\Gamma_{>}^{\downarrow}$  was obtained by  $\chi^2$  minimization technique in the energy range 14 - 21 MeV and was found to be  $24 \pm 13$  keV corresponding to the average  $\alpha_{<}^2 = 3.5 \pm 1.8$  % at  $T = 2.6$  MeV. It should be mentioned that  $\alpha_{<}^2$  depends on  $J$  and our quoted value corresponds to  $\langle J \rangle = 12\hbar$ . The temperature was calculated using the relation  $T = \sqrt{(E^* - E_{\text{rot}} - \Delta P)/\tilde{a}}$ , where  $E_{\text{rot}}$  is the rotational energy and  $\Delta P$  is the pairing energy. The quoted errors correspond to the statistical errors as well as systematic errors owing to the presence of isotopic impurity in the  $^{28}\text{Si}$  target and the uncertainty in the determination of bremsstrahlung component.

The present results have been compared with the only reported measurement for  $^{32}\text{S}$  for which  $\Gamma_{>}^{\downarrow}$  was  $20 \pm 25$  keV and  $\alpha_{<}^2$  was  $1.3 \pm 1.5\%$  at  $T = 2.85$  MeV [Hab04]. It emphasizes the fact that  $\Gamma_{>}^{\downarrow}$  indeed remains constant with temperature. It is also fascinating to note that  $\alpha_{<}^2$  decreases with the increase in temperature. This is owing to the fact that the competition between the time scale associated with the Coulomb spreading width ( $\Gamma^{\downarrow}$ ) and the compound nuclear decay width ( $\Gamma^{\uparrow}$ ) leads towards the restoration of isospin symmetry. The intrinsic decay width of the compound nuclear state becomes so large as compared to the Coulomb spreading width that the state does not get sufficient time to mix. However, in both the cases angular momenta were different and it would be interesting to disentangle the effects of  $J$  and  $T$  on  $\alpha_{<}^2$ . It could also be conjectured that  $\Gamma_{>}^{\downarrow}$  does not change much with angular momentum.

The measured  $\alpha_{>}^2$  at minimum angular momentum ( $1\hbar$ ) has also been compared with the calculation of Sagawa *et al.* [Sag98]. According to the formalism

$$\alpha_{>}^2 = \frac{1}{I_z + 1} \frac{\Gamma_{\text{IAS}}}{\Gamma_{\text{CN}} + \Gamma_{\text{IVM}}} \quad (6)$$

where  $\Gamma_{\text{IAS}}$  is the spreading width of the IAS, which is equivalent to  $\Gamma_{>}^{\downarrow}$ ,  $\Gamma_{\text{CN}}$

is the compound nuclear decay width and  $\Gamma_{\text{IVM}}$  is the width of the isovector monopole (IVM) state at the energy of IAS.  $\alpha_{>}^2$  was set at 0.7% at  $T = 0$  from the recent calculation of Satula *et al.* [Sat09] This results in  $\Gamma_{\text{IVM}} = 3.4$  MeV as  $\Gamma_{\text{CN}} = 0$  at  $T = 0$ . Next,  $\Gamma_{\text{CN}}$  was calculated using the CASCADE code at different temperatures using our best fit parameters.  $\Gamma_{\text{IVM}}$  was assumed temperature independent and  $\Gamma_{>}^{\downarrow}$  was given a weak linear dependence on  $T$  as  $\Gamma_{>}^{\downarrow}(T) = \Gamma_{>}^{\downarrow}(0)(1+cT)$  where  $c = 0.2 \text{ MeV}^{-1}$ . The parameter  $c$  was calculated by assuming that  $\Gamma_{>}^{\downarrow}(T = 2.6 \text{ MeV}) = 37 \text{ keV}$  i.e.  $\Gamma_{>}^{\downarrow}$  remained within the experimental error bar. It is observed that our measured  $\alpha_{>}^2 = 3.5 \pm 1.9 \%$  remains well above the calculated value.

The value of  $\alpha_{>}^2$  at  $T = 0$  has also been extracted using the calculated value of  $\delta_c = 0.65 \%$  in  $^{34}\text{Cl}$  which reproduces the corrected  $ft$  value.  $\alpha_{>}^2$  is extracted utilizing the formalism of Auerbach *et al.* [Aur09] with the assumption that  $\delta_c$  is same for  $^{34}\text{Cl}$  and  $^{32}\text{S}$ . According to this formalism  $\alpha_{>}^2$  is defined as

$$\alpha_{>}^2 = \frac{41\xi A^{2/3}}{4(I+1)V_1} \delta_c \quad (7)$$

where  $V_1 = 100 \text{ MeV}$ ,  $\xi = 3$ . Equation (7) yields  $\alpha_{>}^2 = 2.0 \%$  which in turn yields  $\Gamma_{\text{IVM}} = 1.2 \text{ MeV}$ .  $\alpha_{>}^2$  was extrapolated to higher temperatures using the same procedure described before. It is observed that the calculation, though underpredicts, better explains the measured data. It should be mentioned in this context that Melconian *et al.* [Mel11] have found  $\delta_c$  to be as high as  $5.3 \pm 0.9 \%$  which was attributed to the presence of close lying  $I = 0$  and  $I = 1$  states near 7.0 MeV excitation energy in  $^{32}\text{S}$  and it was corroborated by the shell model calculations. So, it would be interesting to perform the statistical model analysis with the local effects but is beyond the scope of the present thesis. It could be that, at low mass region, the isospin mixing has some finite value at zero temperature, then it gradually increases with temperature and then it

decreases in the statistical region (as is conceived qualitatively). It could also be possible that, as mentioned therein, the formalism of Sagawa *et al.* may be valid in medium and heavy mass regions. However, more data are required at still lower temperatures to understand the systematic behavior of isospin mixing in lower mass region.

In summary, the thesis contains the experimental study of two crucial properties of atomic nucleus utilizing the IVGDR. In the first part, the crucial ratio of shear viscosity to the entropy density has also been determined. Both  $\eta$  and  $s$  increase with temperature resulting in a mild decrease in  $\eta/s$  with temperature. At a given temperature,  $\eta/s$  is also found to be approximately independent of the nuclear size as well as the neutron-proton asymmetry. Moreover, the measured  $\eta/s$  remains confined in the range  $(2.5-6.5) \hbar/4\pi k_B$ . Thus it is observed experimentally that the nuclear fluid conform to the KSS conjecture and also establishes that strong fluidity is the universal characteristic of the strong interaction of many-body nuclear systems. This result, along the results of low-temperature quantum fluids and high-temperature QGP, suggests that large fluidity could possibly be the intrinsic characteristic feature of strongly coupled systems. In the second part, the isospin mixing has been measured at high temperature in  $^{32}\text{S}$  by utilizing the  $\gamma$ -decay of the isovector giant dipole resonance (IVGDR). The Coulomb spreading width  $\Gamma_{>}^{\downarrow}$  was found to be nearly independent of temperature and angular momentum. Moreover, isospin becomes a good quantum number with the increase in temperature. However,  $\alpha_{>}^2$ , when extrapolated to higher temperatures, by imposing its value at zero temperature, underpredicts the measured data.

# List of Figures

1.1	<i>Schematic representation of the variation of the number of accessible states as a function of excitation energy.</i> . . . . .	5
1.2	<i>Schematic representation of various collective modes inside the nucleus with <math>L = 0</math> (monopole), <math>L = 1</math> (dipole) and <math>L = 2</math> (quadrupole). <math>S</math> and <math>T</math> are spin and isospin quantum numbers, respectively (adopted from Ref. [Sup12b]).</i> . . . . .	7
1.3	<i>Schematic representation of the isovector giant dipole resonance.</i> . .	9
1.4	<i>(a) A typical high-energy <math>\gamma</math> ray spectrum from the decay of IVGDR built on an excited state of <math>^{31}\text{P}</math> populated at initial excitation energy of 46.2 MeV. The filled circles represent the experimental spectrum and the continuous line is the sum of statistical model calculation (short-dashed line) and a bremsstrahlung component (dot-dashed line). (b) Corresponding linearized plot.</i> . . . . .	11
2.1	<i>Schematic representation of the flow of a fluid between a moving plate and a stationary plate.</i> . . . . .	16
2.2	<i>Variation of <math>\eta/s</math> with temperature (adopted from Ref. [Kov05]).</i> . .	21
2.3	<i>Dependence of the ratio <math>\eta/s</math> on <math>g^2 N_c</math> (adopted from Ref. [Kov05]).</i> .	21
3.1	<i>Variation of the ground state isospin mixing parameter with mass number for even-even <math>N = Z</math> nuclei. The plot [square (green) with dashed line] is devoid of spurious mixing while the same [triangle (blue) with dashed line] is affected by spurious mixing (adopted from [Sat09]).</i> . . . . .	34
3.2	<i>Variation of isospin mixing parameter with temperature in <math>^{208}\text{Pb}</math> according to Eq. (3.12). The solid [green] and the dashed [blue] lines correspond to two different values of constant <math>c</math> that gives a mild temperature dependence of <math>\Gamma_{\text{IAS}}</math> and <math>\Gamma_{\text{M}}</math> (adopted from [Sag98]).</i> . .	35
3.3	<i>Schematic representation of isospin splitting of the GDR built on (a) <math> I, I = I_z\rangle</math> (b) <math> I + 1, I = I_z\rangle</math> states of the nucleus having isospin projection <math>I_z</math>.</i> . . . . .	41

4.1	Schematic diagram for the decay of compound nucleus. . . . .	47
5.1	Schematic diagram of the LAMBDA spectrometer arranged in three $7 \times 7$ matrix. . . . .	58
5.2	Energy spectrum of (a) $^{22}\text{Na}$ (b) $^{241}\text{Am-}^9\text{Be}$ (c) minimum ionizing cosmic muon backgrounds. The green and blue solid lines in Fig. (b) are $^{241}\text{Am-}^9\text{Be}$ spectra with leak and no leak conditions, respectively. The red line in Fig. (c) represents the landau fit to the experimental cosmic muon spectrum (green solid line). . . . .	60
5.3	A typical energy calibration curve of a detector element of the LAMBDA spectrometer. The green solid circles are the experimental points and the red solid line is the best fitted straight line. . . . .	61
5.4	Geometry of the LAMBDA array used in the experiments. The grey cover is the passive lead shield. The left panel is the cross sectional view and the right panel shows the three dimensional view. . . . .	62
5.5	Simulated response function of the LAMBDA spectrometer for different incident $\gamma$ -ray energies. . . . .	63
5.6	50 element multiplicity filter divided in two blocks with 25 elements each and arranged in $5 \times 5$ matrix. . . . .	64
5.7	Geometry of the multiplicity filter used in the experiments. The left panel is the cross sectional view and the right panel shows the three dimensional view. . . . .	65
5.8	(a) Experimental (green symbols) and simulated (red line) fold distributions for $^{31}\text{P}$ populated at initial excitation energy of 46.2 MeV. The simulated parameters are $M_0 = 5$ , $\delta m = 1$ , $C = 1$ . Peak energy and width of the energy distribution are 0.65 MeV and 1.2 MeV, respectively. (b) Incident and different fold gated angular momentum distributions. . . . .	66
5.9	Liquid organic scintillator (BC501A) based neutron TOF array. . . . .	67
5.10	Experimental (symbols) and simulated (solid line) neutron detection efficiency of BC501A based neutron TOF detector (adopted from [Bal15]). . . . .	68
5.11	Experimental set-up used in this thesis. (a) LAMBDA spectrometer, (b) Multiplicity filter, (c) Neutron TOF detector and (d) Clover detector. . . . .	70
5.12	Circuit diagram used for detection of high-energy $\gamma$ rays. . . . .	71
5.13	Circuit diagram used for neutron measurements. . . . .	73

5.14	(a) A typical time of flight spectrum of a detector element of the LAMBDA array. (b) A typical cyclotron RF time spectrum. Both spectra were measured with respect to the multiplicity filter. . . . .	75
5.15	A typical short vs long 2d-dimensional spectrum of a detector element of the LAMBDA array. Only those events are considered to be valid events that lie in between the two straight lines. . . . .	76
5.16	Typical cosmic muon hit patterns in the LAMBDA spectrometer. . .	77
5.17	Typical hit patterns of true $\gamma$ events in the LAMBDA spectrometer.	78
5.18	Typical high-energy $\gamma$ ray spectra for different gate conditions. (a) Raw but time validated, (b) prompt time gated, (c) prompt time and PSD gated, (d) prompt time, PSD and prompt RF time gated, (e) same as d with RF and time background subtracted, (f) time background spectrum, (g) RF time background spectrum. . . . .	79
5.19	A typical two dimensional plot of ZCT vs TOF. The events that remain within the two dimensional cut are neutron events which are used for further analysis. . . . .	80
5.20	Typical evaporated neutron energy spectra of $^{31}\text{P}$ with only neutron gate in TOF spectrum (green solid circles) and with the two dimensional cut (i.e. both TOF and ZCT gate) as shown in Fig. (5.19) (blue open circles). . . . .	81
6.1	(a) Experimental (green symbols) and simulated (red line) fold distributions for $^{31}\text{P}$ populated at initial excitation energy of 46.2 MeV. The simulated parameters are $M_0 = 5$ , $\delta m = 1$ , $C = 1$ . Peak energy and width of the energy distribution are 0.65 MeV and 1.2 MeV, respectively (section 5.3.1). (b) Incident and different fold gated angular momentum distributions. . . . .	85
6.2	Variation of $a_1(E_\gamma)$ with the $\gamma$ ray energy. The green solid circles are experimentally determined, while the red solid line is theoretically calculated for $E_0 = 5.3$ MeV and $v_{nn} = 0.6 v_{beam}$ . . . . .	87
6.3	Different fold-gated high-energy $\gamma$ ray spectra (left panel) and the evaporated neutron energy spectra (right panel) for $^{31}\text{P}$ . The green solid symbols are experimentally measured spectra, while the red solid lines are the respective statistical model calculations. . . . .	88
6.4	Different fold-gated linearized $\gamma$ ray spectra for $^{31}\text{P}$ . The green solid symbols are experimentally measured spectra, while the red solid lines are the respective Lorentzian having the GDR parameters as shown in table 6.1. . . . .	90
6.5	Comparison of the measured GDR widths (symbols) with the CTFM model calculations. . . . .	92

6.6	Variation of (a) the ground state GDR width and (b) average GDR energy with the mass number. The symbols are (a) the accepted ground state GDR width and (b) the average of the measured GDR energies. The blue dot-dashed, green solid and pink dashed lines are the calculated ground state GDR widths and energies for $\eta(0) = 0.55u$ , $1.0u$ , and $1.25u$ , respectively. . . . .	93
6.7	Experimental data (symbols) along with the theoretical predictions (solid lines) for $\eta$ (upper panel), $s$ (middle panel), and $\eta/s$ (lower panel). Blue short-dashed line (lower panel) is the KSS bound. . . .	95
6.8	Variation of $\eta$ (upper panel (a) & (d)), $s$ (middle panel (b) & (e)), and $\eta/s$ (lower panel (c) & (f)) with mass number at the specified temperature range. . . . .	97
7.1	(a) Experimental fold distributions along with the simulated one. (b) The total fusion cross-section (arb. unit) (green solid triangles with red dot-dashed line) and the selected angular momentum distribution (solid blue line) for statistical model calculations. . . . .	102
7.2	Experimental neutron spectra (green filled circles) along with the CASCADE predictions corresponding to best values of $\tilde{a}$ (red solid lines) for (a) $^{31}\text{P}$ and (b) $^{32}\text{S}$ . . . . .	104
7.3	(a) Experimental high-energy $\gamma$ ray spectra (green filled circles) along with CASCADE calculations for $\Gamma_{>}^{\downarrow} = 0$ keV (blue dashed line) and $\Gamma_{>}^{\downarrow} = 24$ keV (red solid line) for $^{31}\text{P}$ (a) and $^{32}\text{S}$ (c). The corresponding linearized plots are also shown for $^{31}\text{P}$ (b) and $^{32}\text{S}$ (d). . . . .	105
7.4	(a) Experimental $\sigma_{\gamma} \times \epsilon_{in}$ for $^{31}\text{P}$ (green open circles) and $^{32}\text{S}$ (blue filled circles). (b) Experimental ratio (pink filled circles) of the $\gamma$ ray cross section of $^{32}\text{S}$ and $^{31}\text{P}$ along with the CASCADE predictions for different $\Gamma_{>}^{\downarrow}$ . $\Gamma_{>}^{\downarrow} = 0$ keV for blue long-dashed line (zero mixing), $\Gamma_{>}^{\downarrow} = 24$ keV for red solid line and $\Gamma_{>}^{\downarrow} = 10$ MeV for black short-dashed line (full mixing). $\chi^2$ as a function of $\Gamma_{>}^{\downarrow}$ (inset Fig. b). . . . .	106
7.5	Variation of isospin mixing parameters with angular momentum. The green circles represent $\alpha_{>}^2$ , while the blue triangles stand for $\alpha_{<}^2$ . . .	108
7.6	Variation of the Coulomb spreading width with mass number. The red square is the present measurement and the green circle is the measured datum of Ref. [Hab04] for $^{32}\text{S}$ . The pink circles are the measured data for $^{80}\text{Zr}$ [Cor11, Cer15]. (adopted from Ref. [Cer16]).	109
7.7	The isospin mixing parameter $\alpha_{<}^2$ as a function of (a) excitation energy (b) temperature. In Fig. (b) the red square is the present measurement, while the dark blue diamond represents the measured datum of Ref. [Hab04] for $^{32}\text{S}$ . . . . .	110
7.8	Comparison of $\alpha_{>}^2$ with calculation at high temperature [Sag98]. . .	112

# List of Tables

6.1	<i>Experimental GDR and asymptotic NLD parameters at the specified angular momentum and temperature . . . . .</i>	89
7.1	<i>Experimentally determined values of isospin mixing parameter . . .</i>	107



# Chapter 1

## Introduction

A natural approach to study the properties of a system is to perturb it externally and observe its response. One has to opt for an appropriate tool or perturbation to investigate a specific system property. Over the years, various tools have been unearthed to explore the intriguing and exciting facets of the atomic nucleus, which by virtue of its intrinsic complexity, mystery and practical applications, still remains an exciting entity for physicists.

The isovector giant dipole resonance (IVGDR), a member of a broader family of collective resonances called giant resonances, is an excellent probe to study nuclear properties at extreme conditions. It is a collective motion of proton and neutron fluids observed in all nuclei. The GDR can be built on the ground state as well as every excited state of nuclei. Historically, the GDR built on the ground state of a nucleus has been studied by the photoabsorption reaction, while that built on the excited state has been probed by fusion evaporation and inelastic scattering reactions. The lifetime of the GDR is very small ( $10^{-21}$ - $10^{-22}$  sec) and it decays by the emission of high-energy  $\gamma$  rays in 10-25 MeV regions depending on the mass of the nucleus. The small lifetime of the resonance makes it an excellent probe to study exotic nuclear shapes, fission time scale

etc. Due to the presence of nuclear dissipation, the fission process is slowed down resulting in an increased emission of pre-fission particles and  $\gamma$  rays. The viscosity and hence the fission time scale is determined by using a dynamical fission model [Pau94, Kra40]. In this context, it is interesting to note that the dissipation parameter, which fit the pre-fission GDR  $\gamma$  ray multiplicities, also agrees quite well with the pre-fission neutron multiplicities [Pau94].

The present thesis deals with the experimental study of two crucial properties of atomic nuclei at finite temperatures. The first part contains a self-consistent experimental determination of the ratio of shear viscosity ( $\eta$ ) to entropy density ( $s$ ) for equilibrated finite nuclear matter from  $A\sim 30$  to  $A\sim 208$  at different temperatures, while the second part presents an exclusive experimental study of isospin mixing at high temperature in  $^{32}\text{S}$ .

It is observed experimentally that the width of the GDR built on the ground state of nucleus increases with the decrease in mass number. This suggests that the damping mechanism of the GDR is indeed similar to that of a viscous fluid where the modulus of decay ( $\tau$ ) (resonance width is inversely proportional to  $\tau$ ) of the oscillation decreases with the decrease in system volume. Recent theoretical calculations have shown that the shear viscosity at finite temperature is related to the width and energy of the GDR. Thus by measuring the GDR widths and energies,  $\eta$  has been determined at different temperatures for various nuclear masses. Simultaneously, the entropy density  $s$  has been extracted by precisely measuring the nuclear level density (NLD) parameter and nuclear temperature. Simultaneous determination of  $\eta$  and  $s$  enabled us to deduce  $\eta/s$  in a self-consistent way at different temperatures and various mass regions.

In long wavelength limit, ( $qR \ll 1$ ,  $q$  being the momentum transfer and  $R$  is

nuclear dimension) the  $\gamma$  transitions from the decay of the IVGDR are forbidden between the states of the same isospin ( $I$ ). Consequently, if a self-conjugate compound nucleus ( $N=Z$ ) is populated through a self-conjugate entrance channel (both the target and the projectile are self-conjugate), only  $I=0$  states are populated in the compound nucleus (CN) with the assumption that isospin is fully conserved. Due to the above mentioned isospin selection rule,  $\gamma$  transitions only between states  $I=0$  to  $I=1$  are allowed. However, at moderate excitation energies there are not many  $I=1$  final states to be populated by IVGDR  $\gamma$  decay. This results in the suppression of the yield of  $\gamma$  rays decaying from self-conjugate nuclei populated through  $I=0$  entrance channel as compared to  $I\neq 0$  nuclei for which all  $\gamma$  transitions are allowed. However, in presence of an admixture of  $I=1$  states in the initial compound nucleus, the IVGDR  $\gamma$  yield is enhanced as these  $I=1$  states can decay to  $I=0$  states and the degree of enhancement depends on the degree of isospin mixing.

As both subjects of this thesis include temperature and utilize GDR as a probe, we start by giving a brief introduction of the concept of nuclear temperature. Later, in this chapter, a brief introduction on the Giant resonances and the Isovector Giant dipole resonance is presented. The theoretical formalisms and models for describing  $\eta/s$  and isospin mixing have been described in chapter 2 and chapter 3, respectively. The details of the statistical model calculations have been presented in chapter 4. The details of the detector systems, simulation studies and data reduction techniques have been depicted in chapter 5. The experimental details and results of  $\eta/s$  and isospin mixing have been discussed in chapter 6 and chapter 7, respectively. Finally the summary and future outlook have been presented in chapter 8.

## 1.1 The concept of nuclear temperature

It is a well-known fact that nature favors a system to remain in its lowest possible energy state known as the ground state. In a simplistic model, protons and neutrons occupy the lowest single particle states in accordance with the Pauli exclusion principle in the ground state of nucleus. The highest occupied single particle state is called the Fermi level. When energy ( $E^*$ ) is pumped into the nucleus (say, by bombarding a target nucleus with a projectile forming a compound nucleus; the relative kinetic energy of the projectile and the target provides the excitation to the compound nucleus.) the protons and neutrons near the Fermi surface are excited into the higher available single particle states resulting in nuclear excitation, the number of particles excited being dependent on the supplied energy  $E^*$ . At small  $E^*$ , only a few particles are excited and the separation of the excited states ( $D$ ) is large [Fig. (1.1)]. As  $E^*$  gradually increases, the number of excited particles increases. This enhances the number of possible ways in which energy  $E^*$  can be distributed resulting in large number and small separation of the excited states. However, with the increase in  $E^*$ , the individual excited state attains intrinsic width owing to particle decay ( $\Gamma^\dagger$ ). At very high  $E^*$ , intrinsic width of the individual states becomes very large as compared to the separation (i.e.  $\Gamma^\dagger \gg D$ ). In this case one cannot consider the individual states, rather, one defines the density of states  $\rho(E^*, A)$  which gives the number of accessible states in the energy interval  $E^*$  and  $E^*+dE^*$ ,  $A$  being the mass number of the nucleus. In accordance with the statistical physics, one defines the temperature as

$$\frac{1}{T_s} \equiv \left[ \frac{\partial S(E)}{\partial E} \right]_{E=E^*} = \left[ \frac{\partial}{\partial E} \ln \rho(E) \right]_{E=E^*}, \quad (1.1)$$

where  $S$  is the entropy of the system.  $T_s$  is also called microcanonical temperature. The state density  $\rho(E^*, A)$  could be calculated by taking the inverse

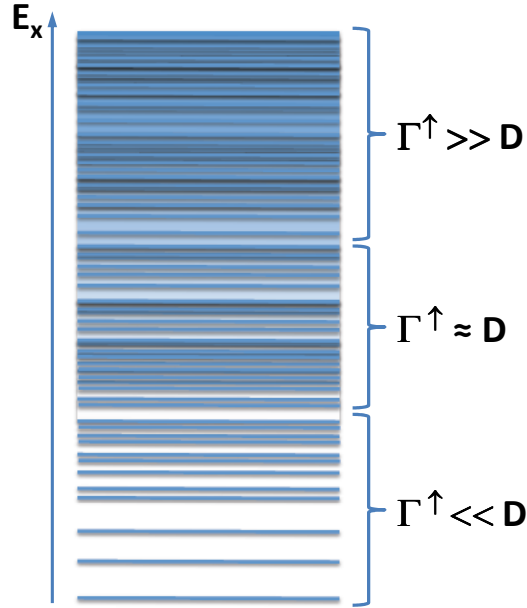


Figure 1.1: *Schematic representation of the variation of the number of accessible states as a function of excitation energy.*

Laplace transform of the grand canonical partition function ( $Z$ ) [Boh99a]. The temperature at which the grand canonical partition function becomes maximum, is called the nuclear temperature ( $T_{\text{nuc}}$ ) [Boh99a]. It is observed that  $T_{\text{nuc}} \equiv T = \sqrt{(E^*/a)}$ . Here  $a$  is called nuclear level density (NLD) parameter which is a measure of the density of single particle states at the Fermi energy. It is observed that [Mor94]

$$\frac{1}{T_s} = \frac{1}{T} - \frac{\gamma'}{E^*}, \quad (1.2)$$

where the constant  $\gamma'$  ranges from one to two. For large  $E^*$  and particle number, the term with constant  $\gamma'$  vanishes, thus  $T_s$  and  $T$  become equivalent. Physically, the nuclear temperature  $T$  roughly provides the average energy per excited nucleon. In this thesis, temperature refers to the nuclear temperature, unless mentioned otherwise.

## 1.2 Giant resonances and their classifications

The giant resonances (GR), generic features of quantum many-body nuclear system, are high-frequency, small-amplitude and highly-damped collective vibrations in which nearly all nucleons take part [Bor98, Har01]. These resonances lie in 10 to 25 MeV excitations depending on the mass and type of the giant resonance. The amplitude of oscillation is a few percent of the nuclear radius and the resonance gets damped after a few vibrations. The resonance is called giant because nearly all nucleons participate in the process and it exhausts a large fraction of the energy-weighted sum rule defined by  $S_L = \sum_f (E_f - E_i) M_{if}^2$ .  $M_{if}$  is the transition matrix element between the initial and final states having energies  $E_i$  and  $E_f$ , respectively and the summation runs over all final states. The giant resonances are characterized by three parameters, namely, the energy, the width and the strength. Since all nuclei participate in these resonances, the characteristic properties do not depend on detailed microscopic structure; rather they vary smoothly with the nuclear mass.

Depending on the interaction involved in the GR excitation, there are electric and magnetic giant resonances. The electric GRs are excited by the interaction of electromagnetic field (EM) with the electric charge current in the nucleus, while the magnetic GRs are caused by the interaction of EM field with the magnetization current and also involve the spin excitation ( $\Delta S=1$ ). To the first order approximation and in the long wave length limit ( $qR \ll 1$ ) the operator that excites the electric giant resonances can be represented as [Har01, Wil69]

$$\hat{\mathbf{O}}_E(\mathbf{L}, \mathbf{M}) = \frac{1}{2} \hat{\mathbf{e}} \sum_{k=1}^A r_k^L Y_{LM}(\Omega_k) - \frac{1}{2} \hat{\mathbf{e}} \sum_{k=1}^A \hat{\mathbf{i}}_{3k} r_k^L Y_{LM}(\Omega_k), \quad (1.3)$$

where  $\hat{\mathbf{i}}_3 = 2\hat{\mathbf{i}}_z$  is the isospin analog of the third component of the Pauli spin matrix [Wil69] and its eigenvalues are +1 and -1 for neutron and proton, re-

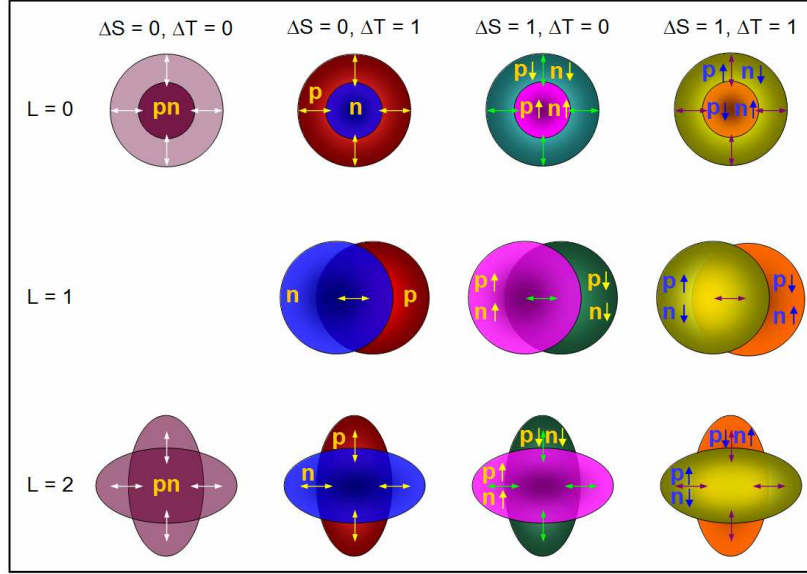


Figure 1.2: Schematic representation of various collective modes inside the nucleus with  $L = 0$  (monopole),  $L = 1$  (dipole) and  $L = 2$  (quadrupole).  $S$  and  $T$  are spin and isospin quantum numbers, respectively (adopted from Ref. [Sup12b]).

spectively. The first and second parts of Eq. (1.3) correspond to the isoscalar (IS) and the isovector (IV) part of the operator, respectively. The isovector excitations involve the change in the isospin quantum number ( $I$ ) by one unit ( $\Delta I = 1$ ), while the isoscalar excitations do not involve any change in  $I$ . From the macroscopic point of view, the isoscalar and the isovector resonances correspond to the in-phase and the out of phase oscillations of proton and neutron fluids in the nucleus. Both the isoscalar and the isovector resonances can have different multipolar excitations e.g.  $L = 0$  means giant monopole resonance,  $L = 1$  corresponds to giant dipole resonance etc. However, it should be mentioned that in the first order approximation, there is no monopole excitation as the operator in Eq. (1.3) is a constant for  $L = 0$ . Therefore, the monopole resonance is purely a second order effect. Similarly, the ISGDR is also a higher order effect because the first part of Eq. (1.3) gives the linear translation of the centre of mass (c.m.) and involve no intrinsic excitation. The energy of different

giant resonances is proportional to  $A^{-1/3}$  and the constant of proportionality is approximately equal to 79 MeV for IVGDR, 80 MeV for ISGMR, 65 MeV for ISGQR and 130 MeV for IVGQR. The magnetic giant resonances can also have different multipolarities and isospin modes. Different giant resonance modes have been schematically described in Fig. (1.2). This thesis deals with only IVGDR and it is also referred to, unless otherwise mentioned, as the GDR.

### 1.3 The isovector giant dipole resonance (IVGDR)

The isovector giant dipole resonance (IVGDR) is the oldest and best-known GR owing to its high selectivity of excitation by  $\gamma$  ray absorption. In simple hydrodynamic model, it can be thought of as the collective vibration of protons against neutrons [Fig. (1.3)], where the restoring force comes from the nuclear symmetry energy and effective surface stiffness [Boh99]. Microscopically, it is described as the coherent superposition of  $1p$ - $1h$  dipole excitations across one major shell ( $1\hbar\omega'$ ). The residual interactions between particles and holes shift the energy of the superimposed state at  $2\hbar\omega'$  and the state exhausts all dipole strength [Bro59, Bro67]. Although, recently a counterexample has been published [Qua17], Brink-Axel hypothesis states that the GDR can be built on every excited state with similar properties to that built on the ground state of the nucleus [Bri55, Axe62].

#### 1.3.1 IVGDR built on ground state of nucleus

The first evidence of the IVGDR was observed in the photoabsorption experiment of Bothe and Getner [Bot37] in 1937. They observed large  $(\gamma, n)$  cross section by bombarding 17 MeV  $\gamma$  ray on  $^{63}\text{Cu}$  target. Few years later, in 1947 Baldwin and Klaiber, while performing photofission reactions in different tar-

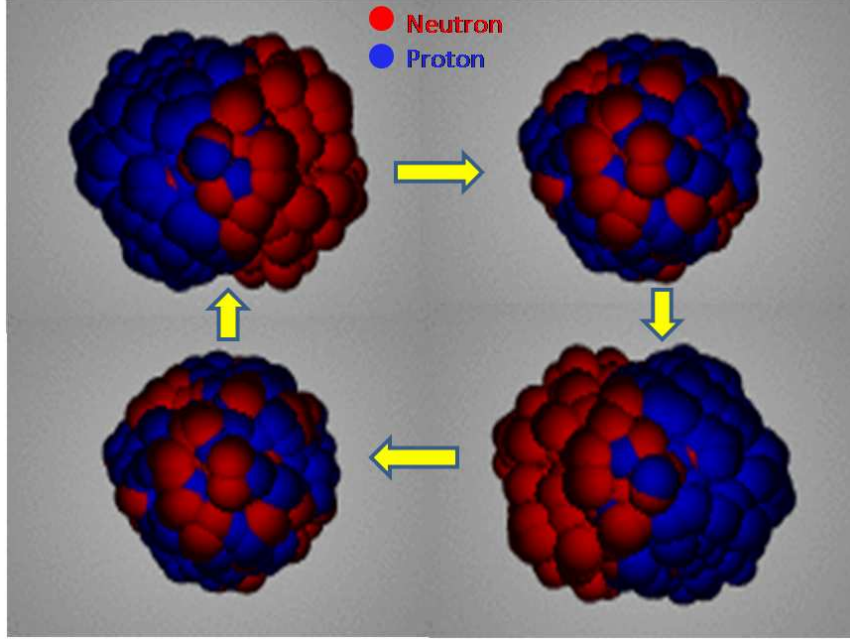


Figure 1.3: *Schematic representation of the isovector giant dipole resonance.*

gets, observed that the excitation function of  $U$  and  $Th$  having a resonance structure with maximum at  $\sim 15$  MeV and a width of  $\sim 5$  MeV [Bal47]. Many more photoabsorption reactions followed and it was observed that the GDR line shape was typically a Lorentzian characterized by the energy ( $E_{\text{GDR}}$ ), the width ( $\Gamma_{\text{GDR}}$ ) and the strength ( $S_{\text{GDR}}$ )

$$\sigma_{\text{abs}}(E_\gamma) = \frac{\sigma_m \Gamma_{\text{GDR}}^2 E_\gamma^2}{(E_\gamma^2 - E_{\text{GDR}}^2)^2 + \Gamma_{\text{GDR}}^2 E_\gamma^2}. \quad (1.4)$$

The energy-integrated strength of the GDR is given by

$$\int_0^\infty \sigma_{\text{abs}}(E_\gamma) dE_\gamma = 60 \frac{NZ}{A}. \quad (1.5)$$

Experimentally it is observed that the integrated strength remains within 20% for medium and heavy nuclei and for light nuclei, the strength falls little short of it. This indicates that all nuclei take part in forming the GDR.

According to the macroscopic model of Goldhaber and Teller (GT) [Gol48], the GDR is the out of phase oscillation of rigid but interpenetrating neutron and

proton spheres against each other keeping the centre of mass fixed. The GDR energy, in this model, is proportional to  $\sqrt{(k'/M)}$  where  $k'$  is the restoring force and  $M$  is nuclear mass. The restoring force is proportional to nuclear surface area i.e.  $R^2 \sim A^{2/3}$ . This implies  $E_{\text{GDR}} \propto \sqrt{A^{2/3}/A} = A^{-1/6}$ . On the other hand, the model put forward by Steinwedel and Jensen (SJ) [Ste50], describes GDR as the out of phase density oscillation of neutron fluid versus the proton fluid within a sharp and fixed boundary keeping the total density fixed. In this model,  $E_{\text{GDR}}$  is proportional to  $R^{-1} = A^{-1/3}$ . In practice, experimental GDR energies of medium and heavy nuclei are well reproduced by the following weighted sum of the above two prescriptions [Ber75]

$$E_{\text{GDR}} = 31.2A^{-1/3} + 20.6A^{-1/6}. \quad (1.6)$$

The GDR is a highly damped motion characterized by a very small lifetime ( $10^{-21}$ - $10^{-22}$  sec) or large width. Owing to the short lifetime, it competes with other modes of nuclear decay and can probe the evolution of different degrees of freedom e.g. shape, isospin etc. A vivid picture of the origin of large width for the GDR could be depicted microscopically. In this picture, the GDR width comprises of three parts, namely, the Landau width ( $\Gamma_{\text{LD}}$ ), the spreading width ( $\Gamma_{\text{sp}}^{\downarrow}$ ) and the escape width ( $\Gamma_{\text{es}}^{\uparrow}$ ).  $\Gamma_{\text{LD}}$  originates from the coupling of the collective  $1p$ - $1h$  state (the GDR state) to the non-collective  $1p$ - $1h$  configurations. The spreading width  $\Gamma_{\text{sp}}^{\downarrow}$  arises due to the coupling of the GDR state to  $2p$ - $2h$ ,  $3p$ - $3h$  and more complicated configurations, whereas, the escape width  $\Gamma_{\text{es}}^{\uparrow}$  is caused by the coupling to the continuum causing direct particle decay into the hole states of the residual nucleus. In medium and heavy nuclei,  $\Gamma_{\text{sp}}^{\downarrow}$  has the major contribution while  $\Gamma_{\text{LD}}$  and  $\Gamma_{\text{es}}^{\uparrow}$  give a minute fraction of the GDR width. However, for light nuclei  $\Gamma_{\text{es}}^{\uparrow}$  ( $\sim 13 \exp[-4.69\sqrt{A/U}]$  MeV,  $A$  and  $U$  being the mass number and intrinsic excitation energy of the compound nuclear state,

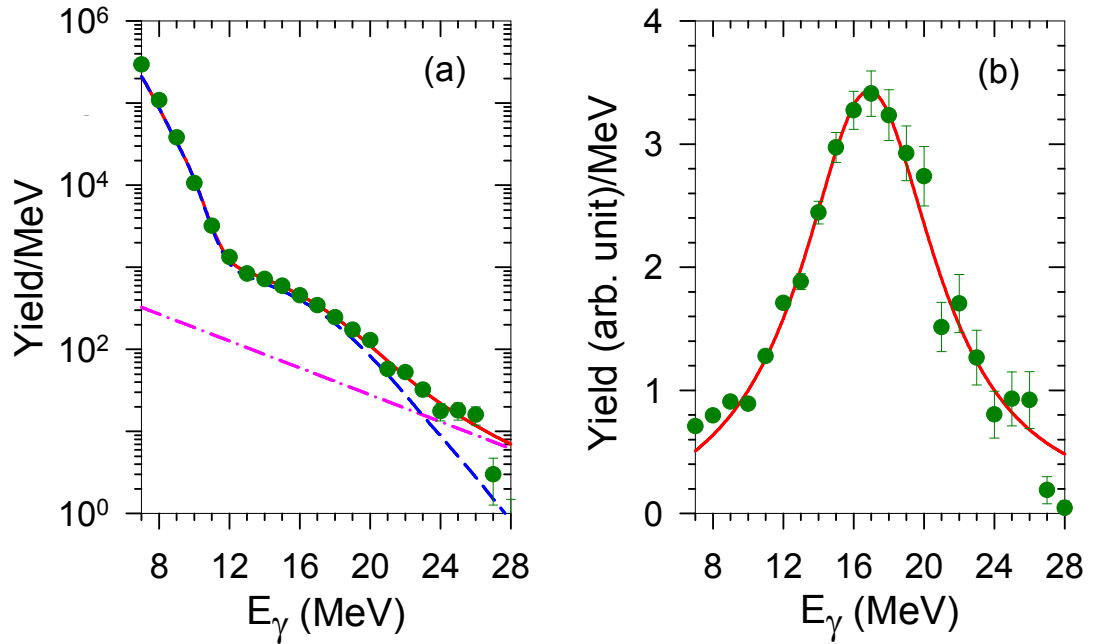


Figure 1.4: (a) A typical high-energy  $\gamma$  ray spectrum from the decay of IVGDR built on an excited state of  $^{31}\text{P}$  populated at initial excitation energy of 46.2 MeV. The filled circles represent the experimental spectrum and the continuous line is the sum of statistical model calculation (short-dashed line) and a bremsstrahlung component (dot-dashed line). (b) Corresponding linearized plot.

respectively [Beh91]) contributes appreciably to the total width.

### 1.3.2 IVGDR built on excited state of nucleus

As put forward by Brink and Axel [Bri55, Axe62], the GDR can be built on every excited state of nucleus with similar properties to that built on the ground state. The rationale behind this lies in the fact that typical lifetime of excited states of nucleus is  $\sim 1000$  times larger than that of the GDR. Therefore, once a nuclear excited state is formed, there is a finite probability that it evolves to a configuration which can be thought of as the GDR built on some excited state of the nucleus.

The first observation of the excited state GDR was made from the measure-

ment of  $\gamma$  ray spectrum in spontaneous fission of  $^{252}\text{Cf}$ , where certain enhancement was observed at  $E_\gamma \sim 10\text{-}15$  MeV which corresponds to IVGDR [Die74]. Later, in 1981, Newton *et al.* first studied the GDR utilizing heavy ion fusion reactions [New81]. During the last three and a half decades, exhaustive studies have been accomplished in excited state GDR by using two complementary techniques, namely inelastic scattering and fusion evaporation reactions. In inelastic scattering reaction [Ram96, Bau98, Hec03] the compound nucleus is populated with low angular momentum. This method thus, though with a large uncertainty in determination of initial excitation energy or temperature ( $T$ ), could exclusively probe the  $T$  dependence of GDR parameters. On the other hand, in fusion evaporation reaction, the compound nucleus is populated at definite initial excitation energy but with a broad range of angular momentum. Therefore, it is difficult to disentangle the effects of temperature and angular momentum. In this thesis, we have utilized the fusion evaporation reaction to populate the compound nucleus. However, we have used light-ion ( $\alpha$ ) beam enabling us to populate the compound nucleus with very low angular momentum which does not affect the GDR parameters.

The excited state GDR relaxes by the emission of high-energy  $\gamma$  rays. It competes with other modes of nuclear decay (neutron, proton,  $\alpha$ , fission etc.) and appears as a bump in the characteristic exponentially decaying  $\gamma$  ray spectrum. Fig. (1.4) shows a typical high-energy  $\gamma$  ray spectrum from the decay of GDR built on excited states of atomic nuclei. The  $\gamma$  rays below 12 MeV, come from the statistical decay of compound nuclei whose intrinsic excitation energy lies below the particle-threshold energy ( $\sim 8$  MeV). The apparent steepness in the slope suggests that indeed these  $\gamma$  rays are emitted from the lower stages of compound nuclear decay chain. The bump in 12-23 MeV regions comes from the statistical decay of the GDR mostly in the initial stages of the decay chain. The

spectra above 24 MeV arise mainly from nucleon-nucleon bremsstrahlung mechanism at the initial stage of equilibrium process in compound-nuclear reaction. The GDR parameters are extracted by comparing the experimental spectrum with the statistical model calculations (chapter 4). The bremsstrahlung component is parameterized by an exponentially decaying function whose slope can be determined by angular distribution measurements of high-energy  $\gamma$  rays.

The systematics, gathered experimentally during the last three and half decades, show that the GDR energy and strength do not change with excitation energy or temperature; but the width increases with the increase in temperature. In recent years, considerable interests have been shown to study the GDR at very low temperatures ( $< 1.5$  MeV) [Sup12a, Dee12, Bal14] and at highest available temperatures ( $> 3.0$  MeV) [Bra89, Kel99, Wie06, Cie15]. At lower temperatures, the measured GDR width is found to be highly suppressed as compared to theoretical predictions. On the other hand, there is heated debate on the saturation of GDR width at higher temperatures.

Different theoretical models have been proposed to explain the increase in apparent GDR width with temperature. The most successful model has been the adiabatic thermal shape fluctuation model (TSFM) [Gal87, Alh88, Orm96]. It says that, owing to the finite size, the shape of the compound nucleus fluctuates around an equilibrium shape at a given temperature. As the GDR vibrations are much faster than the thermal shape fluctuation, the resulting GDR line shape is the superposition of different line shapes corresponding to various shapes of the CN. As the temperature increases, the fluctuation increases resulting in the increase in apparent GDR width. This model explains the experimental data in the range of temperature between  $1.5 \text{ MeV} < T < 3.0 \text{ MeV}$  and low angular momentum ( $J < 50\hbar$ ). Later Kusnezov proposed a parameterization

based on TSFM to describe the  $T$  and  $J$  variation of GDR width [Kus98]. This is called phenomenological thermal shape fluctuation model (pTSFM) and it explains the experimental data in  $T > 1.5$  MeV. However, both the models fail to explain the data at  $T < 1.5$  MeV. To describe the data in the unexplained  $T < 1.5$  MeV, a new parameterized model, called critical temperature included fluctuation model (CTFM), has been proposed [Dee12]. According to CTFM, the GDR width should remain constant up to a temperature, called critical temperature ( $T_c$ ), and increase thereafter. The origin of  $T_c$  lies in the fact that the GDR itself induces a fluctuation in shape due to which it cannot feel the effect of thermal fluctuations. The temperature at which the intrinsic fluctuation equals to the thermal fluctuation is called the critical temperature.  $T_c$  is found to increase linearly with the decrease in mass number by the relation  $T_c = 0.7 + 37.5/A$ . This model well explains the recently measured low temperature as well as the high temperature data [Dee12, Bal14, Gho16, Cer17].

Apart from the above mentioned macroscopic models, a microscopic model has also been proposed to describe the  $T$  and  $J$  dependence of GDR width [Dan98a, Dan98b, Dan12]. According to this model, due to the temperature-induced distortion in the Fermi surface, new particle-particle ( $pp$ ) and hole-hole ( $hh$ ) configurations are created at finite temperatures. Therefore, the GDR state, apart from coupling to the  $ph$  configurations, also couples by collisions to these incoherent  $pp$  and  $hh$  configurations resulting in thermal width ( $\Gamma_T$ ). Within this model, it is observed that the GDR width gradually increases with temperature; however, at high temperatures the width tends to saturate. It is interesting to note that, according to the proponents of this model, the  $pp$  and  $hh$  coupling is a microscopic description of thermal shape fluctuation. This model well explains the experimental data at low temperatures as well as high temperatures.

# Chapter 2

## Viscosity and Entropy Density

### 2.1 Viscosity of a fluid

A fluid is any substance that deforms continuously when subjected to a stress, no matter how small. A typical characteristic property of a fluid is viscosity, which is a measure of its resistance to gradual deformation by shear or tensile stress. The main sources of viscosity are the intermolecular cohesion and intermolecular or interparticle momentum transfer. A fluid can be attributed with mainly three kinds of viscosities, namely

- (a) **Bulk viscosity ( $\zeta$ ):** This type of viscosity is important when a fluid is expanded or compressed. The rate of expansion or compression is governed by the bulk viscosity which exerts an internal frictional force when the fluid is expanded or compressed.
  
- (b) **Shear viscosity ( $\eta$ ):** It is the resistance of a fluid to the shear flow between two adjacent layers. Let us consider a fluid as shown in Fig. (2.1). A uniform tangential force is applied in the  $x$ -direction on the upper plate of area  $A$ . Due to this force, the fluid layer just adjacent to the upper

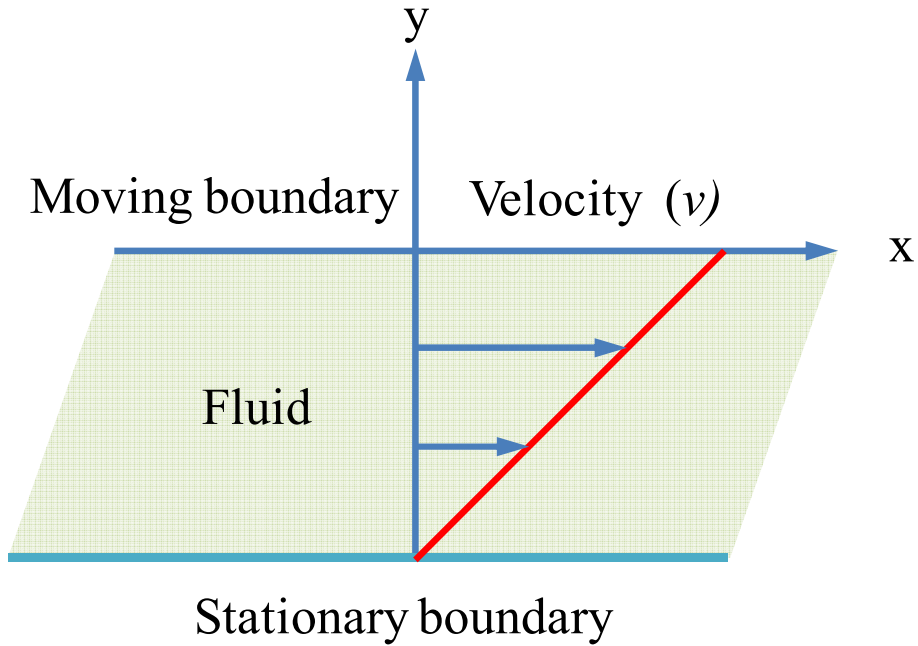


Figure 2.1: Schematic representation of the flow of a fluid between a moving plate and a stationary plate.

plate starts moving with the velocity of the plate ( $v$ ). However, the layer just adjacent to the lower plate remains fixed. Therefore, there exists a velocity gradient in the  $y$ -direction resulting in a shear stress between two adjacent layers of the fluid. The shear stress  $\tau$  is given by

$$\tau = \eta \frac{dv}{dy}, \quad (2.1)$$

where  $\eta$  is called shear viscosity. Physically, it gives the efficiency of momentum transfer between the adjacent layers of the fluid.

- (c) **kinematic viscosity ( $\nu$ ):** It is the ratio of shear viscosity to mass density of a fluid ( $\nu = \eta/\rho_m$ ).

This thesis mainly deals with the shear viscosity of finite nuclear matter at finite temperature. The inverse of shear viscosity is sometimes called the fluidity. However, in section 2.3, it will be discussed qualitatively that fluidity

is not only governed by the transport parameter  $\eta$ , but by the ratio of shear viscosity to the thermodynamic parameter entropy volume density ( $s$ ).

## 2.2 Entropy and entropy density

Entropy ( $S$ ) is an extensive thermodynamic quantity which reflects the disorder of a system. Larger is the value of entropy, larger is its disorder, larger is the stability of the system. Entropy density ( $s$ ), on the other hand, is an intensive quantity defined as the entropy per unit volume of a system. For an atomic nucleus the entropy density is given by

$$s \equiv \frac{S}{V} = \frac{\rho}{A} S, \quad (2.2)$$

where  $A$  and  $V$  are the mass number and the volume of the nucleus and  $\rho$  is the nuclear density. For a system of fermions having single particle states (energy states of individual fermions) of energy  $e_i$ , the entropy is given by

$$S = -k_B \sum_i [f_i \ln f_i + (1 - f_i) \ln(1 - f_i)], \quad (2.3)$$

where  $k_B$  is the Boltzmann constant and  $f_i$  is the occupation probability of the state of energy  $e_i$  given by

$$f_i = \frac{1}{1 + \exp\{(e_i - \mu)/T\}}. \quad (2.4)$$

Here  $\mu$  is the chemical potential and  $T$  is the temperature in units of MeV. At finite temperature  $\mu$  is calculated by using the particle conservation relation viz.  $n = \sum_i f_i$  (In the present case,  $n = N$  or  $Z$ ,  $N$  and  $Z$  being the number of neutron and proton, respectively).

In low temperature region such that  $T < \epsilon_F$  ( $\epsilon_F$  being the Fermi energy), entropy is given by

$$S = 2aT, \quad (2.5)$$

where  $a$  is the nuclear level density (NLD) parameter. Note that  $a$  is a function of temperature and is calculated using the Ignatyuk prescription [Ign75]

$$a = \tilde{a} \left[ 1 + \frac{\Delta S}{U} \{1 - \exp(-\gamma U)\} \right], \quad (2.6)$$

where  $\tilde{a}$  is the asymptotic NLD parameter given by  $\tilde{a} = (\pi^2/6)g(\epsilon_F)$ ,  $g(\epsilon_F)$  being the density of single particle states at the Fermi energy [Boh99a].  $\Delta S$  is the ground state shell correction which is basically the difference of measured and calculated mass of a nucleus.  $U$  is the intrinsic excitation energy given by  $U = aT^2$  and  $\gamma$  is the shell damping factor which reflects the rate of shell effect depletion with excitation energy.

In this thesis, entropy density for finite nuclear matter has been experimentally determined by precisely measuring the nuclear level density parameter and nuclear temperature and compared with microscopic calculations performed using Eqs. (2.2) and (2.3).

### 2.3 Ratio of shear viscosity to the entropy density ( $\eta/s$ )

Experimentally it is observed that, for good fluids such as water, strongly coupled low-temperature quantum fluids ( $^4\text{He}$ ,  $^6\text{Li}$ ) [Rep64, Wil96, Har99, Blo08, Gio08], and the high-temperature quark-gluon-plasma (QGP) [Shu08, Adl03, Mas09, Aam10] produced at the Relativistic Heavy Ion Collider (RHIC) and the Large Hadron Collider (LHC), the shear viscosity differs by many orders of magnitude. For example, for  $^6\text{Li}$ ,  $\eta \sim 1.7 \times 10^{-15}$  Pa·s, while for QGP,  $\eta \sim 5 \times 10^{11}$  Pa·s [Sch09]. Due to this large variation in shear viscosity, one expresses the fluidity in terms of  $\eta/s$ . The reason could be qualitatively understood in the following way. From kinetic theory (though, it should be mentioned that kinetic theory might not be valid for systems like QGP and low-temperature

quantum fluids) the shear viscosity of a non-relativistic dilute gas is given by

$$\eta = \frac{1}{3}\rho m \bar{v} \lambda, \quad (2.7)$$

where  $\rho$  is the molecular density,  $m$  and  $\bar{v}$  are the mass and the average velocity of individual molecules, respectively, and  $\lambda$  is the mean free path. From Eq. (2.7) it is obvious that  $\eta/\rho$  could be a possible choice for a universal scale. It is also supported by the fact that the behavior of solutions of the Navier-Stokes equations is governed by the Reynolds number given by

$$Re = \frac{vL'}{\eta/\rho m}, \quad (2.8)$$

where  $v$  is the velocity of the fluid,  $L'$  is its characteristic length, and  $m$  is the mass of individual molecules. Larger is the value of  $Re$ , larger is the fluidity. From Eqs. (2.7) and (2.8) it is obvious that  $\eta/\rho$  could be a reasonable parameter for representing the fluidity of non-relativistic fluids. It is also observed that for such systems the entropy density  $s \sim \rho k_B$ . Therefore, one can use  $\eta/s$  as a measure of fluidity for non-relativistic fluids.

For a relativistic fluid,  $\eta/s$  is a necessary parameter for representing fluidity because for such a fluid the number of particles is not conserved. In QGP, for example, only the net number of quarks (the number of quarks minus the number of anti-quarks) is well defined, but the number of quarks or the number of gluons is not. The Reynolds number of a relativistic fluid is defined in terms of  $\eta/sT$ , where  $T$  is the temperature [Sch09]. From the above discussions, therefore, one could see that  $\eta/s$  represents a good measure of fluidity both for relativistic and non-relativistic fluids.

### 2.3.1 Importance of $(\eta/s)$

The quantity  $\eta/s$  is important in relation to the liquid-gas phase transition in matter. For several systems, it is observed [Fig. (2.2)] that  $\eta/s$  shows a

minimum at the transition point. Another crucial importance of  $\eta/s$  comes from the demonstration of Kovtun, Son, and Starinets [Kov05] that, for certain supersymmetric gauge theories, the ratio of shear viscosity to entropy density is given by

$$\frac{\eta}{s} = \frac{\hbar}{4\pi k_B}. \quad (2.9)$$

The authors have also conjectured, from the Heisenberg uncertainty principle, that this ratio is the lower bound of  $\eta/s$  for all systems. From Eq. (2.7) one can see that  $\eta \sim \rho m \bar{v} \lambda \sim \rho m \bar{v}^2 t_f \sim \rho E_k t_f$ , where  $E_k$  and  $t_f$  are the mean kinetic energy of individual molecules and the mean free time between collisions, respectively. On the other hand, entropy density  $s \sim \rho k_B$ . Therefore,  $\eta/s \sim (E_k t_f)/k_B$ . Since  $E_k t_f \geq \hbar$ ,  $\eta/s \geq \hbar/k_B$ . Therefore, from the uncertainty principle along with Eq. (2.9), it is evident that  $\eta/s \geq \hbar/4\pi k_B$ . The fluids which obey Eq. (2.9) are called perfect fluids.

The conjecture is also supported by another calculation [Kov05, Buc05] which gives

$$\frac{\eta}{s} = \frac{\hbar}{4\pi k_B} \left[ 1 + \frac{135\xi(3)}{8(2g^2 N_c)^{3/2}} + \dots \right], \quad (2.10)$$

where  $\xi(3)$  is the Apery's constant and  $g^2 N_c$  is the 't Hooft coupling. As can be seen from Fig. (2.3) that  $\eta/s$  approaches the lower bound of  $\hbar/4\pi k_B$  for large  $g^2 N_c$ .

The conjecture of Kovtun, Son, and Starinets has attracted a lot of theoretical and experimental efforts in different areas of physics [Sch09, Che07, Liu06, Sch07, Lah07]. People have tried to find out whether there exists a perfect fluid and whether they follow the KSS conjecture. Although, there are some theoretical counterexamples [Coh07, Che08, Cre11], no fluid that violates the KSS conjecture has been found experimentally. Moreover it is observed that

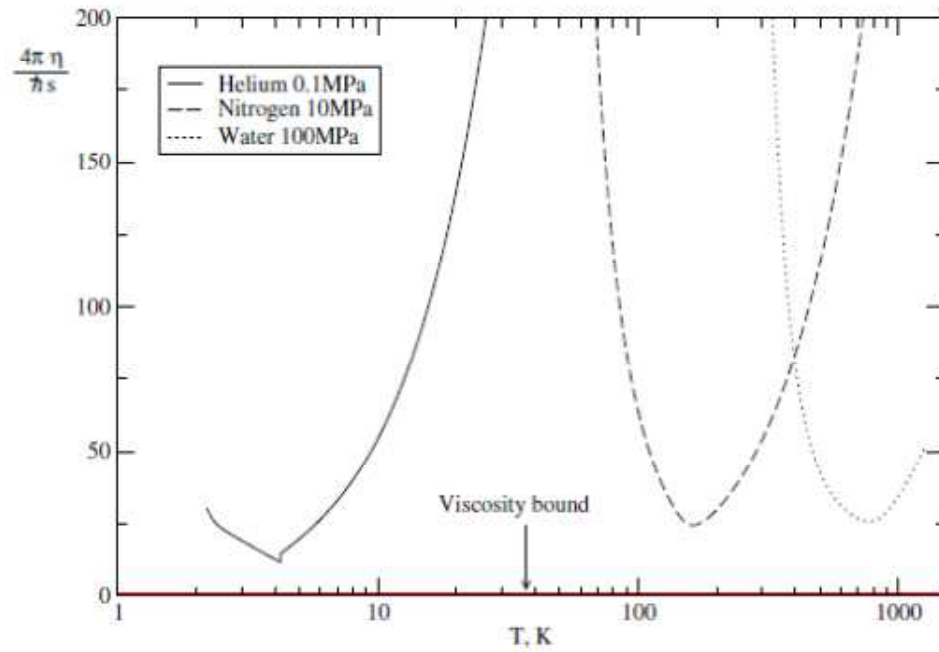


Figure 2.2: Variation of  $\eta/s$  with temperature (adopted from Ref. [Kov05]).

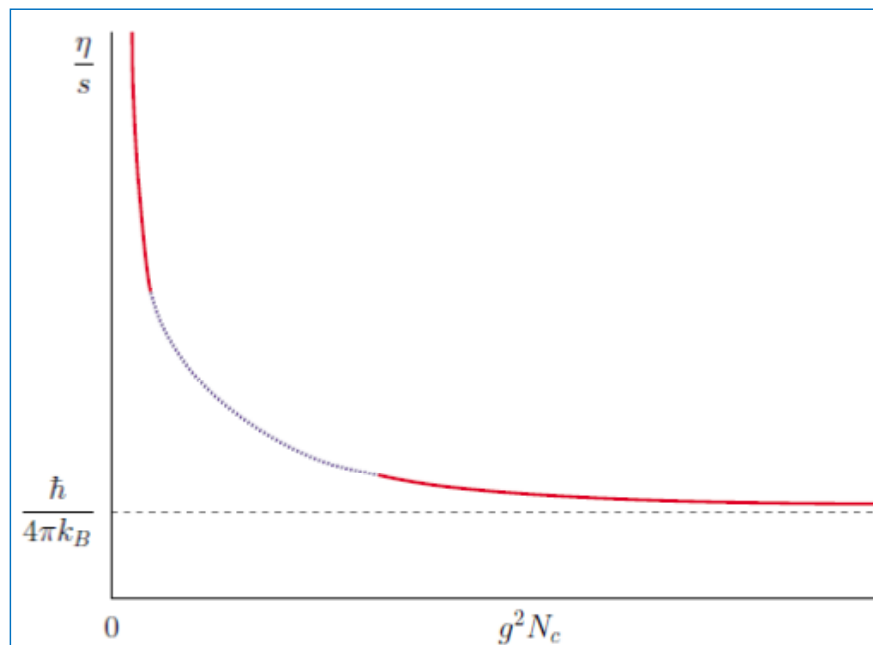


Figure 2.3: Dependence of the ratio  $\eta/s$  on  $g^2 N_c$  (adopted from Ref. [Kov05]).

strongly coupled systems such that low-temperature quantum fluids and high-temperature QGP have very small  $\eta/s$  ( $\sim 5-10 \hbar/4\pi k_B$ ) [Sch09] characteristic of a good fluid.

## 2.4 $\eta/s$ for finite nuclear matter

An atomic nucleus is a many-body quantum system in which the constituent particles, called nucleons, are governed by strong interaction. There is a strong affinity of the matter produced by ultrarelativistic collisions at RHIC and LHC and the conventional nuclear matter. The same forces are active in both the systems and the matter at RHIC and LHC is created due to the interaction of finite nuclei. A finite nucleus, therefore, is an ideal system to search for near perfect fluidity in matter as is observed for the matter produced at RHIC and LHC.

Over the years, people have performed different model-dependent theoretical calculations for shear viscosity, entropy density, and the ratio of these two quantities for finite nuclear matter. P. Danielewicz has derived an analytical relation of shear viscosity for nuclear matter using Uhlenbeck-Uehling equation [Dan84]. In recent years, various model-dependent calculations of  $\eta/s$  have been performed. S. Pal has done the calculations for  $\eta/s$  within an extended statistical multifragmentation model for an equilibrated system of nucleons and fragments produced in multifragmentation [Pal10]. The calculations show that the temperature variation of  $\eta/s$  has similar behavior to that of water and a minimum, characteristic of a liquid-gas phase transition, is observed. In a series of papers [Li11, Zho13, Fan14, Zho14, Den16], the group at the Shanghai Institute of Applied Physics, China has calculated the temperature variation of  $\eta/s$  for an evolving nucleus using various transport models, namely, Boltzmann-Uheling-

Uhlenbeck (BUU) model, extended BUU or van der Waals BUU(VdWBUU) model, isospin dependent Quantum Molecular Dynamic (IQMD) model etc. These calculations show that  $\eta/s$  values for finite nuclear matter are not very different from that of the QGP.

### 2.4.1 Shear viscosity and giant resonances

Viscosity is inherently related to the damping of giant resonances, which is conceived, macroscopically, as in-phase (isoscalar) and out of phase oscillation (isovector) of the proton and neutron fluids. It is seen that the ground state width of the GRs increases with the decrease in mass number of the nucleus. This suggests that the damping mechanism of the GRs is indeed similar to that of a viscous fluid where the modulus of decay ( $\tau$ ) (resonance width is inversely proportional to  $\tau$ ) of the oscillation decreases with the decrease in system volume [Lam32]. In the hydrodynamic description of giant resonances proposed by Auerbach and Yeverechyahu [Aue75], the viscosity of nuclear fluids provides the main mechanism for the damping of the giant states. The viscosity causes the energy of the collective mode to be dissipated into many noncoherent (single particle) modes, and thus describes the damping of the waves. In their model, the authors described the slow motion of neutron and proton fluids using the linearized Navier-Stokes equations. The application of proper boundary conditions yields the following equations

$$1 - \frac{Lj_L(K_I R)}{K_I R j_{L+1}(K_I R)} = \frac{(L+1)j_L(h_I R)}{h_I R j_{L+1}(h_I R)}, \quad (2.11)$$

where

$$K_I^2 = \frac{\omega^2 - i\omega\gamma'\delta_{i,1}}{u_I^2 + \frac{4}{3}i\nu\omega}, \quad (2.12)$$

$$h_I^2 = -(i\omega + \gamma'\delta_{i,1})/\nu.$$

Here  $L$  is the multipolarity,  $K_I$  is the wave number,  $R$  is nuclear radius given by  $R = R_0 A^{1/3}$ ,  $R_0$  being 1.2 fm,  $I$  is the isospin of excitation (for isovector excita-

tion  $I=1$  and for isoscalar excitation  $I=0$ ),  $u_t$  is the velocity of wave propagation (for isoscalar excitation  $u_0=0.126c$  and for isovector excitation  $u_1=0.241c$ ,  $c$  being the velocity of light in free space),  $\nu$  is the kinematic viscosity related to shear viscosity by  $\eta = \rho_m \nu$  and  $\gamma'$  is the mutual viscosity as the authors call it.  $j_L$  is the spherical Bessel's function of order  $L$ . For a definite multipolarity  $L$  and isospin of excitation  $I$ , Eq. (2.11) along with Eq. (2.12) can be solved for  $\omega$ . In general,  $\omega$  is a complex number. The real part of  $\omega$  ( $\omega_r$ ) is related to energy of the excitation by  $E = \hbar\omega_r$  and the imaginary part ( $\omega_i$ ) is related to the width by  $\Gamma = 2\hbar\omega_i$ . It is observed that the width of isoscalar resonances is solely dependent on  $\nu$ , while that of isovector resonances is related to both  $\nu$  and  $\gamma'$ . The authors of Ref. [Aue75] found  $\nu=0.6 \times 10^{22} \text{ fm}^2 \cdot \text{sec}^{-1}$  and  $\gamma'=0.35 \times 10^{22} \text{ sec}^{-1}$  by equating the experimental widths of isoscalar giant quadrupole resonance ( $\sim 3 \text{ MeV}$ ) and isovector giant dipole resonance ( $\sim 4 \text{ MeV}$ ) of  $^{208}\text{Pb}$  with the theoretical ones, respectively.  $\nu=0.6 \times 10^{22} \text{ fm}^2 \cdot \text{sec}^{-1}$  corresponds to  $\eta = \rho_m \nu = 1u$ , where  $u=10^{-23} \text{ MeV} \cdot \text{sec} \cdot \text{fm}^{-3}$  with  $\rho = \rho_m/m = 0.16 \text{ fm}^{-3}$ .

Recently, Auerbach and Sholomo [Aue09] have extended the earlier work of Auerbach and Yeverechyahu [Aue75]. The authors have calculated shear viscosity within a generalized Fermi liquid drop model [Aue09, Kol04] by employing a collision kinetic equation, which properly accounts for the dissipative propagation of sound waves in finite nuclei. According to this model, for a temperature  $T < \epsilon_F$  and excitation energy  $\hbar\omega < \epsilon_F$  of the sound wave, the shear viscosity is given by

$$\eta = \frac{2}{5} \rho \epsilon_F \frac{\tau_{\text{coll}}}{1 + (\omega \tau_{\text{coll}})^2}, \quad (2.13)$$

where  $\tau_{\text{coll}}$  is the Landau approximation for the collision relaxation time de-

ducted from the collision integral and is given by

$$\begin{aligned}\tau_{\text{coll}} &= \frac{\tau_0}{1 + (\hbar\omega/2\pi T)^2}, \\ \tau_0 &= \hbar\alpha/T^2.\end{aligned}\tag{2.14}$$

The parameter  $\alpha$  depends on the in-medium nucleon-nucleon scattering cross section and for isoscalar and isovector resonances its value is 9.2 and 4.6 MeV, respectively [Kol04].

In a recent work [Dan11], Dang has proposed a formalism, based on the Green-Kubo relation and the fluctuation dissipation theorem (FDT) [Kub57, Kub66], relating the shear viscosity to the width and the energy of giant dipole resonance (GDR) in hot finite nuclei. A qualitative relation between shear viscosity and the damping of the GDR can be envisaged by the arguments of Auerbach and Yeverechyahu [Aue75]. According to the authors viscosity causes the energy of the GDR to be dissipated in many non-coherent single-particle states and as pointed out in section 1.3.2, the coupling of the GDR state with the non-coherent states is responsible for the damping of the GDR. Thus one can draw a qualitative relation between the damping of the GDR and shear viscosity at finite temperature.

A quantitative relation between shear viscosity and the GDR parameters (especially width) is obtained by the FDT and the Green-Kubo relation. The FDT says the linear response of a given system to an external perturbation is expressed in terms of fluctuation properties of the system in thermal equilibrium. It basically manifests the internal relationship between the systematic and the random parts of microscopic forces and is realized by making use of the Green-Kubo formula which is an exact expression of the linear transport parameter at a given temperature and density in terms of time dependence of equilibrium fluctuations in the conjugate flux. According to this formula shear

viscosity at temperature  $T$  is related to the shear stress tensor by the following way

$$\eta(T) = \lim_{\omega \rightarrow 0} \frac{1}{2\omega} \iint dt dx e^{i\omega t} \langle [T_{xy}(t, x), T_{xy}(0, 0)] \rangle, \quad (2.15)$$

where the average is carried out within an equilibrium statistical ensemble.

From the FDT it is observed that

$$\begin{aligned} \eta(T) &= \lim_{\omega \rightarrow 0} \frac{1}{2\omega i} [G_A(\omega) - G_R(\omega)], \\ &= \lim_{\omega \rightarrow 0} \frac{\text{Im } G_R(\omega)}{\omega}, \\ &= \lim_{\omega \rightarrow 0} \frac{\sigma(\omega, T)}{C}, \end{aligned} \quad (2.16)$$

where  $G_A(\omega)$  and  $G_R(\omega)$  are the advanced and retarded Green functions, respectively, with  $G_R(\omega) = -i \iint dt dx e^{i\omega t} \theta(T) \langle [T_{xy}(t, x), T_{xy}(0, 0)] \rangle$ ,  $G_A(\omega)$  is the complex conjugate of  $G_R(\omega)$  and  $C$  is a constant. It should be mentioned that Eqs. (2.15) and (2.16) have been utilized to derive the KSS conjecture [Kov05] where  $\sigma(\omega, T)$  was the graviton absorption cross section. For finite nucleus, the line shape of GDR is expressed in terms of a Lorentzian cross section given by

$$\sigma(\omega, T) = \sigma' \frac{\Gamma_{\text{GDR}} \omega^2}{[\omega^2 - E_{\text{GDR}}^2]^2 + \omega^2 \Gamma_{\text{GDR}}^2}. \quad (2.17)$$

Note that the  $T$  dependence in  $\sigma(\omega, T)$  comes mainly from the  $T$  dependence of  $\Gamma_{\text{GDR}}$ . Here,  $\Gamma_{\text{GDR}}$  and  $E_{\text{GDR}}$  are the width and the energy of the GDR. It should be mentioned that  $\omega$  and  $E_{\text{GDR}}$  have the same unit. Incorporating the photoabsorption cross section given by Eq. (2.17) in Eq. (2.16), Dang has obtained the following expression for shear viscosity at finite  $T$

$$\eta(T) = \eta(0) \frac{\Gamma_{\text{GDR}}(T)}{\Gamma_{\text{GDR}}(0)} \left\{ \frac{E_{\text{GDR}}(0)^2}{E_{\text{GDR}}(0)^2 - [\Gamma_{\text{GDR}}(0)/2]^2 + [\Gamma_{\text{GDR}}(T)/2]^2} \right\}^2, \quad (2.18)$$

where  $\eta(0)$  is the shear viscosity at zero temperature. The author has also given an alternative prescription for  $\eta(T)$  by incorporating a Breit-Wigner photoabsorption cross section given by

$$\sigma(\omega, T) = \sigma'' \frac{\Gamma_{\text{GDR}}/2}{[\omega - E_{\text{GDR}}]^2 + [\Gamma_{\text{GDR}}/2]^2}. \quad (2.19)$$

In this case shear viscosity is given by

$$\eta(T) = \eta(0) \frac{\Gamma_{\text{GDR}}(T)}{\Gamma_{\text{GDR}}(0)} \frac{E_{\text{GDR}}(0)^2 + [\Gamma_{\text{GDR}}(0)/2]^2}{E_{\text{GDR}}(T)^2 + [\Gamma_{\text{GDR}}(T)/2]^2}. \quad (2.20)$$

The author has compared the outcome of these two prescriptions and observed that both give nearly the same results. However, in this thesis, the prescription derived using a Lorentzian cross section has been utilized because the GDR parameters have been extracted experimentally by incorporating a Lorentzian photoabsorption cross section in the statistical model calculations (section 4.2).

## 2.5 Motivation of the present work

As has been mentioned earlier, the conjecture of Kovtun, Son, and Starinets stimulated a lot of works, both theoretical and experimental, in different areas of physics in search for perfect fluidity in matter. The results for QGP and low-temperature quantum fluids show that strongly coupled systems have very small values of  $\eta/s$ . This motivated Auerbach and Sholomo for their pioneering theoretical work regarding the value of  $\eta/s$  for finite nuclear matter in which the nucleons are governed by strong interaction. The authors showed that  $\eta/s$  values for heavy and light nuclei were  $\sim (4-19) \hbar/4\pi k_B$  and  $\sim (2.5-12.5) \hbar/4\pi k_B$ , respectively. From their results, the authors gave a bold conjecture that the strong fluidity is a characteristic feature of the strong interaction of the many-body nuclear systems in general and not just of the state created in the relativistic collisions. The theoretical work of Dang also resulted in a similar conclusion. These theoretical results motivated us to carry out a self-consistent, systematic experimental investigation for the ratio of shear viscosity to entropy density in finite nuclear matter. The principal objective was to exclusively probe the quantities required for determining  $\eta/s$ . By self-consistent it is meant that the quantities required for the extraction of shear viscosity were

determined simultaneously with the quantities required for determining entropy density and these quantities are inter-related. With these motivations and objectives, a thorough experimental investigation for  $\eta$ ,  $s$ , and thus,  $\eta/s$  has been performed for equilibrated finite nuclear systems from  $A \sim 30$  to  $A \sim 208$  at different temperatures. The shear viscosity has been extracted by utilizing the  $\gamma$  decay of the isovector giant dipole resonance (prescription of Ref. [Dan11]) and the entropy density has been evaluated from the nuclear level density parameter and nuclear temperature, determined precisely by simultaneous measurements of evaporated neutron energy spectra and the compound nuclear angular momenta. It should be highlighted that this is the first experimental determination of  $\eta/s$  for finite nuclear matter.

# Chapter 3

## Isospin Formalism and Isospin Mixing

### 3.1 Isospin formalism

The concept of charge symmetry (neutron-neutron and proton-proton forces are identical) and charge independence (neutron-neutron, proton-proton and neutron-proton forces are identical) was mathematically formalized by Heisenberg by the introduction of isospin quantum number [Hei32]. In this formalism, the neutron and the proton are considered as two states of the same particle called nucleon. The mathematical formalism of isospin is similar to that of spin. The isospin operator  $\hat{\mathbf{i}}$  is a set of three operators  $\{\hat{\mathbf{i}}_x, \hat{\mathbf{i}}_y, \hat{\mathbf{i}}_z\}$  and acts in the charge or isospin space. Acting on a state of good isospin having quantum number  $i$  and  $i_z$ , the operator  $\hat{\mathbf{i}}^2$  and  $\hat{\mathbf{i}}_z$  reproduce the same states with eigenvalues  $i(i+1)$  and  $i_z$ , respectively

$$\begin{aligned}\hat{\mathbf{i}}^2 |i, i_z\rangle &= i(i+1) |i, i_z\rangle , \\ \hat{\mathbf{i}}_z |i, i_z\rangle &= i_z |i, i_z\rangle .\end{aligned}\tag{3.1}$$

Like spin, an isospin state with quantum number  $i$  can have  $(2i+1)$  projections. For nucleon  $i = 1/2$  and the neutron and proton are the two states of the nucleon

having projections  $i_z = +1/2$  and  $i_z = -1/2$ , respectively. The isospin analog of Pauli spin matrix is defined as  $\hat{\mathbf{i}}_3 = 2\hat{\mathbf{i}}_z$ . The eigenvalue of  $\hat{\mathbf{i}}_3 \equiv i_3 = 2i_z$ .

A nucleus comprises of many nucleons. For such a system, the isospin operator and its projection are defined as

$$\begin{aligned}\hat{\mathbf{I}} &= \sum_j \hat{\mathbf{i}}^j, \\ \hat{\mathbf{I}}_z &= \sum_j \hat{\mathbf{i}}_z^j,\end{aligned}\tag{3.2}$$

and the following relations hold

$$\begin{aligned}\hat{\mathbf{I}}^2 |I, I_z\rangle &= I(I+1) |I, I_z\rangle, \\ \hat{\mathbf{I}}_z |I, I_z\rangle &= I_z |I, I_z\rangle.\end{aligned}\tag{3.3}$$

For a nucleus with  $Z$  protons and  $N$  neutrons,  $I_z = (N - Z)/2$  and it basically defines the nucleus.  $I_z$  can have  $(2I+1)$  values from  $-I$  to  $+I$  for a given  $I$ . These states of the same isospin but with different projections are called the isobaric analog states (IAS). The state with higher value of  $I_z$  is called parent state, while that with lower value of  $I_z$  is called daughter state which can be obtained by operating the parent state by isospin ladder operator. For a give  $I_z$  i.e. for a given nucleus, the isospin quantum number can have values from  $|I_z|$  to  $A/2 = (N + Z)/2$ , where  $A$  is the mass number of the nucleus. It is observed that, apart from a few exceptions such as  $^{34}\text{Cl}$ ,  $^{42}\text{Sc}$ , and  $^{46}\text{V}$ , nuclear interactions favor the lowest possible isospin state as the ground state of nucleus. The detailed discussions on isospin and related aspects could be found in Ref. [Wil69].

## 3.2 Isospin mixing

The charge independence of nuclear force guarantees that, along with space and spin quantum numbers, each nuclear state can be assigned with isospin ( $I$ ) and

its projection ( $I_z$ ). However, the presence of different electromagnetic interactions e.g. Coulomb force, spin-orbit coupling and the charge-dependent part of nuclear interaction mixes the pure isospin states [Wil69]. The Coulomb potential has three parts; isoscalar, isovector, and isotensor Coulomb interactions. The off-diagonal matrix element for isoscalar part vanishes. Therefore, it cannot connect the states of different isospins. The isotensor part connects isospin states separated by  $\Delta\mathbf{I}=2$ . The contribution of this part is very small. The most important isospin violating part is the isovector Coulomb interaction given by  $V_c^1 = -Ze^2/4R \sum_j v_3^j [3 - (r_j/R)^2]$  inside the nucleus, where  $R$  is the nuclear radius. It conserves the angular momentum and parity and connects the isospin states separated by  $\Delta\mathbf{I}=1$ . In this thesis, the mixing between  $I_< \equiv |I, I = I_z\rangle$  and  $I_> \equiv |I + 1, I = I_z\rangle$  states will be considered. The symbol  $\alpha_<^2$  denotes the fraction of  $I_<$  state that mixes with  $I_>$  state and  $\alpha_>^2$  represents the fraction of  $I_>$  state that mixes with  $I_<$  state.

### 3.2.1 Expected variation of isospin mixing with excitation energy or temperature

First order perturbation theory gives

$$\alpha_>^2 = \sum_{I+1} \frac{|\langle I + 1, I = I_z | V_c^1 | I, I = I_z \rangle|^2}{[E_{I+1} - E_I]^2}. \quad (3.4)$$

As the separation energy  $\Delta I = E_{I+1} - E_I$  is large at the ground state and extremely low excited states, isospin mixing is small ( $\sim 5\%$  for  $N=Z=50$ ) at these low energies. As excitation energy gradually increases, the states come closer. However, the states attain intrinsic decay width ( $\Gamma^\uparrow$ ) which increases exponentially with the increase in excitation energy. In this case, the generalized perturbation theory yields [Lev82]

$$\alpha_>^2 = \sum_{I+1} \left| \frac{\langle I + 1, I = I_z | V_c^1 | I, I = I_z \rangle}{[(E_{I+1} + i\Gamma_{I+1}^\uparrow/2) - (E_I + i\Gamma_I^\uparrow/2)]} \right|^2. \quad (3.5)$$

In the low and intermediate excitation energies one can neglect the intrinsic width compared to energy spacing the of states. As the spacing decreases with the increase in excitations, the denominator in Eq. (3.5) decreases resulting in larger isospin mixing. However, when  $\Gamma^\uparrow$  becomes comparable to the level spacing, the denominator in Eq. (3.5) becomes important and leads to the decrease in  $\alpha^2$ . In the statistical region,  $|I + 1, I = I_z\rangle$  state remains embedded in a large ensemble of  $|I, I = I_z\rangle$  states having nearly the same energy. If  $D$  be the average spacing of  $|I, I = I_z\rangle$  states and  $v'$  be the average matrix element between  $|I, I = I_z\rangle$  and  $|I + 1, I = I_z\rangle$  states, the probability of  $|I + 1, I = I_z\rangle$  state per unit energy interval of the spectrum at energy  $E$  is given by [Boh99a]

$$P_{I+1}(E) = \frac{1}{2\pi} \frac{\Gamma^\downarrow}{(E_{I+1} - E)^2 + (\Gamma^\downarrow/2)^2}, \quad (3.6)$$

where  $E_{I+1}$  is the energy of  $|I + 1, I = I_z\rangle$  state and  $\Gamma^\downarrow = 2\pi v'^2/D$  is the width of the distribution and is called Coulomb spreading width (to be more specific, it is the Coulomb spreading width of  $|I + 1, I = I_z\rangle$  state).

In time dependent picture, if a nucleus is populated in  $|I + 1, I = I_z\rangle$  state at  $t=0$ , then the amplitude of finding the system in  $|I + 1, I = I_z\rangle$  state at  $t=t$  is given by

$$A_{I+1}(t) \sim \exp \left[ -\frac{i}{\hbar} E_{I+1} t - \frac{\Gamma^\downarrow}{2\hbar} t \right]. \quad (3.7)$$

The state, therefore, decays or mixes with  $|I, I = I_z\rangle$  states with a time scale of  $\hbar/\Gamma^\downarrow$ . However, the state also decays by particle emission with a time scale of  $\hbar/\Gamma^\uparrow$ . Therefore, Wilkinson suggested that, at high excitations, an appropriate measure of isospin mixing is given by [Wil56]

$$\alpha^2 \sim \frac{\Gamma^\downarrow}{\Gamma^\uparrow}. \quad (3.8)$$

It is observed that  $\Gamma^\downarrow$  does not change much with excitation energy or nuclear mass [Kuh79, Hrn86]; but  $\Gamma^\uparrow$  increases exponentially with the increase in exci-

tation energy resulting in decrease in isospin mixing. Physically, the lifetime of the states becomes so small that they decay before the isospin degree of freedom has time to equilibrate and mix. Therefore, isospin mixing is expected to remain small at lower excitations, increase gradually and attain a maximum value in the intermediate region and decrease at high excitations.

### 3.2.2 Calculations of isospin mixing

Due to the importance of isospin mixing in nuclear phenomena as well as in other fundamental aspects in physics (section 3.2.3), theoretical calculations have been performed from very early days. People have calculated isospin mixing parameter in the ground state as well as in the excited states in nuclei utilizing different models. Some of them are briefly discussed below.

In very early days, William M. MacDonald calculated the isospin impurities in the ground state with the harmonic oscillator wave functions [Mac58]. In the macroscopic approach, Bohr and Mottelson gave an estimate of the ground state isospin mixing utilizing spherical hydrodynamic model by taking into account the polarization effects of isovector monopole modes [Boh99a]. In recent years, microscopic calculations are mainly based on limited single particle spaces within projected mean field approaches [Dob95, Col95]. Suzuki *et al.* have performed a calculation based on Feshbach projection method by connecting the spreading width of the isobaric analog state and isospin mixing in parent nucleus [Suz96]. In this thesis, we will utilize the recent calculation of Satula *et al.* [Sat09]. The authors have evaluated ground state isospin mixing, in a self-consistent non-perturbative way, within the extended mean-field approach utilizing SLy4 energy density functional (EDF) parameterization. Non-perturbative means the method fully takes into account long-range polarization effects associated with the Coulomb force and neutron excess. The prime ad-

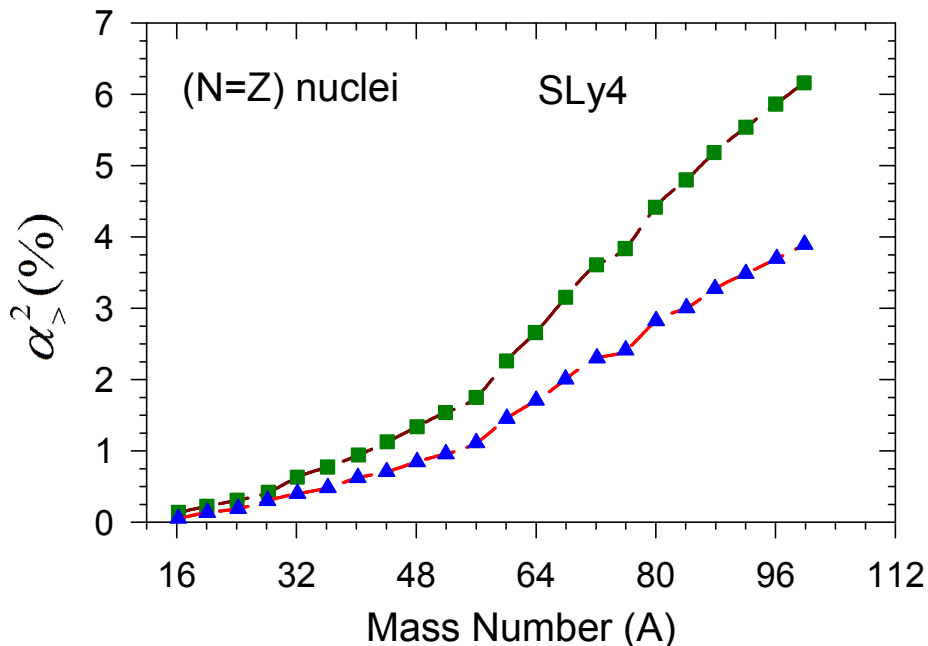


Figure 3.1: Variation of the ground state isospin mixing parameter with mass number for even-even  $N = Z$  nuclei. The plot [square (green) with dashed line] is devoid of spurious mixing while the same [triangle (blue) with dashed line] is affected by spurious mixing (adopted from [Sat09]).

vantage of this method is that, it eliminates the spurious mixing that leads to the suppression of Coulomb induced mixing in  $N=Z$  systems [Fig. (3.1)]. The calculation yields  $\alpha_{>}^2 \sim 0.7\%$  in the ground state of  $^{32}\text{S}$  nucleus.

Harney, Richter and Weidenmuller have developed a quantitative formulation for isospin mixing in compound nuclear reactions by  $S$ -matrix formalism [Hrn86]. The authors have considered the mixing between the states of two isospin classes ( $I_{<} \equiv |I, I = I_z\rangle$  and  $I_{>} \equiv |I + 1, I = I_z\rangle$ ). Following the arguments of Wilkinson, they have parameterized isospin mixing in terms of the Coulomb spreading width and the compound nuclear decay width. The fraction of  $\gtrsim$  states that mixes with  $\lesssim$  states is given by

$$\alpha_{\gtrsim}^2 = \frac{\Gamma_{\gtrsim}^{\downarrow}/\Gamma_{\gtrsim}^{\uparrow}}{1 + \Gamma_{\gtrsim}^{\downarrow}/\Gamma_{\gtrsim}^{\uparrow} + \Gamma_{\lesssim}^{\downarrow}/\Gamma_{\lesssim}^{\uparrow}}, \quad (3.9)$$

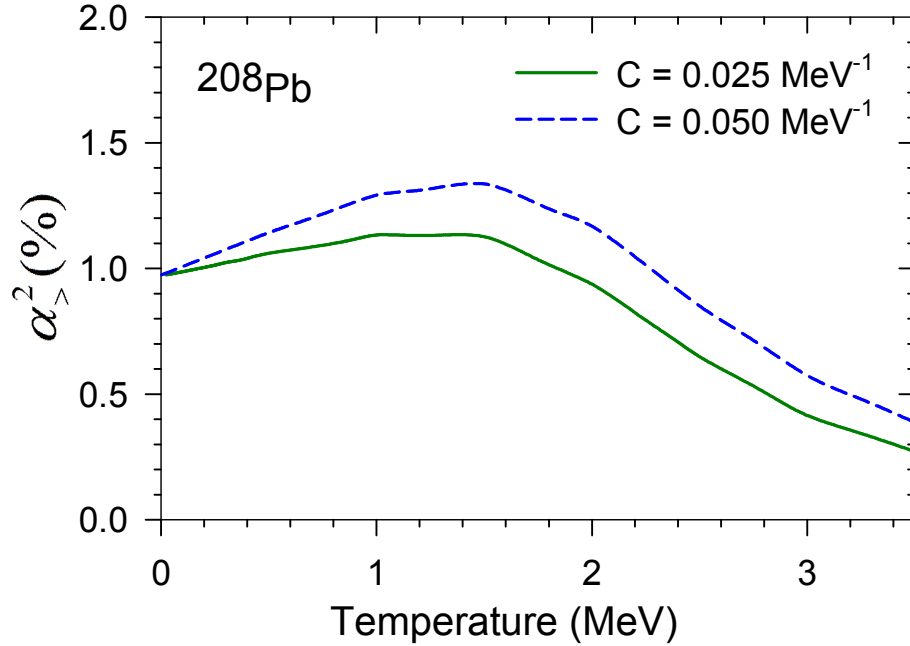


Figure 3.2: Variation of isospin mixing parameter with temperature in  $^{208}\text{Pb}$  according to Eq. (3.12). The solid [green] and the dashed [blue] lines correspond to two different values of constant  $c$  that gives a mild temperature dependence of  $\Gamma_{\text{IAS}}$  and  $\Gamma_{\text{M}}$  (adopted from [Sag98]).

where  $\Gamma^\downarrow$  and  $\Gamma^\uparrow$  are, respectively, the Coulomb spreading width and statistical decay width of the respective states. The details of this formalism will be discussed in section 4.4.2.

In another approach, Sagawa *et al.* have extended the formalism of Ref. [Suz96] at finite temperature by taking into account the intrinsic decay width of the states involved [Sag98]. According to this formalism, the dominant contribution in the spreading width of the isobaric analog states arises owing to the coupling with three components of the isovector giant monopole resonance (IVGMR) and it is expressed as

$$\Gamma_{\text{IAS}}^\downarrow = -2\text{Im} \sum_q \frac{|\langle \text{IAS} | H_1 | q \rangle|^2}{E^* - E_q + i\Gamma_c(E^*)/2 + i\Gamma_{\text{M}}(E^*)/2}, \quad (3.10)$$

where  $|\text{IAS}\rangle$  and  $|q\rangle$  are the eigenstates of fully charge independent nuclear

Hamiltonian.  $H_1$  is the isovector part of Coulomb interaction, charge symmetry breaking as well as the charge independence interactions.  $\Gamma_c$  and  $\Gamma_M$  are the compound width and the spreading width of  $I_0 + 1$  monopole state, respectively;  $I_0 = I_z$  being the isospin projection of parent state. The sum over  $q$  mainly runs over the three components of isospin  $I - 1$ ,  $I$  and  $I + 1$  of the IVGMR in the daughter nucleus having energies  $E_q$ . After some simplifications, Eq. (3.10) can be written as

$$\Gamma_{\text{IAS}}^\downarrow = [\Gamma_c(E^*) + \Gamma_M(E^*)](I_0 + 1)\alpha_{>}^2. \quad (3.11)$$

Eq. (3.11) can also be written as

$$\alpha_{>}^2 = \frac{1}{I_0 + 1} \frac{\Gamma_{\text{IAS}}^\downarrow}{\Gamma_c(E^*) + \Gamma_M(E^*)}. \quad (3.12)$$

$\Gamma_{\text{IAS}}$  and  $\Gamma_M$  are nearly temperature independent; but  $\Gamma_c$  increases exponentially with temperature resulting in a decrease in isospin mixing with the increase in temperature. The authors have also prescribed a mild temperature dependence of  $\Gamma_{\text{IAS}}^\downarrow$  and  $\Gamma_M$  as  $\Gamma^\downarrow(T) = \Gamma^\downarrow(0)[1 + cT]$ . Fig. (3.2) shows the calculations of isospin mixing parameter for  $^{208}\text{Pb}$  utilizing this prescription.

In this thesis, we have utilized the prescription of Harney, Richter and Weidenmuller to extract isospin mixing in  $^{32}\text{S}$  using compound nuclear reactions and tried to extrapolate it towards zero temperature with the formalism of Sagawa *et al.* with several simplifying assumptions.

### 3.2.3 Importance of isospin mixing

The importance of isospin mixing can be summarized as follows

- (a) It gives a measure of the importance of charge symmetry and charge independence breaking interactions in nuclear phenomena.

- (b) As is observed from Eq. (3.12), isospin mixing parameter is related to the spreading width of the IAS and the width of the IVGMR. Therefore, one can have an idea about the width of the IAS or IVGMR knowing all other quantities in Eq. (3.12). It is observed experimentally that the width of the IAS is very small which can be attributed to the small value of the isospin mixing parameter.
- (c) The importance for determining isospin mixing mostly lies in its relation in finding the corrected comparative half-life ( $Ft$ ) from the measured  $ft$  values of superallowed  $\beta$  decay between nuclear analog states of spin  $J^\pi = 0^+$  and isospin  $I = 1$ . Here  $f$  is the statistical rate function dependent on proton number of daughter nucleus and measured total transition energy ( $Q_{\text{EC}}$ ). The quantity  $t$  is the partial half-life for the transition, which is obtained from the measured half-life ( $t_{1/2}$ ) of the parent nucleus corrected for the branching ratio of the transition ( $R$ ) and the electron capture fraction ( $P_{\text{EC}}$ ) and is given by  $t = (1 + P_{\text{EC}})t_{1/2}/R$ . The corrections in  $ft$  values are required to eliminate the effects of radiative processes (radiative corrections) and presence of isospin impurities in the parent and the daughter states (isospin symmetry-breaking corrections). Hardy and Towner defined corrected  $ft$  value as [Har05a, Har05b, Tow10, Har15]

$$Ft \equiv ft(1 + \delta'_R)(1 + \delta_{\text{NS}} - \delta_c) = \frac{K}{2G_{\text{F}}^2 V_{\text{ud}}^2 (1 + \Delta_{\text{R}}^{\text{V}})}, \quad (3.13)$$

where  $\delta'_R$  and  $\delta_{\text{NS}}$  are the transition dependent part of radiative correction and  $\Delta_{\text{R}}^{\text{V}}$  is the transition independent part of radiative correction.  $\delta_c$  is the isospin-symmetry breaking correction defined as  $M_{\text{F}}^2 = (M_{\text{F}}^0)^2[1 - \delta_c]$ ,  $M_{\text{F}}^2$  and  $(M_{\text{F}}^0)^2$  being the transition matrix elements in presence and in absence of isospin mixing, respectively.  $K$  is a constant given by  $K/(\hbar c)^6 = 2\pi^3 \hbar \ln 2 / (m_e c^2)^5 = 8120.2776(9) \times 10^{-10} \text{ GeV}^{-4}\text{s}$ .  $G_{\text{F}}$  is

the weak-interaction constant for pure leptonic muon decay given by  $G_F/(\hbar c)^3 = 1.1663787(6) \times 10^{-5} \text{ GeV}^{-2}$ .  $V_{ud}$  is the up-quark to down-quark transition matrix element in the Cabibbo-Kobayashi-Maskawa (CKM) Matrix, whose unitarity validates the standard model. The isospin symmetry breaking correction  $\delta_c$  is related to the isospin mixing parameter by the following relation [Aur09].

$$\delta_c = 4(I + 1) \frac{V_1}{41\xi A^{2/3}} \alpha_{>}^2, \quad (3.14)$$

where  $V_1 = 100 \text{ MeV}$  and  $\xi = 3$ . From Eqs. (3.13) and (3.14), it is observed that by calculating the radiative corrections and determining the isospin mixing parameter, one can deduce  $Ft$  and hence  $V_{ud}$ . However, to find  $V_{ud}$  one needs isospin mixing parameter at the ground state of nucleus. Therefore, by finding the isospin mixing in higher temperature, one can extrapolate it towards zero temperature using some suitable formalism. For radioactive nuclei, which is not accessible in the ground state, this provides an important technique to find isospin mixing in zero temperature [Cer15]. Also, For stable nuclei, this gives an alternative approach to extract isospin mixing in the ground state.

In this thesis, we will attempt to extrapolate  $\alpha_{>}^2$  towards zero temperature from our measured  $\alpha_{>}^2$  for  $^{32}\text{S}$  at high temperature utilizing the prescription of Sagawa *et al.* [Sag98]. It should be explicitly mentioned that  $\delta_c$  depends on the particular states involved in superallowed  $\beta$  decay. In addition, our measured data is not sensitive enough to draw any particular conclusion about the unitarity of the CKM matrix. However, the extracted data will provide some idea about the order of magnitude for isospin symmetry breaking correction in this mass region.

### 3.2.4 Tools for measurement of isospin mixing

In general, isospin mixing can be studied by utilizing the transitions which would have been forbidden in the absence of isospin mixing. For example,

- (a) Electric dipole transition in self-conjugate nuclei [Far03]
- (b) Splitting of the IAS studied by  $\beta$ -delayed  $\gamma$  rays [Van13]
- (c) Evaporated  $E1$   $\gamma$  rays from the decay of isovector giant dipole resonance (IVGDR) in self-conjugate nuclei [Har86].

In this thesis, the  $\gamma$  decay of IVGDR has been utilized to extract the isospin mixing parameter in  $^{32}\text{S}$  at high excitations.

## 3.3 Isospin selection rule for IVGDR $\gamma$ ray transitions

The isovector operator that connects the initial state and the final state to be populated by the  $E1$   $\gamma$  decay is given by  $\hat{\mathbf{O}}_{\mathbf{E}}^{\text{IV}}(L, M) = -\frac{1}{2}\hat{\mathbf{e}} \sum_{k=1}^A \hat{\mathbf{i}}_{3k} \tau_k^L Y_{LM}(\Omega_k)$ , with  $L = 1$  and  $M = -1, 0$  and  $+1$ . It is observed that the transition matrix element  $M_{\text{if}}$  between the initial state  $|\nu_i, I_i, I_z\rangle$  and the final state  $|\nu_f, I_f, I_z\rangle$  for such an operator is non-zero only for  $\Delta I = 0, \pm 1$  [Wil69],  $\nu$  being the space and spin quantum numbers. For  $\Delta I = \pm 1$

$$M_{\text{if}} \propto \left[ \frac{I_{\text{la}}^2 - I_z^2}{I_{\text{la}}(2I_{\text{la}} - 1)(2I_{\text{la}} + 1)} \right]^{1/2}, \quad (3.15)$$

where  $I_{\text{la}}$  is the larger of  $I_i$  and  $I_f$ . For  $\Delta I = 0$  i.e.  $I_i = I_f$

$$M_{\text{if}} \propto \frac{I_z}{\left[ I_i(I_i + 1)(2I_i + 1) \right]^{1/2}}. \quad (3.16)$$

Therefore, it is obvious from Eq. (3.16) that for a self-conjugate nucleus ( $N = Z$ ,  $I_z=0$ ) the transitions between the states of the same isospin are forbidden. However, all transitions are allowed in a non-self-conjugate nucleus ( $N \neq Z$ ,  $I_z \neq 0$ ). This selection rule is the mainstay for the study of isospin mixing in self-conjugate nuclei, and, in particular, for  $^{32}\text{S}$  in the present case.

### 3.4 Isospin splitting and Pauli blocking of GDR strength

Let us consider a nucleus of mass number  $A$  and isospin projection  $I_z$ . As mentioned earlier, the isospin quantum number for this nucleus can have values from  $I = |I_z|$  to  $I = A/2$ . In this thesis, we will consider only the states of isospin  $I = |I_z|$ ,  $I = |I_z| + 1$  and  $I = |I_z| + 2$ . The strength function of the GDR built on the state  $|\nu, I, I = I_z\rangle$  gets splitted into two components with isospin  $I$  and  $I + 1$  [Fal70, Aky71] [Fig. (3.3a)]. The splitting occurs owing to the competition between the symmetry energy and the difference in particle-hole interactions. Symmetry energy tends to move the states with higher isospin to higher energies while the latter tries to drag it to lower energies. The size of the energy splitting has been calculated by Akyuz [Aky71] and is given by

$$\begin{aligned} E_{I+1} - E_I &= \frac{U_D}{A}(I + 1), \\ E_D &= \frac{1}{I + 1}E_{I+1} + \frac{I}{I + 1}E_I, \end{aligned} \tag{3.17}$$

where  $E_I$  and  $E_{I+1}$  are the centroid energies of the GDR component with isospin  $I$  and  $I + 1$ ;  $U_D = 60$  MeV is the symmetry energy for dipole states and  $E_D$  is average energy of the total strength function (can be approximated by Eq. (1.6)). The strength distributions of the two components are given by the isospin Clebsch-Gordan coefficients multiplied by an additional factor arising from Pauli blocking of configurations reached by  $1p1h$  excitations and could be

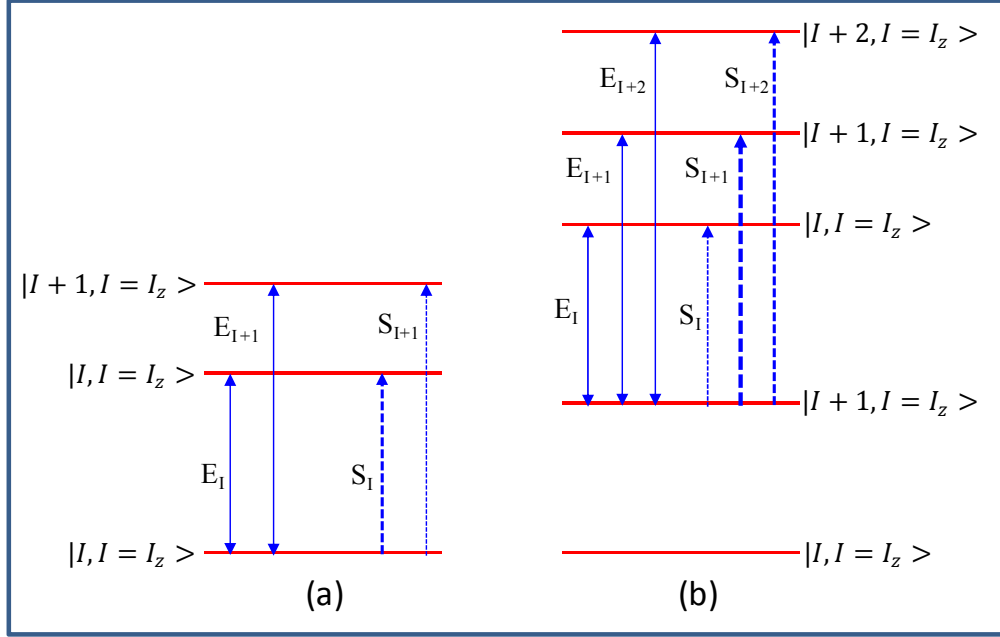


Figure 3.3: Schematic representation of isospin splitting of the GDR built on (a)  $|I, I = I_z\rangle$  (b)  $|I + 1, I = I_z\rangle$  states of the nucleus having isospin projection  $I_z$ .

expressed as follows [Fal70, Beh91]

$$S_I = \frac{I}{I+1} \left(1 + \frac{p_1}{I}\right), \quad (3.18)$$

$$S_{I+1} = \frac{1}{I+1} (1 - p_1), \quad (3.19)$$

where  $p_1 = 1.5IA^{-2/3}$  is the correction for Pauli blocking. Vergados extended this formalism to GDR built on excited states of nuclei [Ver75]. The GDR built on the state  $|\nu, I + 1, I = I_z\rangle$  is splitted into three components with isospins  $I$ ,  $I + 1$  and  $I + 2$  [Fig. (3.3b)]. The centroid energies of these components obey the following relations

$$E_{I''} - E_{I'} = \frac{U_D}{A} [I''(I'' + 1) - I'(I' + 1)]. \quad (3.20)$$

The strength distributions of the GDR components are given by [Ver75,

Beh91]

$$S_i = \frac{2I+1}{(I+1)(2I+3)} \left[ 1 + \frac{p_2(I+2)}{I+1} \right], \quad (3.21)$$

$$S_{i+1} = \frac{I^2}{(I+1)(I+2)} \left[ 1 + \frac{p_2}{I+1} \right], \quad (3.22)$$

$$S_{i+2} = \frac{4(I+1)}{(I+2)(2I+3)} \left[ 1 - p_2 \right], \quad (3.23)$$

where  $p_2 = 1.5(I+1)A^{-2/3}$  is the correction for Pauli blocking. From equations 3.18, 3.19, 3.21 to 3.23 it is obvious that for  $I = I_z \gg 0$ ,  $\Delta I = 0$  transition carries most of the strength and it remains completely absent in self-conjugate nuclei ( $I = I_z = 0$ ). These effects of isospin have indeed been observed experimentally in light and medium non-self-conjugate nuclei [Die71, Pau71, Pyw79, Bow82] and included in the statistical model calculations by Harakeh and Behr for analysis of the GDR built on the excited states of nucleus [Har86, Beh91, Beh93].

### 3.5 Previous experimental works and motivation for the present work

The pioneering work of isospin mixing utilizing the  $\gamma$  decay of the IVGDR was performed by Harakeh *et al.* [Har86]. The authors modified the usual statistical model code CASCADE [Pul77] to perform the calculations with good isospin and parity quantum numbers. Isospin dependent level densities were calculated and the transmission coefficients for both particle and  $\gamma$  decay were multiplied by proper Clebsch-Gordan coefficients (section 4.4). The mixing was done in level densities as follows

$$\begin{aligned} \tilde{\rho}_< &= (1 - \alpha^2)\rho_< + \alpha^2\rho_>, \\ \tilde{\rho}_> &= (1 - \alpha^2)\rho_> + \alpha^2\rho_<, \end{aligned} \quad (3.24)$$

where  $\rho$  and  $\tilde{\rho}$  are the pure and mixed level densities and  $\alpha^2$  is the isospin mixing parameter given by  $\alpha^2 = a + bE^*$ , where  $E^*$  is the excitation energy,  $a$  and  $b$  are free parameters determined from the experimental data. Utilizing this formalism the authors extracted  $\alpha^2 = 3.2\%$  for  $^{28}\text{Si}$  at  $E^* = 34$  MeV. Later, Behr *et al.* [Beh93] modified the mixing formalism. Instead of mixing the level densities, the authors mixed the population matrix according to the formalism of Ref. [Hrn86] (section 4.4.2) where the isospin mixing parameter was calculated by using Eq. (3.9). The authors showed, by inclusive  $\gamma$  ray measurements, that for  $^{28}\text{Si}$ , isospin gradually becomes a good quantum number as excitation energy increases. However, though with large errors, opposite result was found for  $^{26}\text{Al}$ . Kicinska-Habior and collaborators at Warsaw university, Poland have performed some measurements [Hab04, Hab05, Woj06, Woj07] and showed that isospin mixing increases with the increase in the mass number and the atomic number. However, as isospin mixing depends on both temperature and atomic number, one should vary only one parameter at a time. Recently, Corsi [Cor11] and Ceruti [Cer15] have performed interesting works regarding the isospin mixing in  $^{80}\text{Zr}$ . They concluded that the Coulomb spreading width, in fact, remains constant with temperature and isospin mixing decreases with the increase in temperature. The result matches well with the calculation of Sagawa *et al.* [Sag98]; also when extrapolated to zero temperature, the result agrees quite well with the recent calculation of Satula *et al.* [Sat09] (section 3.2.2). However, at lower mass regions the measured isospin mixing values seem to be a bit higher at higher temperatures [Hab05]. It could also be mentioned here that in all the measurements which applied the formalism of Ref. [Beh93] to extract isospin mixing, heavy ion fusion reaction was used to ensure the statistical nature of the evaporated  $\gamma$  rays. However, in such reactions the compound nuclei are populated at higher angular momenta which in turn affect the high energy  $\gamma$

ray spectrum [Bra95], particularly at lower mass regions where different exotic nuclear shapes arise owing to large angular momentum [Maj04, Bre07, Dee10a]. It should also be pointed out that in all the previous measurements in lower mass regions, nuclear level density parameter, which is vital for statistical model calculations as well as for precise determination of nuclear temperature, was not measured.

Exclusive experiments were, therefore, performed to measure the isospin mixing in  $^{32}\text{S}$  for which only one measurement exists at 58.3 MeV [Hab04]. The primal objectives were to a) populate the compound nucleus with light-ion-induced fusion reaction to minimize the angular momentum effect, b) precisely measure the angular momentum populated by measuring the low energy  $\gamma$  ray multiplicity, c) measure the crucial NLD parameter, for the first time in this context, by measuring the evaporated neutron energy spectrum, d) determine the exact temperature by simultaneous measurement of angular momentum and NLD parameter, e) compare our result with the calculations of Ref. [Sag98] and attempt to extrapolate the result towards zero temperature.

# Chapter 4

## Statistical Model Calculations

When a target nucleus is bombarded with a low energy projectile, an excited compound nucleus (CN) is formed. This process conserves the total energy, angular momentum, parity and to some extent the isospin. At these excitation energies, the CN has a large number of available states and it equilibrates in shape, spin and thermal degrees of freedom before decaying into various exit channels. The statistical model calculation, therefore, is an appropriate as well as necessary tool to interpret the experimental data. The principal assumption of this model is that the decay of the CN is independent of its formation process i.e. the CN completely forgets the memory of the entrance channel. The cross section of the  $i$ -th exit channel, therefore, is given by

$$\sigma_i = \sigma_{\text{CN}} \frac{\Gamma_i}{\Gamma^\dagger} \quad (4.1)$$

where  $\sigma_{\text{CN}}$  is the compound nuclear formation cross section or fusion cross section,  $\Gamma_i$  is the width of the  $i$ -th exit channel and  $\Gamma^\dagger$  is the total decay width of the compound nuclear state. These quantities are calculated by using a modified version of the statistical model code CASCADE originally developed by F. Puhlhofer [Pul77] based on the standard Hauser-Feshbach formalism.

## 4.1 Compound nucleus formation

Let us consider a fixed target nucleus (spin, parity, mass  $J_T$ ,  $\pi_T$  and  $M_T$ , respectively) being bombarded by a projectile (spin, parity and mass  $J_P$ ,  $\pi_P$  and  $M_P$ , respectively) of energy  $E_{\text{beam}}$ . The compound nucleus is formed with a definite initial excitation energy given by  $E^* = Q + \{M_T/(M_T + M_P)\}E_{\text{beam}}$ ,  $Q$  being the Q-value of the reaction but with a broad range of angular momentum. The partial cross section  $\sigma(J, \pi)$  for the formation of a compound nucleus with spin  $J$  and parity  $\pi$  is given by

$$\sigma(J, \pi) = \frac{\lambda^2}{4\pi} \frac{(2J+1)}{(2J_P+1)(2J_T+1)} \sum_{S=|J_P-J_T|}^{S=J_P+J_T} \sum_{L=|J-S|}^{L=J+S} T_L(E_{\text{beam}}) \quad (4.2)$$

where  $\lambda = h/\sqrt{2\mu E_{\text{cm}}}$  is the wavelength of the projectile in centre of mass frame.  $\mu$  is reduced mass of the target and the projectile and  $E_{\text{cm}} = \{M_T/(M_P + M_T)\}E_{\text{beam}}$  is the available energy in the centre of mass frame.  $T_L(E_{\text{beam}})$  is the transmission coefficient at radial angular momentum  $L$  and energy  $E_{\text{beam}}$ . The sum over  $L$  is restricted by the parity conservation relation  $\pi = \pi_P \pi_T (-1)^L$ . In strong absorption model  $T_L$  is given by

$$T_L(E_{\text{beam}}) = \frac{1}{1 + \exp[\{L - L_0(E_{\text{beam}})\}/d]} \quad (4.3)$$

where  $d$  is the diffuseness parameter. The parameter  $L_0(E_{\text{beam}})$  is chosen so as to reproduce experimentally determined total fusion cross section  $\sigma_{\text{CN}}(E^*) = \sum_{J,\pi} \sigma(J, \pi)$ . It should be highlighted here that, due to experimental data acquisition conditions, a part of  $\sigma(J, \pi)$  was selected in the actual experiments performed in the present thesis. This was simulated with the actual experimental conditions (section 5.3.1) and was incorporated in the CASCADE code (instead of calculating it within the CASCADE code).

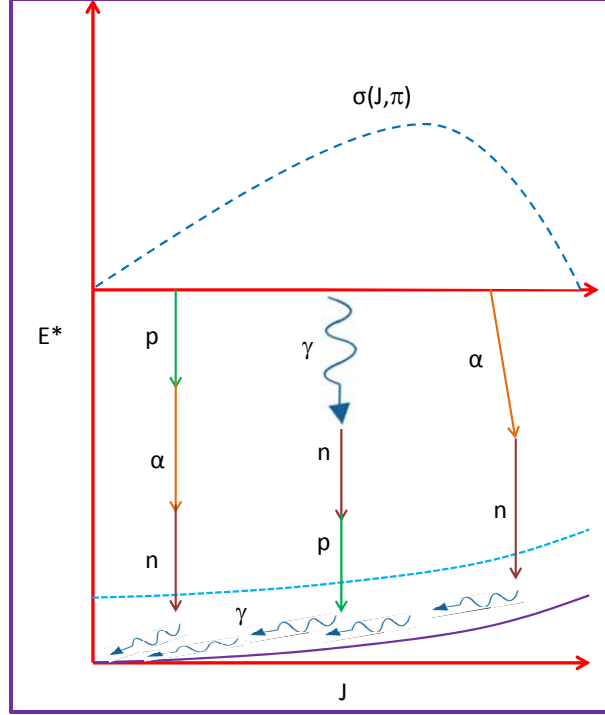


Figure 4.1: Schematic diagram for the decay of compound nucleus.

## 4.2 Compound nucleus decay

Once a compound nucleus is formed, it equilibrates in shape, thermal and spin degrees of freedom. This equilibrated nucleus then decays into different exit channels depending on the compound nuclear state. In this thesis, the decay of four particles namely neutron, proton, alpha and  $\gamma$  has been considered. Fig. (4.1) schematically shows the compound nuclear decay process. The decay width of any exit channel is determined, by the reciprocity theorem, from the absorption cross section in the inverse channel. The decay width of a particle  $x$  with energy  $E_x$  and spin  $S_x$  is given by

$$\left(\frac{d\Gamma_x}{dE_x}\right)_{J_i} = \frac{1}{2\pi} \frac{\rho_f(E_f, J_f)}{\rho_i(E_i, J_i)} \sum_{S=|J_f-S_x|}^{S=J_f+S_x} \sum_{L=|J_i-S|}^{L=J_i+S} T_L^x(E_x) \quad (4.4)$$

where  $\rho_f(E_f, J_f)$  and  $\rho_i(E_i, J_i)$  are the level densities of the daughter and the mother states with energy and spin  $E_f, J_f$  and  $E_i, J_i$ , respectively. The energy

of the emitted particle is related to  $E_i$  and  $E_f$  by  $E_x = E_i - E_f - B_x$ ,  $B_x$  being the separation energy of particle  $x$ .  $T_L^x$  is the transmission coefficient of  $x$  in the potential of the daughter nucleus. This is a crucial input in the CASCADE code and calculated by solving the Schroedinger equation with the optical model potential. In this thesis, the optical model parameters of Becchetti and Greenlees [Bec69] were used for neutron and proton, while for  $\alpha$ , the parameters of Mcfadden and Satchler [Mcf66] were utilized.

The  $\gamma$  decay width has been calculated using the reciprocity theorem and the Brink-Axel hypothesis [Bri55, Axe62] which states that the GDR can be built on each and every state of atomic nuclei. For  $E1$  (GDR)  $\gamma$  transition from an initial state  $E_i, J_i$  to a final state  $E_f, J_f$ , the decay width is given by

$$\left(\frac{d\Gamma_\gamma}{dE_\gamma}\right)_{J_i} = \sum_{J_f=J_i-1}^{J_f=J_i+1} \frac{\rho_f(E_f, J_f) \sigma_{\text{abs}}(E_\gamma)}{\rho_i(E_i, J_i)} \frac{E_\gamma^2}{3 (\pi \hbar c)^2} \quad (4.5)$$

where  $E_\gamma = E_i - E_f$  and  $\sigma_{\text{abs}}(E_\gamma)$  is the photo absorption cross section for a state at excitation energy  $E_f$  and spin  $J_f$ .  $\sigma_{\text{abs}}(E_\gamma)$  usually taken as a Lorentzian given by

$$\sigma_{\text{abs}}(E_\gamma) = \frac{4\pi e^2 \hbar NZ}{m_p c} \frac{S_{\text{GDR}} \Gamma_{\text{GDR}} E_\gamma^2}{A (E_\gamma^2 - E_{\text{GDR}}^2)^2 + \Gamma_{\text{GDR}}^2 E_\gamma^2} \quad (4.6)$$

where  $m_p$  is the proton mass,  $S_{\text{GDR}}$ ,  $\Gamma_{\text{GDR}}$ , and  $E_{\text{GDR}}$  are the strength, the width and the peak energy of the resonance, respectively. These are given as input for the compound nucleus in the CASCADE code. For other nuclei in the decay CASCADE,  $E_{\text{GDR}}$  is scaled by using the prescription of Berman and Fultz which gives  $E_{\text{GDR}} = 31.2/A^{1/3} + 20.6/A^{1/6}$  [Ber75].

The  $E2$  (Giant quadrupole resonance) emission is also included in the CASCADE code. However, the contribution of GQR is negligibly small in the region of interest.

### 4.3 Nuclear level density

The most crucial ingredient in the statistical model calculations is nuclear level density (NLD). The decay widths of different exit channels depend significantly on the NLD. Therefore, incorporation of proper NLD over a wide range of excitations is crucial for correct interpretation of experimental results. The fundamental method to calculate the NLD is to determine the number of different ways in which individual nucleons can be placed in various single particle orbitals such that the excitation energy lies in the range  $E^*$  and  $E^* + dE^*$ . Thus the physics, in the determination of NLD, is contained in calculation procedure of the single particle states.

The simplest possible single particle level distribution is that of equally spaced levels [Boh99]. However, from the neutron resonance data it is observed that

- (a) In the vicinity of the closed shells, the experimental level spacings are considerably larger than between shells.
- (b) There are odd-even fluctuations in the density of states if one uses the actual excitation energies i.e. the neutron binding energies as the reference energies.

To take into account these effects many authors have independently developed semiempirical prescriptions for the calculation of NLD [Ign75, Kat78, Rei81, Sch82]. The nuclear level density, at angular momentum  $J$  and both parity together, as a function of excitation energy is given by

$$\rho(E^*, J) = \frac{2J + 1}{12\Theta'^{3/2}} \sqrt{a} \frac{\exp(2\sqrt{aU})}{U^2} \quad (4.7)$$

where  $\Theta' = \Theta(1 + \delta_1 J^2 + \delta_2 J^4)$  is deformable liquid drop moment of inertia;  $\Theta = 2I_r/\hbar^2$ ,  $I_r = 2/5MR^2$  is the rigid body moment of inertia and  $\delta_1, \delta_2$  are the

deformability coefficients.  $U = E^* - \Delta P - J(J+1)/\Theta'^2$  is the intrinsic excitation energy,  $\Delta P$  being the pairing energy.  $a$  is the nuclear level density parameter which is proportional to the single particle density of states at the Fermi surface. According to the prescription of Ignatyuk and Reisdorf [Ign75, Rei81] the NLD parameter  $a$  is given by

$$\begin{aligned} a &= \tilde{a}(A)a_{\text{sh}} \\ a_{\text{sh}} &= 1 + \frac{\Delta S}{U} \{1 - \exp(-\gamma U)\} \end{aligned} \quad (4.8)$$

where  $\tilde{a}$  is the smooth or the liquid drop part and  $a_{\text{sh}}$  is the shell correction part of the NLD parameter.  $\gamma$  is the shell damping factor which determines the rate of shell effect depletion with excitation energy. The ground state shell correction  $\Delta S$  is calculated from the relation

$$\Delta P + \Delta S = M_{\text{exp}} - M_{\text{ld}} \quad (4.9)$$

$M_{\text{exp}}$  and  $M_{\text{ld}}$  being the experimental and liquid drop mass of nucleus. Ignatyuk *et al.* assumed  $\tilde{a} = \alpha + \beta A$  [Ign75] while Reisdorf calculated  $\tilde{a}$  from the density of eigenmodes in a deformed cavity with realistic boundary conditions [Rei81]. The calculations yield

$$\tilde{a} = a_v r_0^3 A + a_s r_0^2 A^{\frac{2}{3}} B_s + a_k r_0 A^{\frac{1}{3}} B_k \quad (4.10)$$

where  $a_v$ ,  $a_s$  and  $a_k$  are  $0.04543 \text{ MeV}^{-1}\text{fm}^{-3}$ ,  $0.1355 \text{ MeV}^{-1}\text{fm}^{-2}$  and  $0.1426 \text{ MeV}^{-1}\text{fm}^{-1}$ , respectively. Reisdorf assumed  $\Delta P = p/\sqrt{A}$ . From neutron resonance data for nuclei with  $A = 100\text{-}253$  the parameters  $r_0$ ,  $p$  and  $\gamma$  were found to be  $1.153 \text{ fm}$ ,  $10.5 \text{ MeV}$  and  $0.054 \text{ MeV}^{-1}$ , respectively.  $B_s$  and  $B_k$  are the surface and curvature terms in the liquid drop model. The parameter  $\tilde{a}$  is sometimes denoted by  $\tilde{a} = A/K$ , where  $K$  is called inverse level density parameter and is determined experimentally from evaporated neutron energy spectra [Kau12, Pra13, Pra16].

In this thesis,  $\tilde{a}$  is determined from the measured neutron energy spectra which are then utilized for the analysis of high energy  $\gamma$  ray spectra. Also, following Kicinska-Habior [Hab90], who tested this level density prescription for light masses,  $a_s$  and  $a_k$  were taken as  $0.1246 \text{ MeV}^{-1}\text{fm}^{-2}$  and  $0.1523 \text{ MeV}^{-1}\text{fm}^{-1}$ , respectively, which are slightly different from the original values obtained by Reisdorf from neutron resonance data in heavier masses. Also the values of  $B_s$  and  $B_k$  are assumed to be unity.

## 4.4 Isospin and parity in statistical model calculations

Isospin and parity quantum numbers were incorporated in the standard statistical model code *CASCADE* [Pul77] originally by Harakeh [Har86]; and later it was modified by Behr [Beh91, Beh93]. In this version of *CASCADE* code, apart from energy ( $E$ ) and angular momentum ( $J$ ), population cross section matrices and level densities were assigned with definite isospin ( $I$ ) and parity ( $\pi$ ) quantum numbers. Two lowest possible isospin states  $I_{<} \equiv |I, I = I_z\rangle$  and  $I_{>} \equiv |I + 1, I = I_z\rangle$  were considered in each nucleus. To calculate the decay widths Eqs. (4.4) and (4.5) were multiplied by proper Clebsch-Gordan Coefficients. Also the effect of isospin splitting and strength distribution (described in section 3.4) for  $E1$   $\gamma$  transitions were properly taken care of. As far as parity is concerned, it is not so important at high excitations as roughly both positive and negative parity states are populated equally. Also, it was assumed that the level densities are equally divided between both parity states. Consequently, the inclusion of parity does not affect the emission of GDR  $\gamma$  rays which are emitted from the initial steps of compound nuclear decay.

### 4.4.1 Isospin dependence of nuclear level density

Eq. (4.7) does not involve the isospin quantum number. It refers to the total level density at energy  $E^*$  and angular momentum  $J$ . The level density of a state  $|I, I = I_z\rangle$  in the parent nucleus is calculated by subtracting the level density of the isobaric analog nucleus from that of the parent nucleus. The NLD of the isobaric analog nucleus is calculated by using Eq. (4.7) with a proper shift in the excitation energy. For example, The level densities of  $|0, I = I_z = 0\rangle$  and  $|1, I = I_z = 0\rangle$  states in  $^{32}\text{S}$  are calculated as follows

$$\begin{aligned}\rho_{32\text{S}}(E^*, J, I = 0) &= \rho_{32\text{S}}(E^*, J) - \rho_{32\text{P}}(E^* - E_{\text{IAS}, I=1}, J) \\ \rho_{32\text{S}}(E^*, J, I = 1) &= \rho_{32\text{P}}(E^* - E_{\text{IAS}, I=1}, J) - \rho_{32\text{Si}}(E^* - E_{\text{IAS}, I=2}, J)\end{aligned}\quad (4.11)$$

where  $E_{\text{IAS}, I}$  is the energy of the isobaric analog state of isospin  $I$ . In the CASCADE code it is calculated as

$$\begin{aligned}E_{\text{IAS}} &= M(Z_{\text{IAS}}) - M(Z) + \Delta E_c - (m_n - m_p) \quad \text{for } N \geq Z \\ E_{\text{IAS}} &= M(Z_{\text{IAS}}) - M(Z) - \Delta E_c + (m_n - m_p) \quad \text{for } N < Z\end{aligned}\quad (4.12)$$

$Z_{\text{IAS}}$  is the proton number of the analog nucleus. For  $N \geq Z$ ,  $Z_{\text{IAS}} = Z - 1$ ,  $N_{\text{IAS}} = N + 1$  and for  $N < Z$ ,  $Z_{\text{IAS}} = Z + 1$ ,  $N_{\text{IAS}} = N - 1$ .  $\Delta E_c$  is the Coulomb displacement energy and is given by [Wil69] (in keV unit)

$$\begin{aligned}\Delta E_c &= 1539 \frac{\bar{Z}}{A^{1/3}} - 3230 \frac{\bar{Z}}{A} + 3600 \frac{\bar{Z}}{A^{4/3}} - 783 \left[ \frac{\bar{Z}}{A} \right]^{1/3} + 530 \left[ \frac{\bar{Z}}{A^2} \right]^{1/3} \\ &\quad - 17 \frac{\bar{Z}}{A^{2/3}} \left[ \bar{Z} - \frac{A}{3 + 0.022484 A^{2/3}} \right] + 60\end{aligned}\quad (4.13)$$

where  $\bar{Z} = Z_{<} + 0.5$ ,  $Z_{<}$  being the minimum of  $Z$  and  $Z_{\text{IAS}}$ . For  $^{32}\text{S}$ ,  $\Delta E_c = 5.9$  MeV,  $E_{\text{IAS}, I=1} = 6.8$  MeV,  $E_{\text{IAS}, I=2} = 11.8$  MeV and  $\rho(I = 1)/\rho(I = 0) \sim 1/3$  at initial excitation energy  $\sim 40$  MeV.

### 4.4.2 Isospin mixing in the statistical model calculations

In the version of the CASCADE code used in this thesis, population cross section was mixed before decay into different exit channels. The mixing was

formalized according to the prescription of Harney, Richter and Weidenmuller [Hrn86]. The authors considered isospin mixing in compound nuclear reaction by Coulomb force using the  $S$ -matrix formalism. As Coulomb force conserve angular momentum and parity, mixing between the states  $I_{<} = |I, I = I_z\rangle$  and  $I_{>} = |I + 1, I = I_z\rangle$  of same spin and parity was considered. The Coulomb spreading widths at a given energy and angular momentum are given by

$$\begin{aligned}\Gamma_{<}^{\downarrow} &= 2\pi |\langle I_{>} | V_c | I_{<} \rangle|^2 \rho(I_{>}) \\ \Gamma_{>}^{\downarrow} &= 2\pi |\langle I_{<} | V_c | I_{>} \rangle|^2 \rho(I_{<})\end{aligned}\tag{4.14}$$

As the matrix elements in Eq. (4.14) are roughly the same, it is obvious that

$$\frac{\Gamma_{<}^{\downarrow}}{\Gamma_{>}^{\downarrow}} = \frac{\rho(I_{>})}{\rho(I_{<})}\tag{4.15}$$

The fractions of  $\gtrsim$  states that goes to the  $\lesssim$  states by virtue of isospin mixing are given by

$$\alpha_{\gtrsim}^2 = \frac{\Gamma_{\gtrsim}^{\downarrow}/\Gamma_{\gtrsim}^{\uparrow}}{1 + \Gamma_{\gtrsim}^{\downarrow}/\Gamma_{\gtrsim}^{\uparrow} + \Gamma_{\lesssim}^{\downarrow}/\Gamma_{\lesssim}^{\uparrow}}\tag{4.16}$$

where  $\Gamma^{\uparrow}$  is the statistical decay width of the respective states. The mixed population cross sections are obtained from the cross sections of pure isospin states as follows

$$\begin{aligned}\tilde{\sigma}_{<} &= (1 - \alpha_{<}^2)\sigma_{<} + \alpha_{>}^2\sigma_{>} \\ \tilde{\sigma}_{>} &= (1 - \alpha_{>}^2)\sigma_{>} + \alpha_{<}^2\sigma_{<}\end{aligned}\tag{4.17}$$

where  $\sigma$  and  $\tilde{\sigma}$  are the pure and mixed population cross sections of the respective states.

For the nuclei considered in this thesis, only  $I_{<}$  states are populated in the initial compound nucleus if it is assumed that isospin is conserved. The calculations are started, therefore, using  $\sigma_{<} \neq 0$  and  $\sigma_{>} = 0$ . Only  $\Gamma_{>}^{\downarrow}$  is given as an input parameter and  $\Gamma_{<}^{\downarrow}$  is calculated by using Eq. (4.15). Once the decay

widths are calculated within the CASCADE code,  $\alpha_{\gtrsim}^2$  and  $\tilde{\sigma}_{\gtrsim}$  are calculated from Eqs. (4.16) and (4.17), respectively. The cross sections of the exit channels are then determined using these mixed population cross sections. These steps are followed at each and every step in the decay cascade.

# Chapter 5

## Experimental Details and Simulation Studies

This thesis deals with experimental determination of

- (a)  $\eta/s$  for finite nuclear matter at four different mass regions ( $^{31}\text{P}$ ,  $^{97}\text{Tc}$ ,  $^{119}\text{Sb}$ ,  $^{201}\text{Tl}$ ) [Deb17].
- (b) Isospin mixing at high temperature in  $^{32}\text{S}$  [Deb16].

In both the studies, the quantities that have been measured are the high-energy  $\gamma$  rays from the decay of IVGDR, evaporated neutron energy spectrum and angular momentum of the compound nucleus (CN). Therefore, the experimental set-up, detector systems, data acquisition electronics and data reduction techniques were the same in both the cases. The high-energy  $\gamma$  ray spectra were measured using a **Large Area Modular BaF<sub>2</sub> Detector Array** (LAMBDA) spectrometer [Sup07]. The CN angular momenta were determined by measuring the low-energy  $\gamma$  ray multiplicity with a Gamma Multiplicity filter [Dee10], while the evaporated neutron energy spectra were measured by using a Neutron Time of Flight (TOF) detector [Kau07, Kau09]. In this chapter the details of these detector systems and associated electronics, simulations studies, data reduction techniques are discussed.

## 5.1 High-energy $\gamma$ ray detectors

The cross section of high-energy  $\gamma$  rays from the decay of IVGDR is  $10^{-3}$ - $10^{-4}$  times smaller than the particle (neutron, proton etc.) decay cross sections. Therefore, the detector systems used for the measurement of high-energy  $\gamma$  rays should have large efficiency. The high-energy  $\gamma$  rays interact with the detector material by pair production mechanism ( $\gamma \rightarrow e^+ - e^-$ ) and produce electromagnetic (EM) shower. The cross section of this process is proportional to  $Z^2$ , where  $Z$  is the proton number of the detector material. The high-energy  $\gamma$  ray detectors, thus, should be made of high  $Z$  material and should be sufficiently large to contain the EM shower within its volume. Another important quality of these detectors is the high rejection capability of neutrons which are the major source of background in the measurement of high-energy  $\gamma$  rays. The neutrons are mainly removed by TOF technique. The  $\gamma$ -ray detectors, therefore, should have good time resolution so that the neutrons can be rejected even when the detector is placed close enough to the target thereby increasing its geometrical efficiency.

The inorganic scintillators fulfill most of the above requirements and thus are considered to be the best detector material for high-energy  $\gamma$  ray detection. The best suited and cost effective inorganic scintillator is  $\text{BaF}_2$  whose detection efficiency is high owing to large density ( $4.89 \text{ gm/cm}^3$ ). The scintillation light output of  $\text{BaF}_2$  material consists of two parts namely a fast component (decay time  $\sim 600 \text{ ps}$ ) peaking at  $\lambda \sim 220 \text{ nm}$  and a slow component (decay time  $\sim 630 \text{ ns}$ ) peaking at a larger wavelength  $\lambda \sim 320 \text{ nm}$ . The intensity ratio of the fast component to the slow component is of  $\sim 1:4$ . The fast component provides the time information, while the second component gives the energy information. Owing to the smaller decay time and high reproducibility of the fast component,

the time resolution of  $\text{BaF}_2$  scintillators is few hundred picoseconds. In addition, the radiation length and Molliere radius are 2.05 cm and 3.39 cm, respectively, resulting in smaller longitudinal and transverse spread and effective confinement of EM shower. However, the disadvantage of  $\text{BaF}_2$  is small scintillation efficiency ( $\sim 10000$  photons are produced per MeV of incident  $\gamma$  radiation) resulting in poor energy resolution. Also, the temperature dependence of light output leads to gain instability necessitating frequent calibration and maintenance of steady temperature during experiment. Apart from that, there is intrinsic  $\alpha$ -activity due to radium impurities, which are always present in  $\text{BaF}_2$  crystals.

Another inorganic scintillator material that is often used for high-energy  $\gamma$  ray measurement is  $\text{NaI(Tl)}$ . Due to large scintillation efficiency ( $\sim 40000$  photons are produced per MeV of incident  $\gamma$  radiation), its energy resolution is better than that of  $\text{BaF}_2$ . Also, its efficiency is comparable to that of  $\text{BaF}_2$ . However, the time resolution of  $\text{NaI(Tl)}$  is much worse than that of  $\text{BaF}_2$ . Apart from that,  $\text{NaI(Tl)}$  is hygroscopic and difficult to handle. Its thermal neutron capture cross section is also large making it inferior to  $\text{BaF}_2$ .

In recent years, another inorganic scintillator  $\text{LaBr}_3(\text{Ce})$  has gained much popularity in studying  $\gamma$ -ray spectroscopy. Due to large atomic number and high density ( $5.1 \text{ gm/cm}^3$ ) its detection efficiency is better than that of  $\text{BaF}_2$  and  $\text{NaI(Tl)}$ . Its energy resolution is also better ( $\sim 60000$  photons are produced per MeV of incident  $\gamma$  radiation) and time resolution is comparable to that of  $\text{BaF}_2$ . However, main disadvantage of this scintillator is that it is difficult to grow in large volume and is very costly. The material is very hygroscopic and non-linearity is observed at high energies.

At the Variable Energy Cyclotron Centre (VECC), Kolkata, two sophisti-

cated detector systems, namely, the LAMBDA spectrometer and the Multiplicity filter have been developed with BaF<sub>2</sub> scintillators. In the following sections these detector systems are described in detail.

## 5.2 The LAMBDA spectrometer

The LAMBDA spectrometer [Sup07] consists of 162 BaF<sub>2</sub> scintillator detectors each having a length of 35 cm and cross sectional area of 3.5×3.5 cm<sup>2</sup>. The prime advantages of the array are

- (a) large  $\gamma$ -ray detection efficiency and fast timing response.
- (b) high granularity which reduces  $\gamma - \gamma$  and  $\gamma - n$  pile-up events.
- (c) modularity i.e. the array can be arranged in different matrix configurations (5×5, 7×7, 9×9) depending on the experimental requirements.



Figure 5.1: Schematic diagram of the LAMBDA spectrometer arranged in three 7×7 matrix.

In this thesis, a part of the LAMBDA spectrometer arranged in a 7×7 matrix was utilized [Fig. 5.1].

### 5.2.1 Fabrication and properties of individual detectors

The detector elements were fabricated from bare BaF<sub>2</sub> crystals using standard procedure. The crystals were properly cleaned with dehydrated ethyl alcohol and wrapped with 8-10 layers of 10  $\mu\text{m}$  thick white teflon (C<sub>2</sub>H<sub>4</sub>) cloth which is a good UV reflector (since BaF<sub>2</sub> emits scintillation light in UV region). Teflon also acts like a diffused reflector which minimizes the non-uniformity of large detector elements. 3-4 layers of aluminium foil of thickness 10  $\mu\text{m}$  were used for efficient light collection and block the surrounding lights from entering into the detector. Fast UV sensitive photomultiplier tubes (29 mm diameter, Phillips XP2978) were coupled with the crystals with a highly viscous UV transmitting optical grease (Basyllone). The coupled systems were then wrapped with light tight black tape. Specially designed aluminium collars were used around the coupling area to provide additional support. The whole assembly was then covered with heat shrinkable PVC tube.

The non-uniformity of individual detector elements was checked with <sup>137</sup>Cs source and was found to less than 5%. The energy resolution ( $R = \Delta E/E$ ) of the detectors was studied with laboratory standard sources such as <sup>137</sup>Cs, <sup>22</sup>Na, <sup>241</sup>Am-<sup>9</sup>Be. It was observed that  $R \sim 16/\sqrt{E}(\%)$ , where  $E$  is in units of MeV. The time resolution between two BaF<sub>2</sub> detectors was measured with <sup>60</sup>Co source keeping the two detectors 180° apart. The energy gated (1.0-1.4 MeV) time resolution was found to be 960 ps [Sup07]. The  $\alpha$  impurities were determined using pulse shape discrimination technique and the measured value was 0.3 counts/sec/cm<sup>3</sup>.

### 5.2.2 Calibration of the LAMBDA spectrometer

Each detector element of the LAMBDA array was calibrated using the  $\gamma$  radiation from laboratory standard sources (<sup>22</sup>Na, <sup>241</sup>Am-<sup>9</sup>Be) and minimum ion-

izing cosmic muon backgrounds. The sources give the low energy part of the calibration curve, while the high-energy part is obtained from cosmic muon backgrounds. In Figs. (5.2a) and (5.2b) the measured  $\gamma$ -ray spectrum of  $^{22}\text{Na}$  (0.511, 1.274 MeV) and  $^{241}\text{Am}$ - $^9\text{Be}$  (4.43 MeV) are shown, respectively. Due to high granularity of the array the probability of full energy deposition in a single detector for 4.43 MeV  $\gamma$  rays is rather small and they leak into the neighboring detectors. Therefore, to get the full energy deposition in a single detector data was analyzed in no leak condition i.e. only those events were selected for which only one detector in the whole array fired at a time. The minimum ionizing cosmic muons deposit 6.6 MeV of energy per centimeter in  $\text{BaF}_2$  material. When

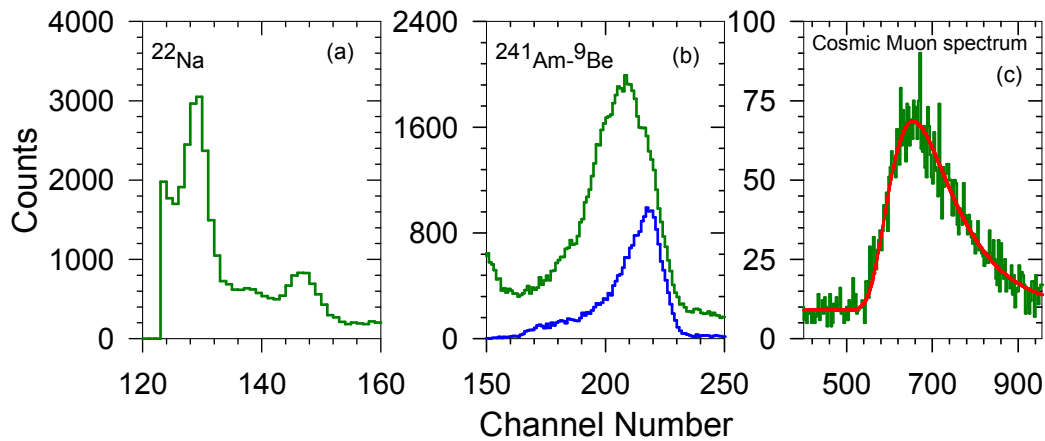


Figure 5.2: Energy spectrum of (a)  $^{22}\text{Na}$  (b)  $^{241}\text{Am}$ - $^9\text{Be}$  (c) minimum ionizing cosmic muon backgrounds. The green and blue solid lines in Fig. (b) are  $^{241}\text{Am}$ - $^9\text{Be}$  spectra with leak and no leak conditions, respectively. The red line in Fig. (c) represents the Landau fit to the experimental cosmic muon spectrum (green solid line).

a muon passes vertically through the array, it deposits 23.1 MeV of energy in each detector element (3.5 cm width) of the array. In offline analysis the cosmic spectrum in each detector element was generated when all detectors in a vertical column fired simultaneously. The typical form of muon spectrum is of Landau shape and the peak was obtained by fitting the experimental spectrum with the Landau function. Fig. (5.2c) shows a typical cosmic muon spectrum fitted

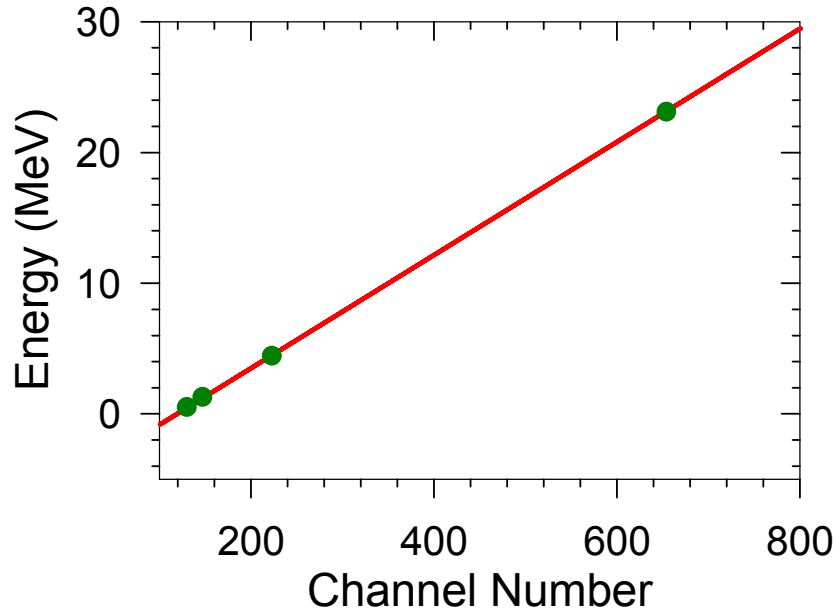


Figure 5.3: A typical energy calibration curve of a detector element of the LAMBDA spectrometer. The green solid circles are the experimental points and the red solid line is the best fitted straight line.

with the Landau function. In this process the whole array can be calibrated in a short time. A typical calibration curve is shown in Fig. (5.3). As can be seen that the detector remains linear at least up to 23.1 MeV energy. During the experiment, the gain of the array was frequently monitored and calibration was performed once in 30-36 hours.

### 5.2.3 Response of the LAMBDA spectrometer

The response function of a detector is crucial for proper interpretation of the experimental data, specially when one is dealing with  $\gamma$  rays. In the present thesis, the response of the LAMBDA spectrometer was simulated using Monte Carlo GEANT4 simulation package [Ago03] with nearly exact experimental geometry and conditions. The response was then folded with the statistical model (CASCADE) calculations to compare it with experimental data for extraction of

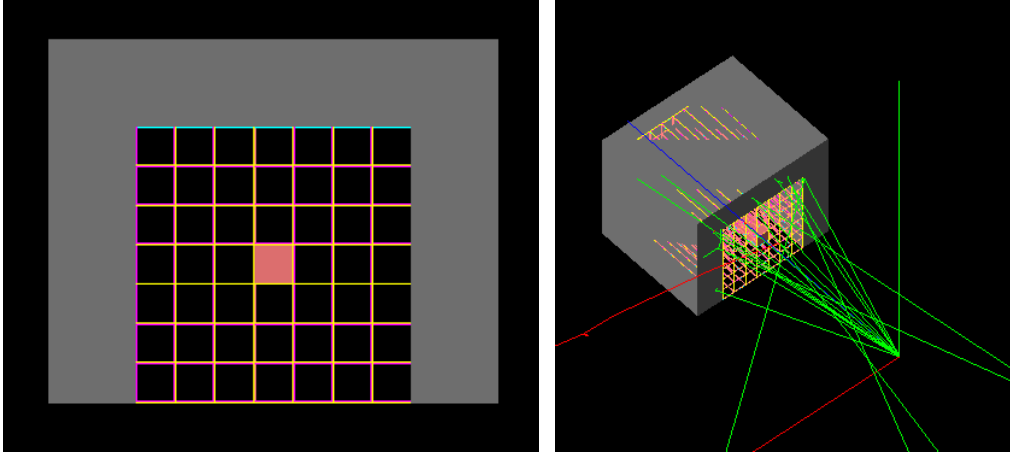


Figure 5.4: *Geometry of the LAMBDA array used in the experiments. The grey cover is the passive lead shield. The left panel is the cross sectional view and the right panel shows the three dimensional view.*

desired quantities. The array was placed at a distance of 50 cm from the target position. The geometry was constructed by properly taking into account the  $\text{BaF}_2$  and other wrapping materials, passive lead shield, target chamber etc. The  $\gamma$  rays of energies 0-40 MeV were thrown uniformly in 0.25 MeV interval from the target and tracked through the detector material with proper physics processes (pair production, photoelectric effect, Compton scattering, multiple scattering, ionization, bremsstrahlung etc.) through which the  $\gamma$  rays and other secondary particles (electron) interact with detector materials and deposit their energies. Owing to the high granularity of the array, the high-energy  $\gamma$  rays leak into different detectors. Various methods were tested for event reconstruction and the nearest neighbor cluster summing (section 5.6.4) was found to be the most efficient technique. The response functions of the LAMBDA spectrometer for different energies are shown in Fig. (5.5). It should be mentioned that response of the PM tubes was not considered in the present thesis. The response functions for different energies were saved in  $160 \times 160$  matrix and folded with the CASCADE spectrum (interpolated in 0.25 MeV bin as CASCADE gives spec-

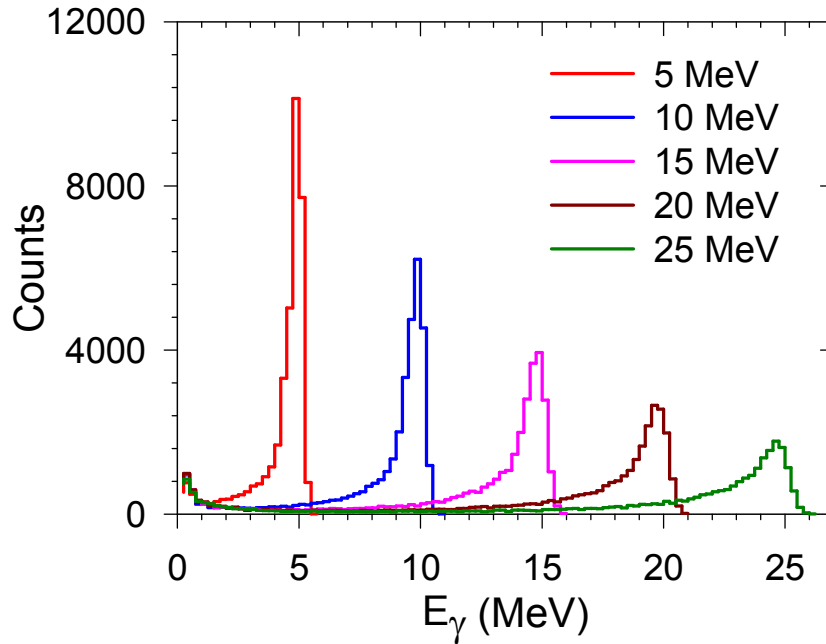


Figure 5.5: *Simulated response function of the LAMBDA spectrometer for different incident  $\gamma$ -ray energies.*

trum in 1.0 MeV bin) before comparing it with the experimentally measured spectra.

### 5.3 Multiplicity filter

In fusion reaction, the compound nucleus (CN) is populated at a well defined initial excitation energy but with a broad range of angular momentum [Fig. (4.1)]. At the initial stages of decay, evaporated particles and high-energy (GDR)  $\gamma$  rays mainly removes excitation energy and a little angular momentum. Below the particle threshold energy ( $\sim 8$  MeV above the yrast line), energy is removed by statistical  $E1$   $\gamma$  rays. When excitation energy comes down near the yrast line, the angular momentum is removed by stretched  $E2$   $\gamma$  rays [Fig. (4.1)]. Thus, one can have an idea about the populated CN angular momentum by measuring the  $\gamma$ -ray multiplicity. Experimentally the  $\gamma$ -ray multiplicity is de-

terminated by an array of detectors placed close to the target. However, because of the detector efficiency and solid angle coverage, one cannot measure the exact number of emitted  $\gamma$  rays. What one measures is the number of detector fired (fold) in each event. From this fold distribution, one can find the multiplicity distribution and angular momentum distribution.

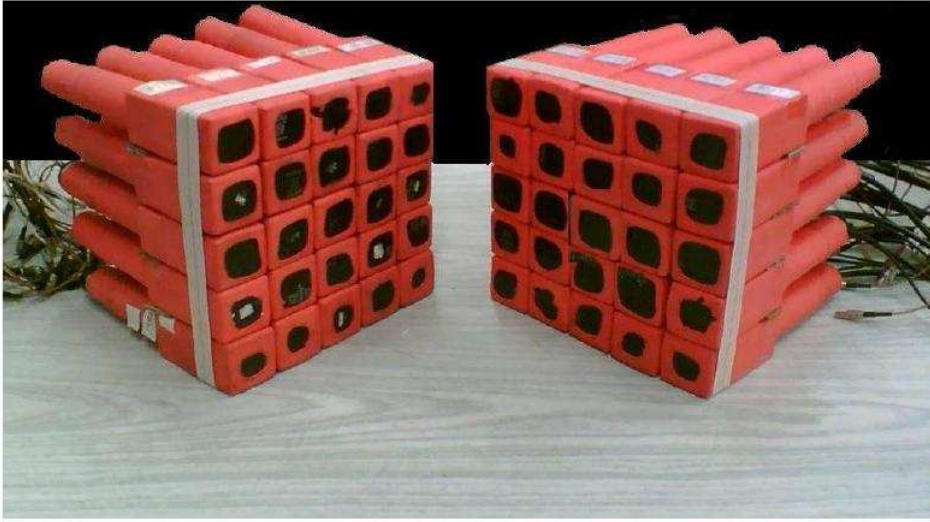


Figure 5.6: 50 element multiplicity filter divided in two blocks with 25 elements each and arranged in  $5 \times 5$  matrix.

At VECC, Kolkata, a 50 element multiplicity filter has been designed and developed with  $\text{BaF}_2$  scintillator [Dee10]. Fig. (5.6) shows the multiplicity filter divided into two blocks of 25 detectors each. During the experiment, the blocks are placed on the top and the bottom of the target chamber. Each detector is 5 cm long and has a cross sectional area of  $3.5 \times 3.5 \text{ cm}^2$ . The fabrication procedure was the same as that used for LAMBDA spectrometer (section 5.2.1). The energy resolution of the detector is  $\sim 7\%$  at 1.17 MeV and the energy gated (1.0-1.4 MeV) time resolution, studied with a  $^{60}\text{Co}$  source, between two multiplicity detector elements is  $\sim 450$  ps. The cross talk probability of the filter was checked with different laboratory standard sources at different thresholds.

For example, the cross talk probability is  $\sim 5\%$  for 662 keV  $\gamma$  rays at a threshold of 300 keV.

### 5.3.1 Mapping of fold distribution into angular momentum space

The angular momentum distributions were obtained by matching the experimentally measured fold distributions with the simulated ones [Fig. (5.8a)] obtained utilizing a realistic technique [Dee10]. The experimental fold distributions were obtained, in offline analysis, by gating with high-energy  $\gamma$  ray spectra ( $> 10$  MeV) so as to get rid of the non-fusion events. The simulations were performed using the Monte Carlo GEANT4 simulation package (Originally the simulations were done using Monte Carlo GEANT3 code [Bru86] and later it was upgraded to GEANT4). Two blocks of the multiplicity filter were placed on the top and the bottom of the target chamber at a distance of 5 cm from the target. Each block was arranged in a staggered castle type geometry to equalize

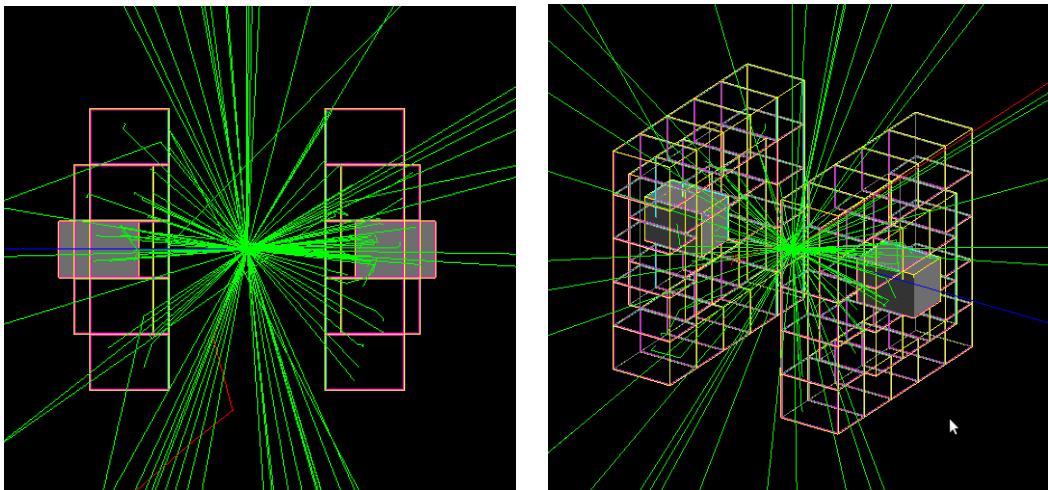


Figure 5.7: *Geometry of the multiplicity filter used in the experiments. The left panel is the cross sectional view and the right panel shows the three dimensional view.*

the solid angle of each detector element. In each event, the  $\gamma$ -ray multiplicity

was randomly generated according to the following distribution

$$P(M) = \frac{2M + 1}{1 + \exp\{(M - M_0)/\delta m\}} \quad (5.1)$$

where  $M_0$  is the maximum of the distribution and  $\delta m$  is diffuseness. The energy distribution of the multiplicity  $\gamma$  rays was assumed to be Gaussian with adjustable peak and width. The  $\gamma$  rays were tracked through the BaF<sub>2</sub> material with relevant physics processes and appropriate experimental conditions (trigger, threshold etc.). The parameters  $M_0$ ,  $\delta m$ , peak and width of the energy distribution were varied judiciously to match the experimental and simulated fold distributions. The conversion of multiplicity distribution into the angular momentum space was achieved using the relation  $J = 2M + C$ , where the free parameter  $C$  takes into account the angular momentum loss due to particle

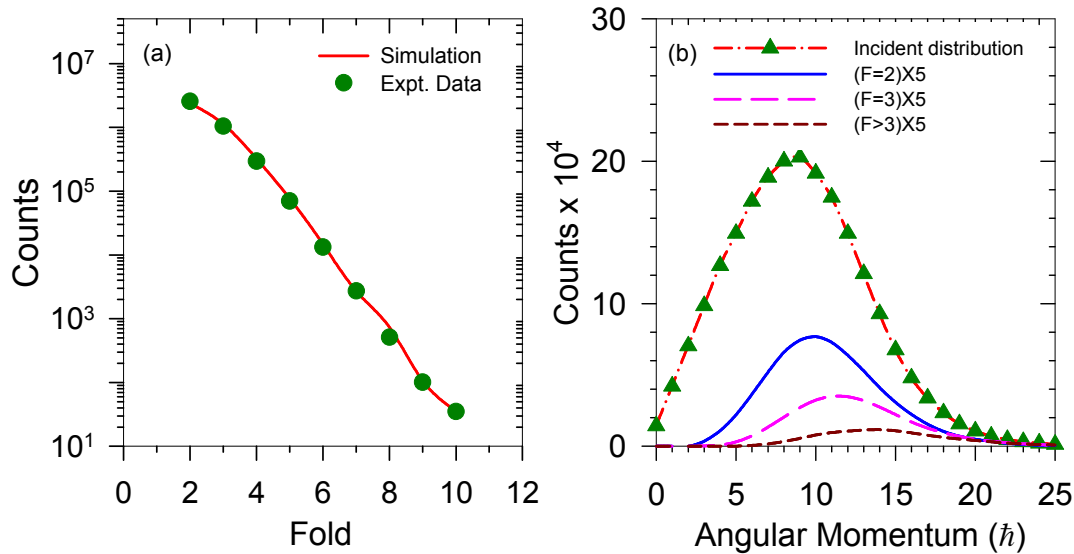


Figure 5.8: (a) Experimental (green symbols) and simulated (red line) fold distributions for  $^{31}\text{P}$  populated at initial excitation energy of 46.2 MeV. The simulated parameters are  $M_0 = 5$ ,  $\delta m = 1$ ,  $C = 1$ . Peak energy and width of the energy distribution are 0.65 MeV and 1.2 MeV, respectively. (b) Incident and different fold gated angular momentum distributions.

evaporation and statistical  $\gamma$  ray emission.  $C$  was obtained by matching the simulated CN angular momentum distribution with the calculated one by PACE4

code. After fixing all the parameters, different fold gated angular momentum distributions were generated according to the experimental requirements [Fig. (5.8b)].

## 5.4 Neutron time of flight detector

In the present work, the evaporated neutron energy spectra were measured to extract the nuclear level density parameter which is crucial for determining nuclear temperature and thus the entropy density for finite nuclear matter. The evaporated neutrons were detected with a liquid scintillator based time of flight (TOF) detector which is a part of the larger TOF array developed at VECC for spectroscopic study of energetic neutrons emitted in heavy ion induced reactions. A part of the array is shown in Fig. (5.9). Liquid scintillators



Figure 5.9: *Liquid organic scintillator (BC501A) based neutron TOF array.*

are widely used for neutron measurements in a mixed environment of neutrons and  $\gamma$  rays due to high light output, good detection efficiency, fast decay time and excellent n- $\gamma$  discrimination. Each detector cell was cylindrical in shape (5 inch in diameter and 5 inch in length) and was made up of 3 mm thick stainless

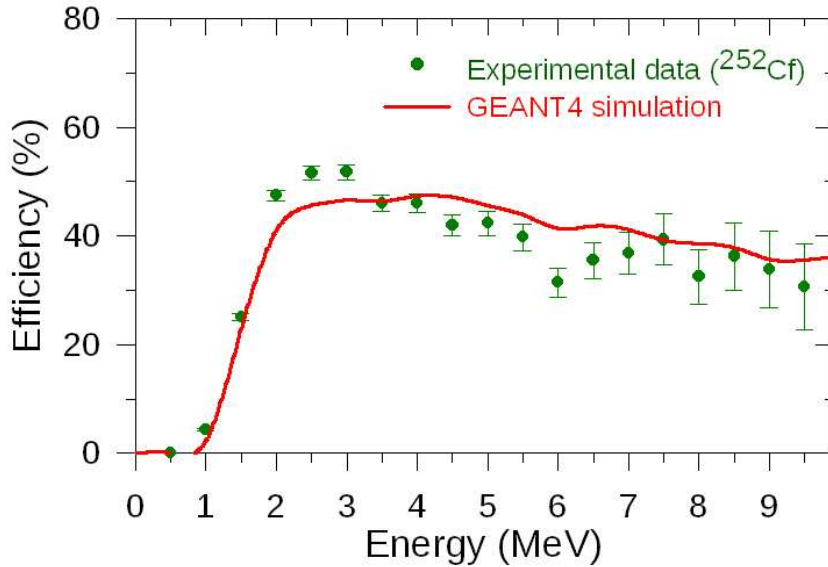


Figure 5.10: *Experimental (symbols) and simulated (solid line) neutron detection efficiency of BC501A based neutron TOF detector (adopted from [Bal15]).*

steel. The internal wall of the cells was white painted for efficient collection of scintillation light. The cells were filled with xylene-based liquid scintillator BC501A which was thoroughly flushed with dry nitrogen gas of purity 99.999% to remove the dissolved oxygen present in the liquid. The scintillator cells were sealed with 6 mm thick pyrex glass and were coupled with a 5 inch diameter PMT (model: 9823B, Electron tube Ltd.). The typical time resolution of a detector element is of  $\sim 1.2$  ns which results in an energy resolution of  $\sim 17\%$  at 1 MeV when placed at a distance of 150 cm from the target position. The intrinsic detector efficiency was measured with  $^{252}\text{Cf}$  source and is shown in Fig. (5.10) along with the GEANT4 simulations.

## 5.5 Experimental details

The experimental techniques were the same for both the studies reported in this thesis. That is why, an overall picture of the experimental procedures are

given in this section. The experiments were performed at the Variable Energy Cyclotron Centre, Kolkata using pulsed  $\alpha$ -beam from K-130, AVF cyclotron. Self-supporting targets were bombarded with  $\alpha$ -beam and different particles in the exit channel were detected using in-house developed dedicated detector systems described in the previous sections. The data were recorded and stored in event-by-event format by using an in-house developed VME based data acquisition system.

### 5.5.1 Detector set-up

The experimental set-up comprised of four major detector systems as shown in Fig. (5.11). The purpose and characteristics of each detector system have been described earlier. The LAMBDA array was configured in a  $7 \times 7$  matrix form and was placed at a distance of 50 cm from the target position at an angle of  $90^\circ$  with respect to the beam direction. It was surrounded by 8-10 cm thick lead bricks to block the cosmic  $\gamma$  ray backgrounds. It was observed by simulation that this arrangement could eliminate 90% of  $\gamma$  backgrounds. Also a 3 mm thick lead plate was placed in front of the array to cut down the low energy  $\gamma$  rays from the target. The geometrical efficiency of the array was 1.8 %. The 50 element multiplicity filter was divided into two blocks of 25 detectors each. The blocks were configured in  $5 \times 5$  matrices in staggered castle type geometry and were placed on the top and the bottom of the target chamber at a distance of 5 cm from the target. The angular coverage of the multiplicity filter was  $\sim 55$  %. All the detectors of the LAMBDA array and the multiplicity filter were gain matched so as to apply nearly equal threshold in all the detectors. A neutron time of flight detector was placed at a distance of 150 cm from the target and at an angle of  $150^\circ$  with respect to the beam direction. Two detector elements of the VENUS array [Sou16] were positioned at angles  $35^\circ$  and  $90^\circ$

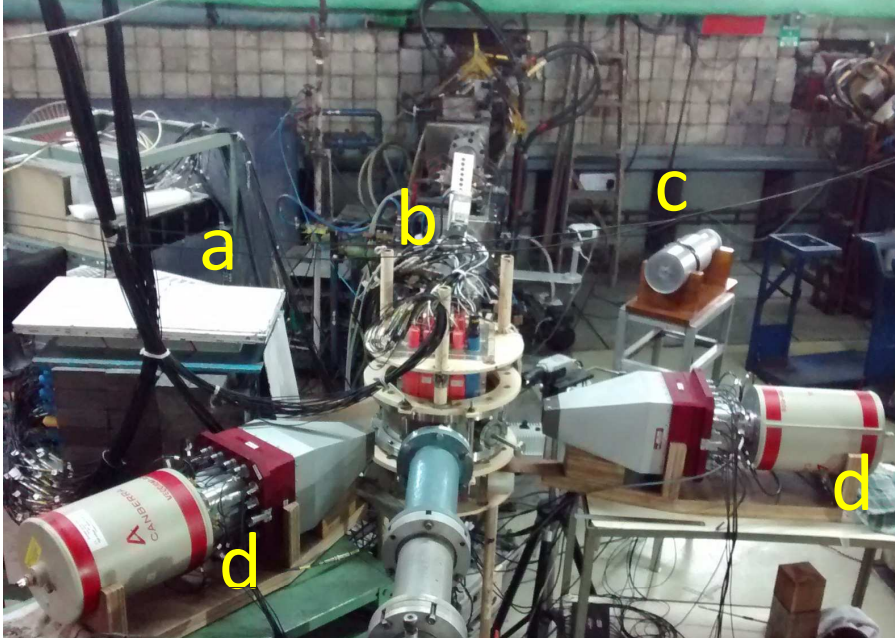


Figure 5.11: *Experimental set-up used in this thesis. (a) LAMBDA spectrometer, (b) Multiplicity filter, (c) Neutron TOF detector and (d) Clover detector.*

at a distance  $\sim 30$  cm from the target. These detectors were used for testing purpose and also to observe any presence of isotopic impurity in the target. The beam dump, located at  $\sim 3$  m downstream, was covered with borated paraffin blocks and lead bricks to cut the  $\gamma$  and neutron backgrounds. As the gain of  $\text{BaF}_2$  scintillators vary with temperature, arrangements were made to keep the temperature fixed at  $18^\circ\text{C}$ . The maximum variation of temperature was found to be  $\pm 1^\circ\text{C}$ . Nevertheless, the LAMBDA array was frequently calibrated to take care of the variation of temperature.

### 5.5.2 Electronics set-up for $\gamma$ ray measurements

The pulse processing and the data acquisition were performed with a dedicated CAMAC based front-end electronics and VME based data acquisition system developed at VECC. All ancillary equipments were placed inside the experi-

mental hall and controlled from outside over ethernet. Fig. (5.12) shows the complete electronics and data acquisition circuit diagram for the LAMBDA spectrometer and the multiplicity filter. In each event, three main quantities were recorded, namely, energy deposited in each detector element of the LAMBDA spectrometer, its time (with respect to the multiplicity filter start trigger) and the number of multiplicity detectors fired (fold). Apart from that, the cyclotron radio frequency (RF) time was also recorded with respect to the

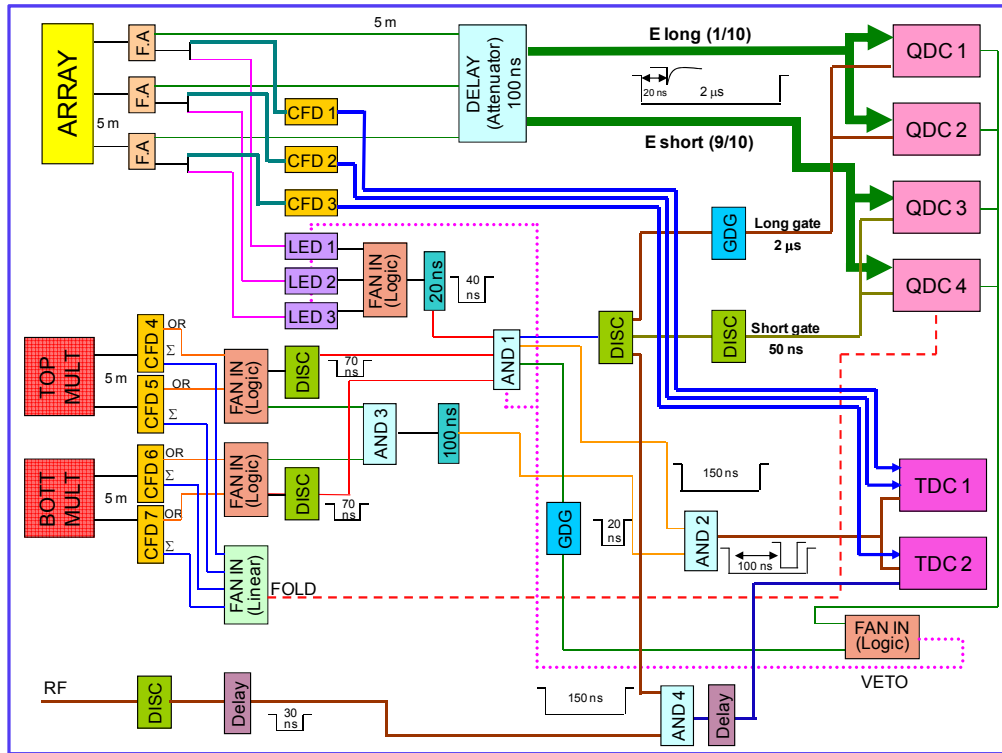


Figure 5.12: Circuit diagram used for detection of high-energy  $\gamma$  rays.

multiplicity filter. The signals from the LAMBDA array was divided into linear (for energy information) and logic paths. The signals in the logic path were fed into constant-fraction-discriminators (CFD) (CAEN C808) (for time information) and leading-edge-discriminators (LED) (CAEN C894) (for gate generation). The multiplicity detector signals were sent to CFDs and the re-

sulting logic signals were used for master trigger generation. A level-1 trigger was generated when any detector in the LAMBDA spectrometer fired above a threshold of  $\sim 4$  MeV. A level-2 trigger was generated when any of the detectors from the top multiplicity filter fired in coincidence with any of detectors from the bottom multiplicity above a threshold of  $\sim 300$  keV. A coincidence of level-1 and level-2 triggers generated the master trigger for the data acquisition. This coincidence technique guarantees the selection of statistical events as well as a significant reduction in background events. The time start was taken from the coincidence signal of both the top and the bottom multiplicity filters validated by the master trigger. The signals of the LAMBDA array in the linear path were divided into parts with amplitude ratio 1:9 and were fed into QDCs (CAEN V792), with a delay of 100 ns, through impedance adapters (CAEN A992). This was done for pulse shape discrimination (PSD) and the two linear signals were integrated for  $2 \mu\text{s}$  (long gate) and 50 ns (short gate), respectively. The integration times were so chosen that the PSD spectra formed a band along  $45^\circ$ . The logic signals from the CFDs were delayed properly and fed into TDCs (CAEN V775) which were run in common start mode. The fold of the multiplicity filter was obtained from the CFDs which give 1 mA output current per detector fired. Total current sum in each event was acquired using a linear fan-in module and was integrated in the short gate. The RF signal was validated by the master trigger and after adjusting with proper delay the signal was fed into a TDC. The signals from the clover detectors were properly shaped and sent to an ADC (CAEN V785). It should be mentioned that, in each run, the data were acquired in the clover detector in its own gate for 30-45 minutes and for rest of the time the acquisition was done with the gate generated by the master trigger.



The PH and the ZCT informations were recorded with an ADC (CAEN V785), while TOF and fold informations were acquired by a TDC (CAEN V775) and a QDC (CAEN V792), respectively. The prompt  $\gamma$  rays were separated from neutron by TOF technique. However, there are always  $\gamma$  backgrounds present even within the seemingly neutron events in TOF spectra. These  $\gamma$  backgrounds were separated from the neutrons by PSD technique comprising of PH and ZCT.

## 5.6 Data reduction for high-energy $\gamma$ rays

The GDR energy of the systems studied in this thesis, especially  $^{31}\text{P}$  and  $^{32}\text{S}$ , is of  $\sim 17\text{-}18$  MeV. As the cross section of  $\gamma$  rays falls exponentially with the increase in  $\gamma$  ray energy, it is very small at GDR energies and often comparable or less than that of the cosmic backgrounds. Apart from that, the statistical neutrons are the main source of background for  $\gamma$  ray measurements. Also, the pile-up events add to undesired contribution in the high-energy  $\gamma$  ray spectra. Special cares have been taken to eliminate all these backgrounds during the experiments (section 5.5.1) and in the offline analysis performed in the framework of CERN Physics Analysis Workstation (PAW). To ensure the selection of beam related events, the cyclotron RF time spectrum was measured [Fig. (5.14b)]. In offline analysis only those events were considered that were within the prompt gate (red shaded region in Fig. (5.14b)) of the RF time spectrum. In the following sections, the procedure of different background elimination and data reconstruction have been described in detail.

### 5.6.1 Rejection of neutron background

The energy of the neutron produced in the statistical decay of the compound nucleus lies mainly below 12 MeV. These neutrons interact with the  $\text{BaF}_2$  material via capture ( $n, \gamma$ ) and inelastic scattering ( $n, n'\gamma$ ) reactions i.e. ultimately the

neutron energy is deposited in the detector in the form  $\gamma$  rays. Thus, neutrons cannot be separated from  $\gamma$  rays using PSD technique. The only mechanism to

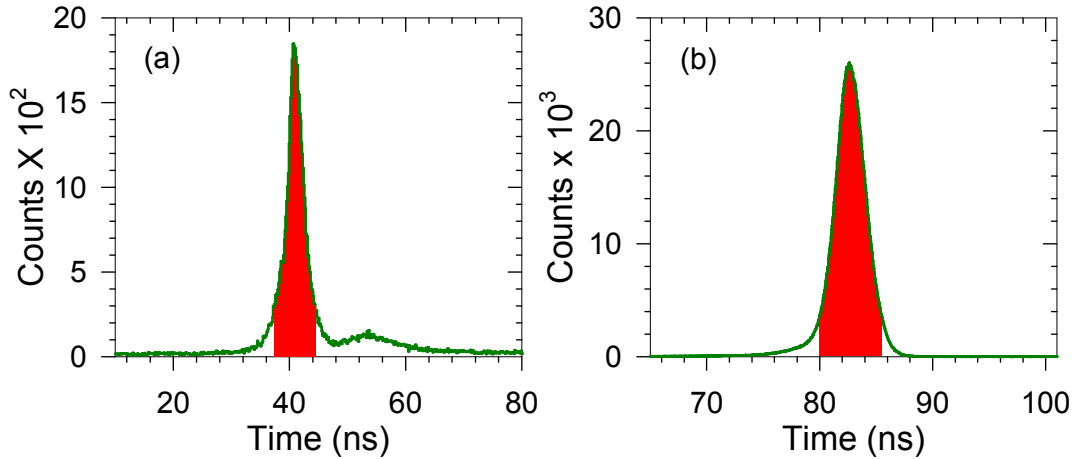


Figure 5.14: (a) A typical time of flight spectrum of a detector element of the LAMBDA array. (b) A typical cyclotron RF time spectrum. Both spectra were measured with respect to the multiplicity filter.

separate these neutron from  $\gamma$  rays is the time of flight technique. A typical time of flight spectrum of a detector element of the LAMBDA array is shown in Fig. (5.14a). The fast timing property of the  $\text{BaF}_2$  scintillators effectively separates the neutrons from photon events. In offline analysis, only those events were selected that fell within the prompt gate (red shaded region in Fig. (5.14a)) of the TOF spectra of individual detectors.

### 5.6.2 Rejection of pile-up events

A pile-up event occurs when, along with a valid high-energy  $\gamma$  ray in a single detector, another photon ( $\gamma, \gamma$  pile-up) or neutron ( $\gamma, n$  pile-up) enters the same detector within the same integration gate. In such cases, the ratio of the integrated charge in the long and the short gate will be different from that of a real photon event and thus will appear away from the true  $\gamma$  band in short vs long 2-dimensional spectrum of the individual detectors. A typical PSD spectrum

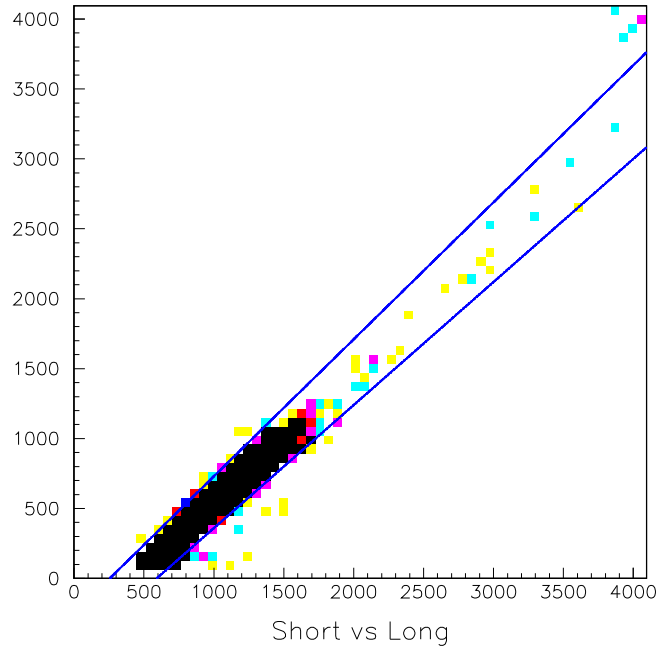


Figure 5.15: A typical short vs long 2d-dimensional spectrum of a detector element of the LAMBDA array. Only those events are considered to be valid events that lie in between the two straight lines.

for an element of the LAMBDA spectrometer is shown in Fig 5.15 along with the 2-dimensional cut used in offline analysis. It should be mentioned that, due to high granularity of the LAMBDA array, the contribution of pile-up events is negligibly small.

### 5.6.3 Rejection of cosmic backgrounds

As mentioned earlier, the major sources of backgrounds in the measurement of high-energy  $\gamma$  rays are the cosmic  $\gamma$  and muon ( $\mu$ ) backgrounds. The cosmic  $\gamma$  rays are blocked by the thick passive lead shield. However, the muons cannot be stopped by the lead shield. The high segmentation of the LAMBDA array and the hit pattern of cosmic muons were utilized to get rid of the muon backgrounds. As the energy of these muons are very high ( $\sim$  GeV), they pass through the whole array and deposits energy in the detector elements. Typical

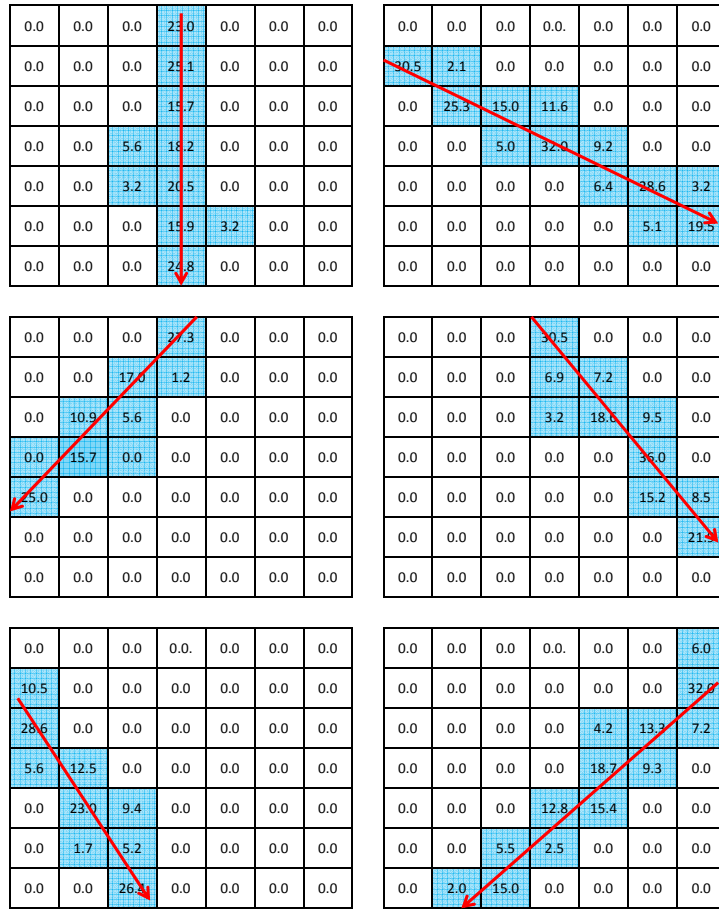
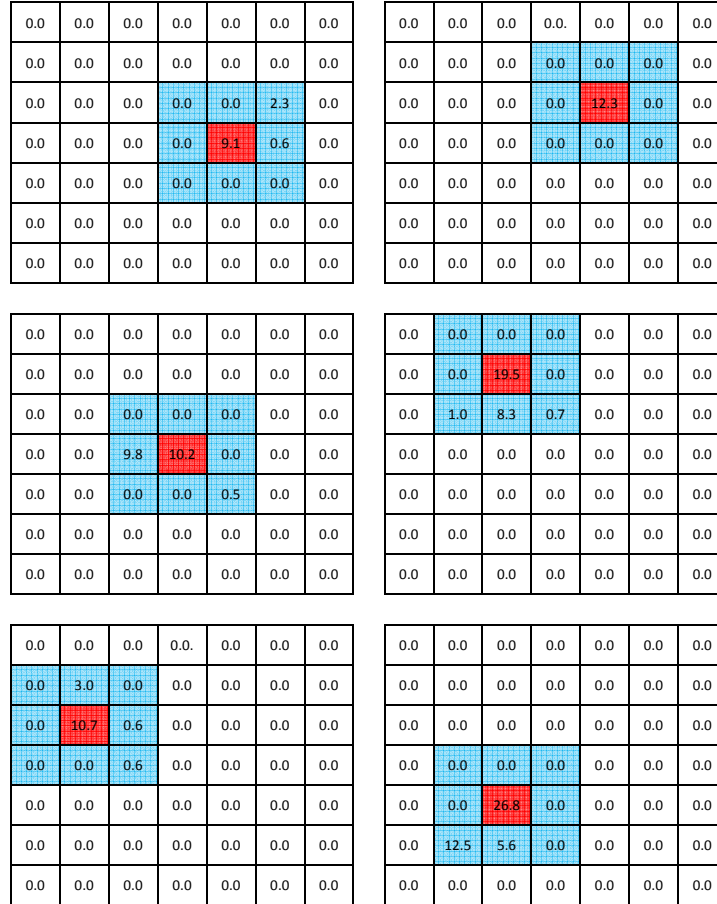


Figure 5.16: Typical cosmic muon hit patterns in the LAMBDA spectrometer.

tracks of the muons in the arrays are shown in Fig. (5.16). These patterns are quite different from those of true  $\gamma$  events [Fig. (5.17)] Therefore, in any event, if the detectors in top-bottom, top-left, top-right, bottom-left, bottom-right and left-right fired in coincidence, that event was rejected in offline analysis. Also, the cosmic muons deposit 6.6 MeV energy per centimeter of the  $\text{BaF}_2$  material. If the muons pass vertically, they deposit 23.1 MeV of energy in each detector element. For oblique incidents, the energy deposits are even higher. When the summing is done (section 5.6.4), the resulting energy lies much above the region of interest and thus rejected.

## 5.6.4 Data reconstruction

Figure 5.17: Typical hit patterns of true  $\gamma$  events in the LAMBDA spectrometer.

The energy of the  $\gamma$  rays was reconstructed using nearest neighbor cluster ( $3 \times 3$ ) summing technique. The detector with the highest energy deposition was considered as the centre of the cluster. If the centre of the cluster was found to be any of the side detectors then that event was rejected because, in that case, energy might leak out of the array. Apart from that, it was also checked whether the number of detectors fired in the cluster were the same as that fired in the whole array. Thus finding a valid cluster, the energy was reconstructed by summing the energy deposition in all nine detectors in the cluster. It should be mentioned that each detector element had to satisfy the various gates (prompt

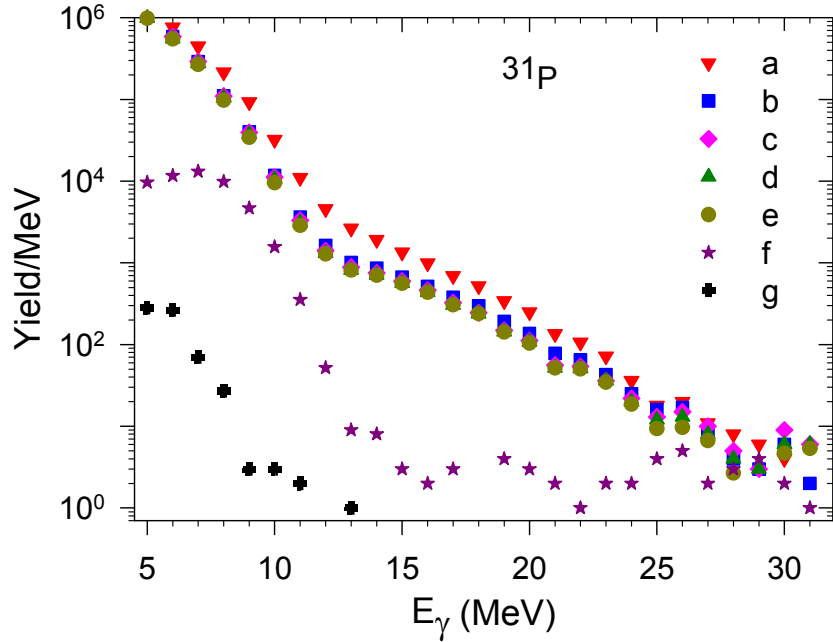


Figure 5.18: Typical high-energy  $\gamma$  ray spectra for different gate conditions. (a) Raw but time validated, (b) prompt time gated, (c) prompt time and PSD gated, (d) prompt time, PSD and prompt RF time gated, (e) same as d with RF and time background subtracted, (f) time background spectrum, (g) RF time background spectrum.

time gate, prompt RF time gate, PSD gate) described in previous sections. The sensitivities of different gates in high-energy  $\gamma$  ray spectra are shown in Fig. (5.18). Finally, the cluster summed  $\gamma$  energy was Doppler corrected by using the relation  $E_{corr} = \gamma'(1 - \beta \cos\theta)E_{clus}$ , where  $E_{clus}$  is the cluster summed energy.  $\beta$  is the velocity of the compound nucleus in units of velocity of light in free space and  $\gamma' = 1/\sqrt{1 - \beta^2}$ .  $\theta$  is the angle of the centre of the cluster with respect to the direction of the compound nuclear velocity (equivalent to the beam direction) which was in between  $45^\circ$ - $135^\circ$ . The maximum value of  $\beta$  was 0.0194 for  $^{31}\text{P}$  compound nucleus at 42 MeV beam energy. It resulted in maximum Doppler correction of 230 keV at  $E_{clus} = 17$  MeV, which remains within the energy bins (1 MeV). The background contributions arising due the chance coincidence in the prompt TOF gate and prompt RF gate have also been

subtracted to obtain the final high-energy  $\gamma$  ray spectra.

## 5.7 Data reduction for neutrons

As mentioned in section 5.5.3, the TOF and the ZCT were recorded in each event during the neutron measurements. As the pulse shapes for neutron and  $\gamma$  radiations are different, they are well separated in the two dimensional plot of ZCT vs TOF [Fig. (5.19)]. In the off-line analysis, only those events were selected that were within the two dimensional cut as shown in Fig. (5.19). These are neutron events which are then converted to neutron energy spectrum from

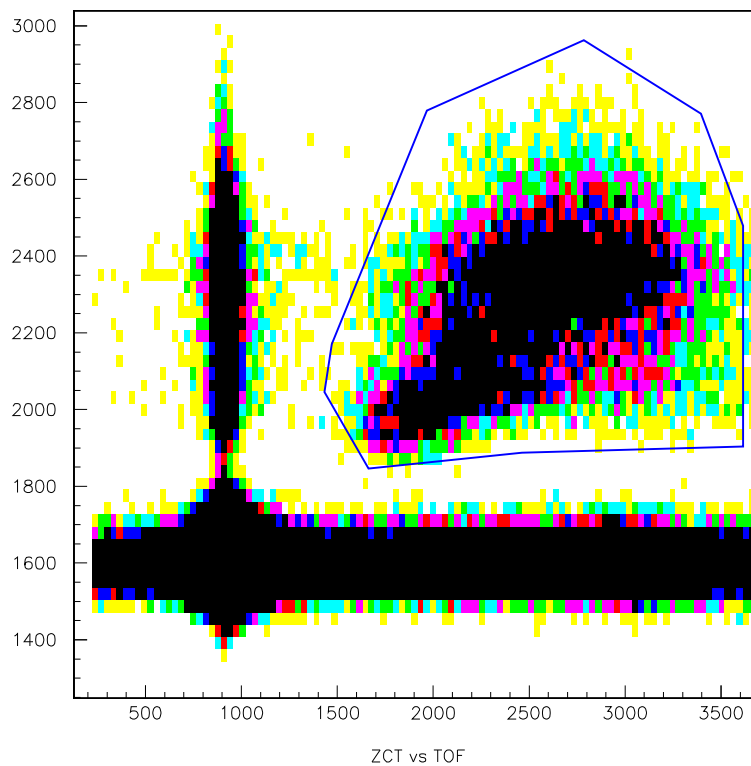


Figure 5.19: A typical two dimensional plot of ZCT vs TOF. The events that remain within the two dimensional cut are neutron events which are used for further analysis.

TOF spectrum using prompt  $\gamma$  peak as time reference. The effects of applying only the gate in TOF spectrum and both in TOF and ZCT spectra are shown

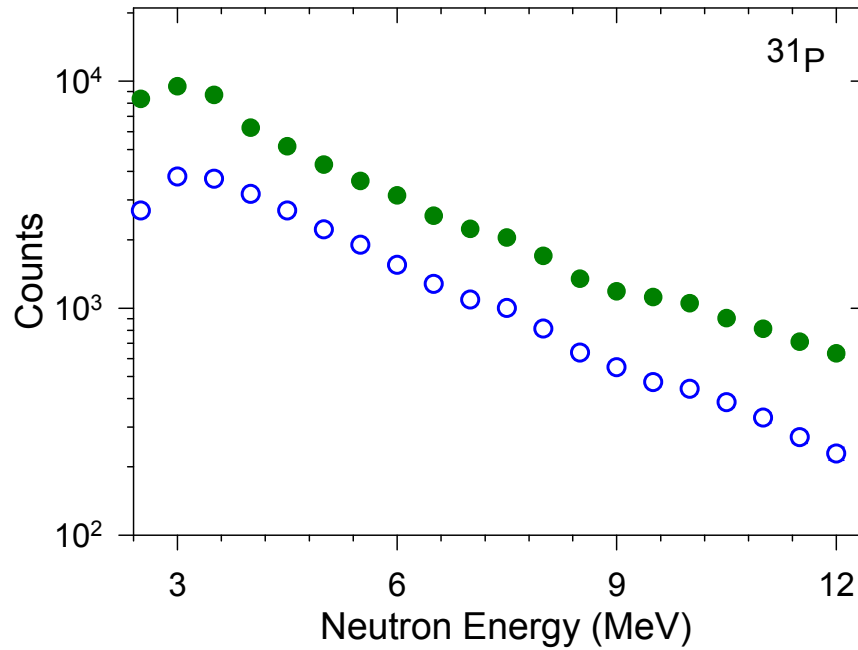


Figure 5.20: Typical evaporated neutron energy spectra of  $^{31}\text{P}$  with only neutron gate in TOF spectrum (green solid circles) and with the two dimensional cut (i.e. both TOF and ZCT gate) as shown in Fig. (5.19) (blue open circles).

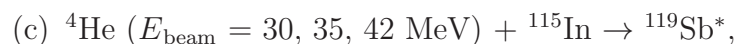
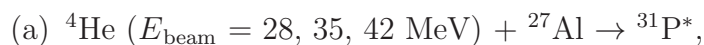
in Fig. (5.20). The neutron energy spectra were converted to the centre of mass frame from the laboratory frame and then compared with the statistical model calculations, after folding with the detector efficiency, to extract the nuclear level density parameter.



# Chapter 6

## $\eta/s$ for Finite Nuclear Matter: Experiments, Results, and Discussions

In this chapter, the work on the experimental determination of the ratio of shear viscosity ( $\eta$ ) to entropy density ( $s$ ) is presented. This is the first experimental study of  $\eta/s$  for finite nuclear matter [Deb17]. The nuclei  $^{31}\text{P}$ ,  $^{97}\text{Tc}$ ,  $^{119}\text{Sb}$ , and  $^{201}\text{Tl}$  were populated through following light-ion-induced compound nuclear reactions in the temperature range of (0.8-2.1) MeV using  $\alpha$  beams from the K-130 cyclotron at the Variable Energy Cyclotron Centre (VECC), Kolkata, India.



The importance of light ion lies in the fact that the compound nuclei were populated at angular momenta ( $J$ ), much less than the critical angular momenta for

the systems ( $J_c = 0.6A^{5/6}$ ) [Kus98] above which the effect of angular momentum on the GDR parameters is observed; hence exclusive temperature variation of the GDR parameters and consequently, the shear viscosity could be probed. However, there is a disadvantage of utilizing the light ion beam to populate the compound nuclei. The incident energy per nucleon above the Coulomb barrier for light ion is comparatively large, resulting in a non-statistical bremsstrahlung component. This has to be properly taken care of during the analysis of the experimental data. It should be mentioned that the experimental procedure and the results for the GDR parameters of  $^{97}\text{Tc}$ ,  $^{119}\text{Sb}$ , and  $^{201}\text{Tl}$  have been described in detail in Refs. [Sup12a, Dee12, Bal14]. In this chapter, experimental details will be described only for  $^{31}\text{P}$ . Finally, the results and discussions will be presented for all systems.

## 6.1 Experimental details and data reduction

In this set of experiments, the following quantities were determined

- (a) The GDR parameters (the peak energy, the width, and the strength) : determined by measuring the high-energy  $\gamma$  ray spectra from the decay of the GDR.
- (b) The nuclear level density (NLD) parameter: determined by measuring the evaporated neutron energy spectra.
- (c) The compound nuclear angular momentum: determined by measuring the low-energy  $\gamma$  ray multiplicity.
- (d) The bremsstrahlung slope parameter: determined by measuring the angular distributions of high-energy  $\gamma$  rays.

In this section, the experimental procedure and data reduction techniques, which have already been described in detail in chapter 5, are briefly presented.

The high-energy  $\gamma$  rays from the decay of the GDR were measured by a part of the LAMBDA spectrometer (section 5.2) placed at a distance of 50 cm from the target position and at an angle of  $90^\circ$  with respect to the beam direction. The 50-element multiplicity filter (section 5.3) was divided into two blocks of 25 elements each and was placed on the top and the bottom of the target chamber [Fig. (5.11)] to measure the  $\gamma$  ray multiplicity in an event-by-event mode. The evaporated neutron energy spectra were measured by using an element of the neutron TOF array (section 5.4) placed at a distance of 150 cm from the target position and at an angle of  $150^\circ$  with respect to the beam direction. The cyclotron RF time spectrum was recorded with respect to the multiplicity filter to ensure the selection of beam-related events. The angular distributions of high-energy  $\gamma$  spectra were also measured at  $55^\circ$  and  $125^\circ$  for  $^{31}\text{P}$  and  $^{119}\text{Sb}$  at  $E_{\text{beam}} = 42$  MeV.

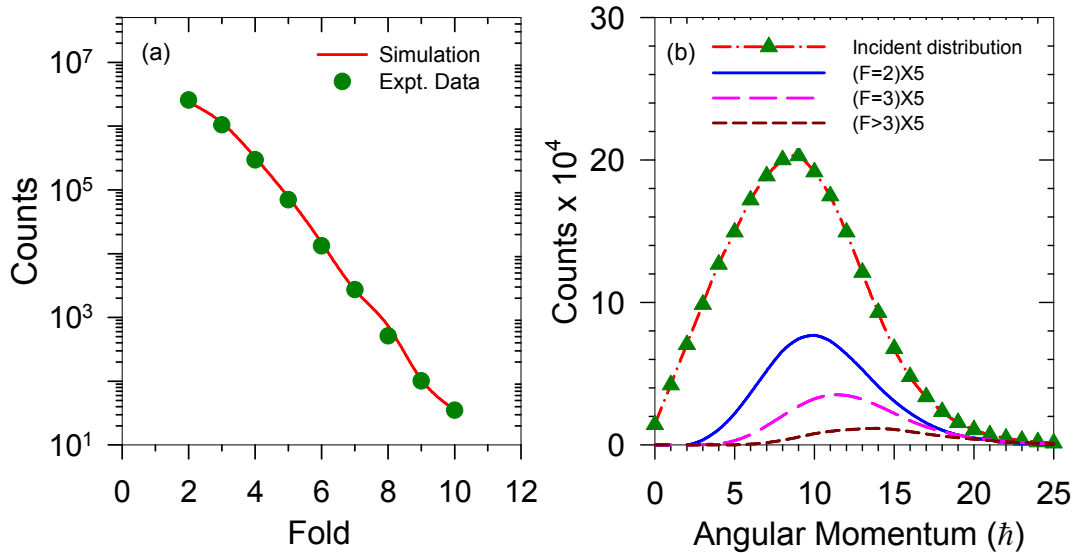


Figure 6.1: (a) Experimental (green symbols) and simulated (red line) fold distributions for  $^{31}\text{P}$  populated at initial excitation energy of 46.2 MeV. The simulated parameters are  $M_0 = 5$ ,  $\delta m = 1$ ,  $C = 1$ . Peak energy and width of the energy distribution are 0.65 MeV and 1.2 MeV, respectively (section 5.3.1). (b) Incident and different fold gated angular momentum distributions.

The high-energy  $\gamma$  rays detected in the LAMBDA spectrometer were reconstructed using the cluster summing technique after correcting for all the backgrounds as described in section 5.6. Different fold-gated (fold  $\equiv$  number of multiplicity detectors fired in each event) high-energy  $\gamma$  ray spectra were also reconstructed according to the requirements. The measured fold distributions were mapped onto the angular momentum space by a realistic technique based on GEANT4 simulations (section 5.3.1). Different fold-gated angular momentum distributions were simulated and average angular momenta corresponding to different folds were calculated using the relation  $\sum_J \sigma(J)J / \sum_J \sigma(J)$ . In Fig. (6.1) the measured and simulated fold distributions along with different fold-gated angular momentum distributions are shown for  $^{31}\text{P}$  populated at the initial excitation energy of 46.2 MeV. The neutron TOF spectra were converted to neutron energy spectra using the prompt  $\gamma$  peak as time reference (section 5.7) and different fold-gated neutron energy spectra were extracted. The neutron spectra were then converted from the laboratory frame to the centre of mass (c.m.) frame.

## 6.2 Extraction of NLD and GDR parameters

The nuclear level density and the GDR parameters were extracted by comparing the evaporated neutron energy spectra and the high-energy  $\gamma$  ray spectra, respectively, with the statistical model calculations performed using a modified version of the statistical model code CASCADE. It should be mentioned that as all nuclei considered in this chapter are non-self-conjugate nuclei, the isospin quantum number does not play a crucial role in statistical model calculations. That is why experimental data were analyzed using a version of the CASCADE code which does not involve isospin quantum number. The angular momentum distributions corresponding to different folds were incorporated in the CASCADE

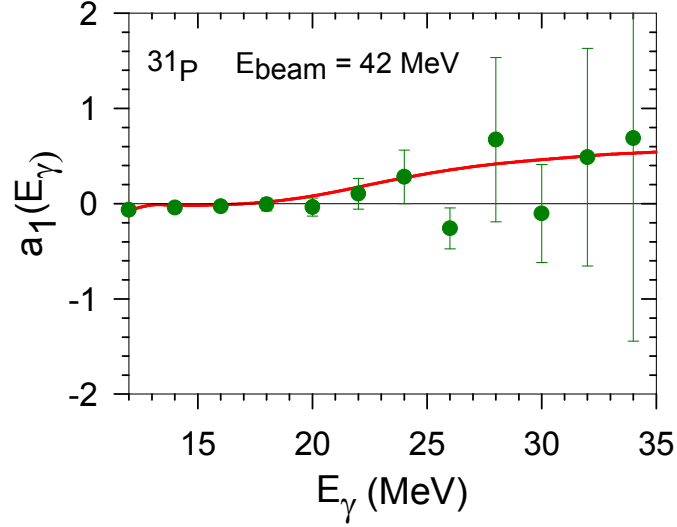


Figure 6.2: Variation of  $a_1(E_\gamma)$  with the  $\gamma$  ray energy. The green solid circles are experimentally determined, while the red solid line is theoretically calculated for  $E_0 = 5.3$  MeV and  $v_{nn} = 0.6 v_{beam}$ .

code and respective fold-gated neutron and high-energy  $\gamma$  ray spectra were compared with the calculations. The Ignatyuk-Reisdorf prescriptions (section 4.3) was utilized in the CASCADE calculations. The asymptotic nuclear level density parameter ( $\tilde{a}$ ) was varied, to match the experimental and calculated neutron energy spectra, by varying the  $r_0$  parameter (Eq. 4.10) and best fit value was obtained by  $\chi^2$  minimization procedure in the energy range 4-10 MeV. It should be mentioned that the calculated neutron spectra were folded with the energy dependent efficiency of the neutron TOF detector before comparing with the experimental spectra. Simultaneously, the calculated high-energy  $\gamma$  spectra, along with a bremsstrahlung component, parameterized as  $\sigma = \sigma_0 \exp(-E_\gamma/E_0)$ , were folded with the detector response function (section 5.2.3) and compared with the experimental spectra to extract the GDR parameters [resonance strength ( $S_{\text{GDR}}$ ), energy ( $E_{\text{GDR}}$ ) and width ( $\Gamma_{\text{GDR}}$ )].

The bremsstrahlung slope parameter  $E_0$  was determined from the angular

distribution of the high-energy  $\gamma$  rays measured at  $E_{beam} = 42$  MeV. The  $\gamma$ -ray angular distribution in the c.m. frame was assumed to have the form

$$W(E_\gamma, \theta) = W_0(E_\gamma)[1 + a_1(E_\gamma)P_1(\cos \theta) + a_2(E_\gamma)P_2(\cos \theta)] \quad (6.1)$$

Since  $P_2(\cos \theta) = 0$  for  $\theta = 55^\circ$  and  $125^\circ$ ,  $a_1(E_\gamma)$  was determined by measuring the  $\gamma$  ray yield (properly normalized with total incident beam particles) at  $\theta =$

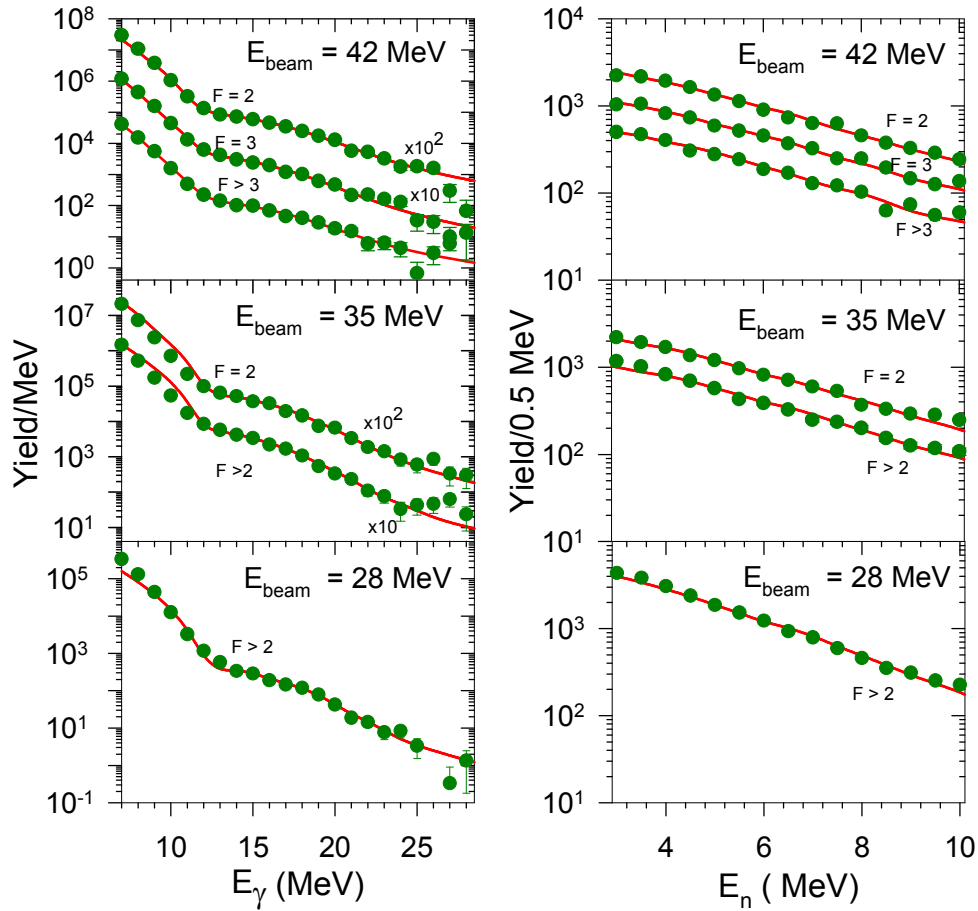


Figure 6.3: Different fold-gated high-energy  $\gamma$  ray spectra (left panel) and the evaporated neutron energy spectra (right panel) for  $^{31}\text{P}$ . The green solid symbols are experimentally measured spectra, while the red solid lines are the respective statistical model calculations.

$55^\circ$  and  $125^\circ$ . The bremsstrahlung slope parameter  $E_0$  was deduced by comparing the experimentally determined  $a_1(E_\gamma)$  with the theoretically calculated one [Fig. (6.2)]. The source of the bremsstrahlung component was assumed

Table 6.1: *Experimental GDR and asymptotic NLD parameters at the the specified angular momentum and temperature*

$E_{\text{beam}}$ MeV	$\langle J \rangle$ $\hbar$	$T$ MeV	$\tilde{a}$ MeV $^{-1}$	$E_{\text{GDR}}$ MeV	$\Gamma_{\text{GDR}}$ MeV
28	12.2±4.2	0.84±0.37	4.7±0.2	18.7±0.2	7.4±0.7
35	11.0±3.6	1.80±0.23	4.2±0.2	17.1±0.2	8.2±0.7
	13.4±4.3	1.55±0.30	4.2±0.2	16.8±0.2	7.7±0.7
42	11.8±3.7	2.06±0.18	4.3±0.2	17.5±0.2	9.3±0.4
	13.5±4.1	2.00±0.22	4.0±0.2	17.0±0.2	8.9±0.7
	15.9±5.2	1.69±0.33	4.0±0.2	17.8±0.2	8.5±0.6

to be due to collisions among the nucleons and the angular distribution of the radiation was assumed to be isotropic in the nucleon-nucleon (n-n) frame of reference. The bremsstrahlung energy spectrum was then converted from n-n frame to c.m. frame resulting in an angular distribution. Calculating these yield at  $\theta = 55^\circ$  and  $125^\circ$ , the value of  $a_1(E_\gamma)$  was extracted.  $a_1(E_\gamma)$  depends on the slope parameter  $E_0$ ; thus  $E_0$  was deduced by matching the calculated  $a_1(E_\gamma)$  with that obtained from experiments. The extracted slope parameter was found to be of  $\sim 5.3$  MeV, which could roughly be reproduced by the systematics  $E_0 = 1.1[(E_{\text{beam}} - V_c)/A_p]^{0.72}$  [Nif90]. This systematics was utilized to extract the slope parameters at the beam energies for which angular distribution of the high-energy  $\gamma$  ray was not measured. It should be mentioned that  $a_1(E_\gamma)$  also depends on the velocity ( $v_{\text{nn}}$ ) of the n-n frame with respect to the laboratory frame. Ideally  $v_{\text{nn}}$  should be  $0.5v_{\text{beam}}$ . However, in the present case,  $v_{\text{nn}}$  was found to be  $0.6v_{\text{beam}}$ . This slight difference could be attributed to the Fermi velocity of the nucleons.

In Fig. (6.3) different fold-gated high-energy  $\gamma$  ray spectra and the evaporated neutron energy spectra for  $^{31}\text{P}$  are presented along with the statistical model calculations. Resulting GDR and NLD parameters are shown in table (6.1)

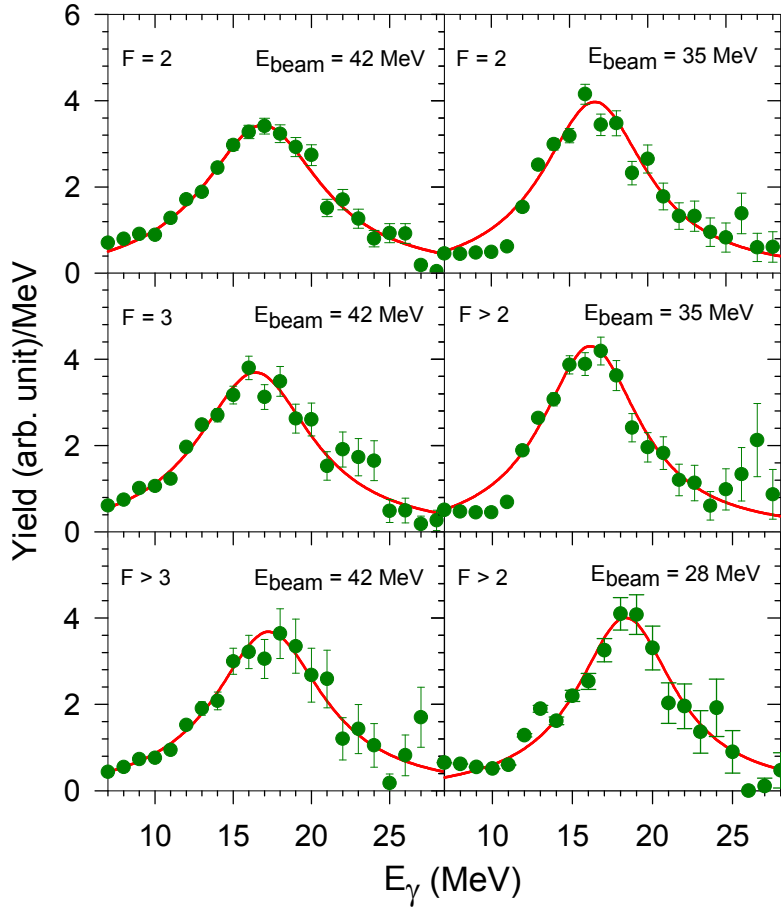


Figure 6.4: Different fold-gated linearized  $\gamma$  ray spectra for  $^{31}\text{P}$ . The green solid symbols are experimentally measured spectra, while the red solid lines are the respective Lorentzian having the GDR parameters as shown in table 6.1.

In order to emphasize on the GDR region the corresponding linearized spectra are shown in Fig. (6.4), using the quantity  $F(E_\gamma)Y^{exp}(E_\gamma)/Y^{cal}(E_\gamma)$ , where  $Y^{exp}(E_\gamma)$  and  $Y^{cal}(E_\gamma)$  are the experimental and the CASCADE spectra, while  $F(E_\gamma)$  is the Lorentzian having the GDR parameters as shown in table (6.1). The temperature was calculated using the relation  $T = \sqrt{U/a(T)}$ , where  $U = E^* - E_{\text{rot}} - E_{\text{GDR}} - \Delta P$ ;  $E^*$ ,  $E_{\text{rot}}$ ,  $E_{\text{GDR}}$ , and  $\Delta P$  being the initial excitation energy, average rotational energy, measured GDR energy, and the pairing energy, respectively.  $a(T)$  is the NLD parameter at temperature  $T$  corresponding to intrinsic excitation energy  $U$ . It should be mentioned that, GDR may have

contributions from the decay steps subsequent to the particle decay. Therefore, one should use an average initial excitation energy instead of  $E^*$ . For  $^{31}\text{P}$ , the GDR energy being high, contributions from the stages after particle decay were very small and the effect of averaging on  $T$  was negligible. For other nuclei, the average temperatures were found to remain well within the quoted errors which originate from the uncertainty in measured angular momentum, GDR energy and the NLD parameter. The details of the GDR parameters for  $^{97}\text{Tc}$ ,  $^{119}\text{Sb}$ , and  $^{201}\text{Tl}$  could be found in Refs. [Bal14, Sup12a, Dee12].

### 6.3 Determination of the shear viscosity

The shear viscosity ( $\eta$ ) was determined at different temperatures from the measured  $E_{\text{GDR}}$  and  $\Gamma_{\text{GDR}}$  by utilizing the formalism of Dang (section 2.4.1) according to which

$$\eta(T) = \eta(0) \frac{\Gamma_{\text{GDR}}(T)}{\Gamma_{\text{GDR}}(0)} \left\{ \frac{E_{\text{GDR}}(0)^2}{E_{\text{GDR}}(0)^2 - [\Gamma_{\text{GDR}}(0)/2]^2 + [\Gamma_{\text{GDR}}(T)/2]^2} \right\}^2, \quad (6.2)$$

where  $\eta(0)$  is the shear viscosity at zero temperature,  $E_{\text{GDR}}(0)$  and  $\Gamma_{\text{GDR}}(0)$  are the energy and the width of the GDR built on the ground state and  $\Gamma_{\text{GDR}}(T)$  is the width of the GDR built on the excited state at temperature  $T$ . As the energy of the GDR built on excited states is nearly independent of temperature (table 6.1), the ground state GDR energy  $E_{\text{GDR}}(0)$  was taken as the average ( $E_{\text{AV}}$ ) of the measured energies at different temperatures, while the accepted  $\Gamma_{\text{GDR}}(0)$  for  $^{31}\text{P}$ ,  $^{97}\text{Tc}$ ,  $^{119}\text{Sb}$  and  $^{201}\text{Tl}$  were 7.5, 5.5, 4.5, 3.5 MeV, respectively. As can be seen from Fig. (6.5) these ground state GDR widths nicely reproduce the variation of the measured GDR widths at higher temperatures within the CTFM calculations [Dee12]. Following Refs. [Aue75, Aue09, Dan11],  $\eta(0)$  was taken as  $1u$ , where  $u = 10^{-23} \text{ MeV}\cdot\text{s}\cdot\text{fm}^{-3}$ . Interestingly, the ground state GDR widths and average GDR energies (except for  $^{31}\text{P}$ ) were well reproduced by the

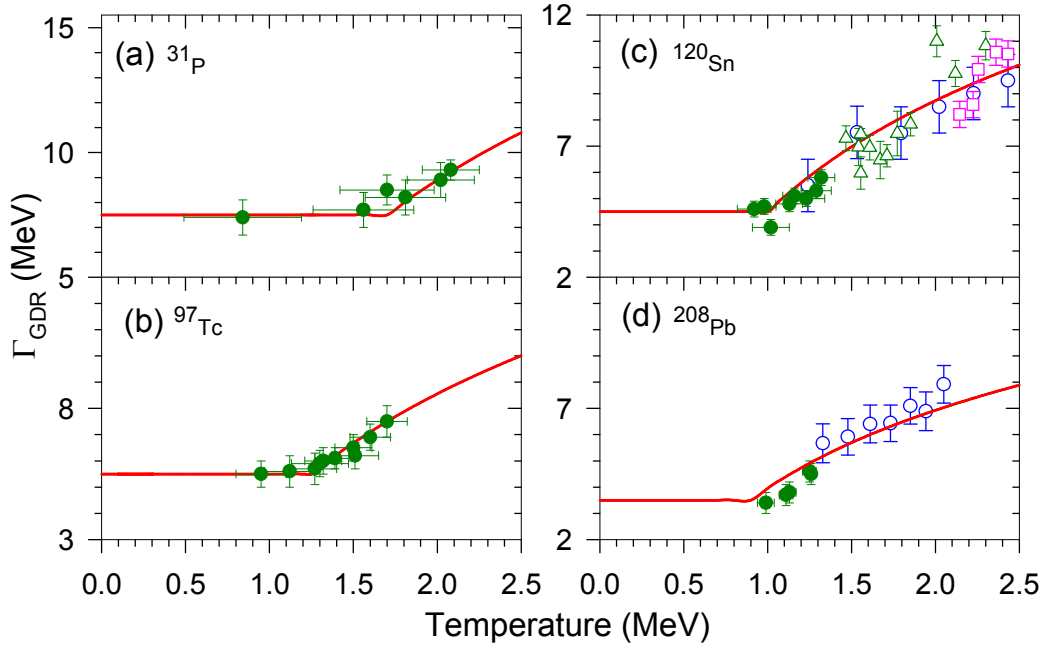


Figure 6.5: Comparison of the measured GDR widths (symbols) with the CTFM model calculations.

prescription of Ref. [Aue75], derived using  $\eta(0) = 1u$  [Fig. (6.6)]. According to the formalism,  $\Gamma_{\text{GDR}}(0) = 2.3 + 14/A^{1/3} + 21/A^{1/2}$  MeV. The authors derived this relation by solving the following equations for  $\omega$

$$1 - \frac{Lj_L(K_1 R)}{K_1 R j_{L+1}(K_1 R)} = \frac{(L+1)j_L(h_1 R)}{h_1 R j_{L+1}(h_1 R)}, \quad (6.3)$$

where

$$K_1^2 = \frac{\omega^2 - i\omega\gamma'\delta_{I,1}}{u_1^2 + \frac{4}{3}i\nu\omega}, \quad (6.4)$$

$$h_1^2 = -(i\omega + \gamma'\delta_{I,1})/\nu,$$

$$\eta = \rho\nu,$$

where  $\rho$  is the nuclear density  $= 0.16 \text{ fm}^{-3}$ . The descriptions of all parameters are given in section (2.4.1). In the present work,  $\eta(0)$  was also varied, keeping all other parameters fixed as used in Ref. [Aue75] (section (2.4.1), to reproduce the ground state GDR widths of  $^{97}\text{Tc}$  (upper bound) and  $^{201}\text{Tl}$  (lower bound) [Fig. (6.6)]. This results in the lower and the upper limits for  $\eta(0)$  as  $0.55u$

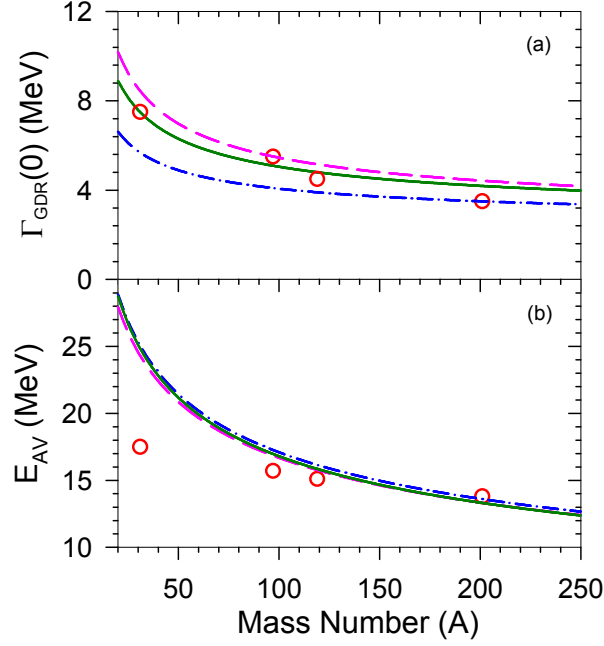


Figure 6.6: Variation of (a) the ground state GDR width and (b) average GDR energy with the mass number. The symbols are (a) the accepted ground state GDR width and (b) the average of the measured GDR energies. The blue dot-dashed, green solid and pink dashed lines are the calculated ground state GDR widths and energies for  $\eta(0) = 0.55u$ ,  $1.0u$ , and  $1.25u$ , respectively.

and  $1.25u$ , respectively. Interestingly, these bounds are quite similar to that ( $0.6u$  and  $1.2u$ ) used in Ref. [Dan11], which were obtained in Ref. [Dav76] by comparing the calculated and the experimental most probable fission-fragment kinetic energies. These bounds have been considered as systematic errors in the deduced quantities.

## 6.4 Determination of the entropy density

The entropy density was determined from the measured level density parameter and nuclear temperature by using the Fermi gas model prescription

$$\begin{aligned}
 s(T) &= \frac{\rho}{A} S(T) , \\
 S(T) &= 2a(T)T ,
 \end{aligned}
 \tag{6.5}$$

where the nuclear density  $\rho = 0.16 \text{ fm}^{-3}$  and  $A$  is the mass number of the nucleus.  $a(T)$  was deduced from the experimentally determined asymptotic NLD parameter  $\tilde{a}$  by using the Ignatyuk parameterization  $a(T) = \tilde{a}[1 + \frac{\Delta S}{U}\{1 - \exp(-\gamma U)\}]$  [Ign75]. The ground state shell correction values  $\Delta S$ , which are the difference of experimentally measured and liquid drop masses, were -2.23, -0.20, 0.22, and -8.31 MeV for  $^{31}\text{P}$ ,  $^{97}\text{Tc}$ ,  $^{119}\text{Sb}$ , and  $^{201}\text{Tl}$ , respectively. These shell correction values were calculated within the CASCADE code by using the droplet model of Myers and Swiatecki [Mye74] with the Wigner term. The damping factor  $\gamma$ , which determines the rate of shell effect depletion with excitation energy, was  $0.054 \text{ MeV}^{-1}$  [Ign75, Pra16]. It should be mentioned that  $\tilde{a}$  was not extracted from the neutron energy spectrum for  $^{201}\text{Tl}$ . The values of  $\tilde{a}$  used for fitting the high-energy  $\gamma$  ray spectra were utilized to extract the entropy density. Except for  $^{201}\text{Tl}$ ,  $\Delta S$  is very small for all other nuclei. This results in a minute effect of  $\Delta S$  and the damping factor ( $\gamma$ ) on deduced  $a(T)$  and  $T$  at the concerned nuclear excitations. However, following the recent measurements [Rou13, Pra16], an uncertainty of  $0.020 \text{ MeV}^{-1}$  has been included in the damping factor. This adds to maximum systematic uncertainties of 9% and 4% in  $a(T)$  and  $T$ , respectively for  $^{201}\text{Tl}$  at the lowest excitation. For other masses, these uncertainties are much smaller.

## 6.5 Results and discussions

In this work, the shear viscosity, entropy density, and the ratio of these two quantities have been determined experimentally in a self-consistent way at different mass regions and at different temperatures in the range 0.8-2.1 MeV. Fig. (6.7) shows the deduced quantities along with the respective calculations. The errors include the statistical error as well as the systematic error arising due to the variation in  $\eta(0)$ . The deduced shear viscosities are well reproduced for the

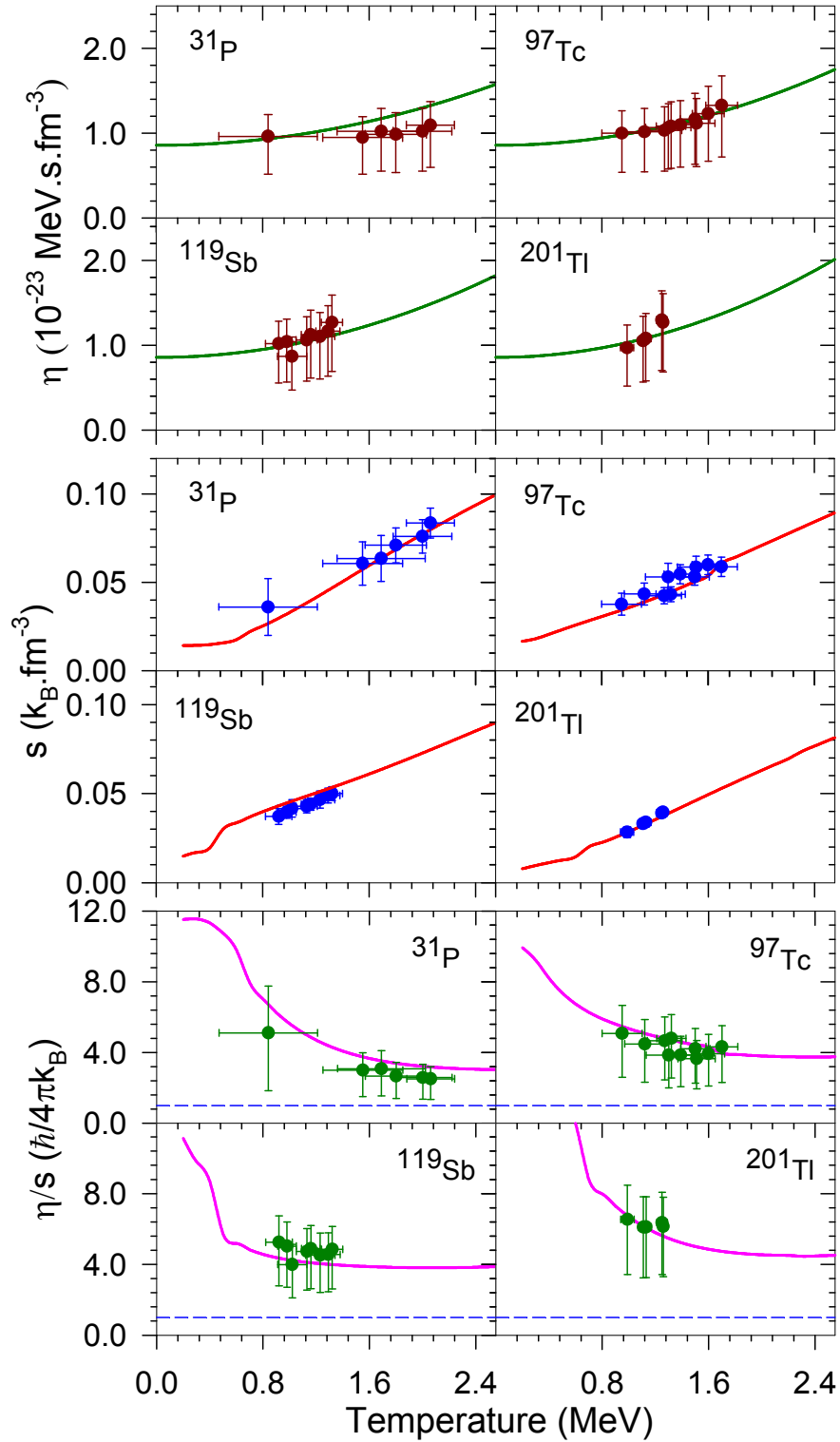


Figure 6.7: Experimental data (symbols) along with the theoretical predictions (solid lines) for  $\eta$  (upper panel),  $s$  (middle panel), and  $\eta/s$  (lower panel). Blue short-dashed line (lower panel) is the KSS bound.

systems by the calculations based on the generalized Fermi liquid drop model (FLDM) [Aue09, Kol04] (section 2.4.1). The model directly calculates  $\eta$  by utilizing the two-body collisional approach and gives  $\eta(T) = \frac{2}{5}\rho\epsilon_F\tau_{\text{coll}}/[1+(\omega\tau_{\text{coll}})^2]$ , where  $\epsilon_F$  is the Fermi energy,  $\omega$  is the angular frequency of excitation, and  $\tau_{\text{coll}}$  is the collision relaxation time given by  $\tau_{\text{coll}} = \tau_0/[1+(\hbar\omega/2\pi T)^2]$ ,  $\tau_0 = \hbar\alpha/T^2$ . In the rare collision (zero sound) regime (which corresponds to giant resonances)  $\omega\tau \gg 1$  and at low temperatures such that  $T \ll \hbar\omega$ , the shear viscosity reduces to  $\eta(T) = \frac{2}{5}\rho\epsilon_F\frac{\hbar}{4\pi^2\alpha} \times [1 + (2\pi T/\hbar\omega)^2]$ . The parameter  $\alpha$  depends on the in-medium nucleon-nucleon scattering cross section and for isovector resonances its value is 4.6 MeV [Kol04]. The theoretical results are obtained using the values of  $\epsilon_F = 37$  MeV, corresponding to  $\rho = 0.16$  fm<sup>-3</sup> and considering  $\hbar\omega$  as the average GDR energy. It is observed that at low temperatures,  $\eta$  increases with  $T$ , which can be understood qualitatively by the following arguments. For an equilibrated nucleus, the momentum is transported by the nucleons. The kinetic theoretical calculations give  $\eta \sim \bar{v}\lambda$ , where  $\bar{v}$  is the average velocity of the nucleons, and the mean free path  $\lambda \sim \bar{v}/N_{\text{coll}}$ . In the rare collision region, the collision frequency  $N_{\text{coll}}$  does not change much with temperature, while  $\bar{v} \sim \sqrt{T}$ . Therefore, the mean free path as well as the nucleon momentum increase with temperature. That means the momentum can be transported more efficiently over a large distance, thereby increasing  $\eta$  with temperature.

It is also interesting to note that the measured entropy density is well reproduced by the microscopic calculations (section 2.2).  $s(T)$  was estimated, in units of  $k_B$ , utilizing the relation  $s(T) = -\frac{\rho}{A} \times \sum_i [f_i \ln(f_i) + (1 - f_i) \cdot \ln(1 - f_i)]$ , where  $f_i$  is the occupation probability of the state with energy  $e_i$  given by  $f_i = [1 + \exp\{(e_i - \mu)/T\}]^{-1}$ . The chemical potential  $\mu$  was calculated from particle conservation viz.  $n = \sum_i f_i$ , and the single particle energies  $e_i$  for neutron and protons were calculated using the deformed Wood-Saxon potential

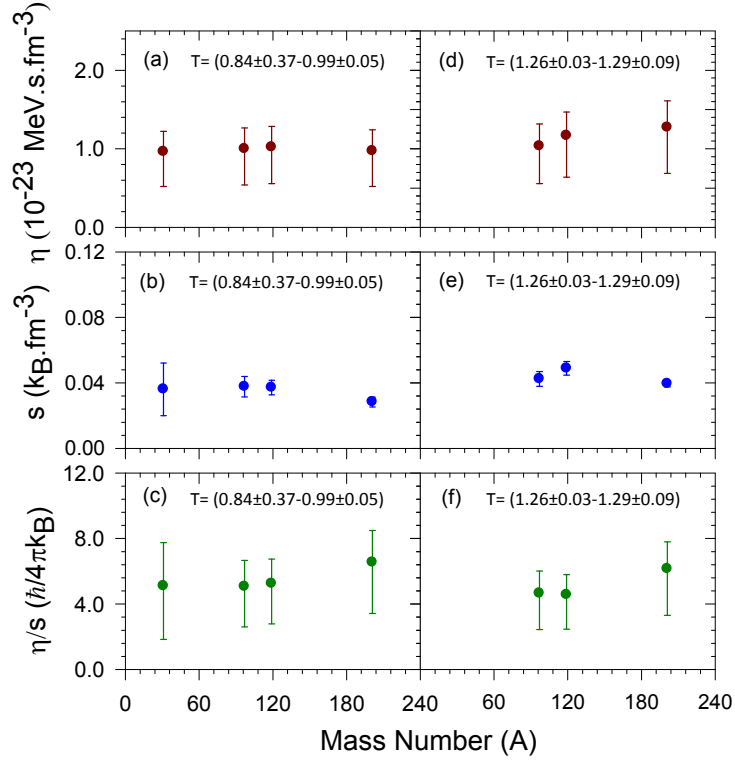


Figure 6.8: Variation of  $\eta$  (upper panel (a) & (d)),  $s$  (middle panel (b) & (e)), and  $\eta/s$  (lower panel (c) & (f)) with mass number at the specified temperature range.

with the universal parameters [Cwi87]. The entropy for the neutrons and the protons were calculated separately and were added to obtain the total entropy for the nucleus. As the temperature increases, the distortion of the Fermi surface becomes larger, thereby increasing the number of accessible microstates. This results in the increase in entropy density with temperature.

The deduced  $\eta/s$  shows (lower panel of Fig. (6.7)) a mild decrease with temperature. Moreover, it is confined in the range  $(2.5-6.5) \hbar/4\pi k_B$  for the finite nuclear matter within the temperature range  $\sim (0.8-2.1)$  MeV. Therefore, it could be concluded that nuclear matter obeys the KSS conjecture. Moreover, the measured  $\eta/s$  is comparable to that of the QGP for which  $\eta/s < 5 \hbar/4\pi k_B$  [Sch09]. It, therefore, could be reaffirmed, as pointed out in Ref. [Aue09], that

the strong fluidity is a universal characteristic feature of the strong interaction of the many-body nuclear systems and not just of the state created in the relativistic collisions. This result, along the results of low-temperature quantum fluids (for which  $\eta/s$  is of  $\sim 6-10 \hbar/4\pi k_B$  [Sch09]), suggests that large fluidity could also possibly be the intrinsic characteristic feature of strongly coupled systems. It is also fascinating to note from Fig. (6.8) that, although  $\eta$  shows a slight increase with the mass number (Fig. (6.8d)) at the highest available temperature for heavier nuclei,  $\eta/s$  remains within (5.1-6.5)  $\hbar/4\pi k_B$  (Fig. (6.8c)) and (4.6-6.1)  $\hbar/4\pi k_B$  (Fig. (6.8f)) at the lowest and highest available temperatures, respectively, for all nuclei (since the data at higher specified temperature range were not available for  $^{31}\text{P}$ , the high-temperature plots contain only three points). This indicates that  $\eta/s$  is approximately independent of the nuclear size and the neutron-proton asymmetry at a given temperature. However, it could be the artefact of incorporating the same  $\eta(0)$  for all nuclei. Also owing to large errors, the data are not sensitive enough to draw any conclusion and thus, call for further studies.

# Chapter 7

## Isospin Mixing in $^{32}\text{S}$ : Experiments, Results, and Discussions

In this chapter, the experimental study of isospin mixing in  $^{32}\text{S}$  at high excitation is presented. The principal objectives of this work [Deb16] were to exclusively measure the isospin mixing probability using light-ion-induced reactions and also measure the nuclear temperature which is crucial for proper interpretation of the measured data. The compound nuclei  $^{31}\text{P}$  and  $^{32}\text{S}$  were populated by the following reactions performed at the Variable Energy Cyclotron Centre, Kolkata.

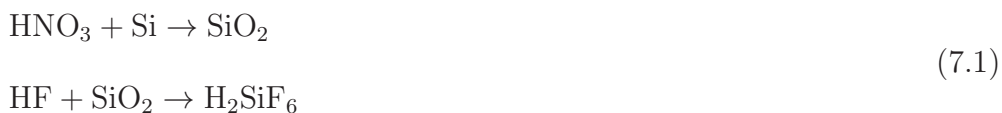
- (a)  $^4\text{He} (E_{\text{beam}} = 35 \text{ MeV}) + ^{27}\text{Al} \rightarrow ^{31}\text{P}^*$ ,
- (b)  $^4\text{He} (E_{\text{beam}} = 38 \text{ MeV}) + ^{28}\text{Si} \rightarrow ^{32}\text{S}^*$ ,

The nucleus  $^{31}\text{P}$  was populated as a reference nucleus at the same temperature and angular momentum but with a different entrance channel isospin to extract the GDR parameters. These parameters were then utilized for the analysis of  $^{32}\text{S}$ . As nearly all nucleons participate in the GDR, it is expected that the GDR

parameters would be the same (at a given temperature and angular momentum) for these two nearby nuclei. It should again be highlighted that due to the availability of light ion beam ( $\alpha$ ), the compound nuclei were populated at low angular momentum. Consequently, there was no influence of angular momentum on the GDR parameters and the high-energy  $\gamma$  ray spectra, which is observed in compound nuclei populated through heavy-ion-induced reactions specially at low mass regions. In such cases, the nuclei possess various exotic shapes such as Jacobi shape, cluster structure etc. resulting in complicated shapes of high-energy  $\gamma$  ray spectra [Maj04, Bre07, Dee10a].

## 7.1 Preparation of Silicon target

Silicon is a very brittle material and it is not easy to prepare a self-supporting thin silicon target with rolling technique. We prepared the target from a thick natural silicon wafer by chemical etching technique utilizing a solution of hydrofluoric acid (HF), nitric acid ( $\text{HNO}_3$ ) and acetic acid ( $\text{CH}_3\text{COOH}$ ) in the ratio of 4:7:11. Silicon is oxidized by nitric acid and produces silicon dioxide ( $\text{SiO}_2$ ) on the layer of Si wafer. This  $\text{SiO}_2$  layer reacts with HF and produces hydrofluosilicic acid ( $\text{H}_2\text{SiF}_6$ ).



$\text{H}_2\text{SiF}_6$  is easily removed from the surface and thus Si gets etched. One disadvantage of this method is that the side portion of the wafer gets etched very quickly. Therefore, the uniformity of the target was ensured by encapsulating the sides of the wafer with wax. In this method, we could prepare 10.8 mg thick Si target.

## 7.2 Experimental details and data reduction

The quantities that have been measured in the above mentioned experiments are

- (a) The high-energy  $\gamma$  ray spectra from the decay of the GDR measured using a part of the LAMBDA spectrometer,
- (b) The evaporated neutron energy spectra measured using TOF neutron detector, and
- (c) The low-energy  $\gamma$  ray multiplicity measured using the multiplicity detector array.

The experimental set-up and data reduction techniques were the same as described in detail in chapter 5 and also in section 6.1, in brief. That is why these are not being discussed here. The only important observation that should be pointed out that the fold distributions for both  $^{31}\text{P}$  and  $^{32}\text{S}$  are the same [Fig. (7.1)]. This implies that both compound nuclei were populated at the same average angular momentum. It is also evident from Fig. (7.1b) that the selected angular momentum space was slightly inclined to higher angular momenta. This is due to the fact that during data recording only those events were selected for which both the top and the bottom multiplicity filter fired in coincidence (section 5.5.2). This coincidence technique, despite selecting the higher angular momentum phase space, guarantees the selection of statistical events as well as a significant reduction in background events.

## 7.3 Extraction of NLD, GDR and isospin mixing parameters

In this thesis, the statistical model calculations were performed by using a modified version of the CASCADE code in which isospin and parity quantum

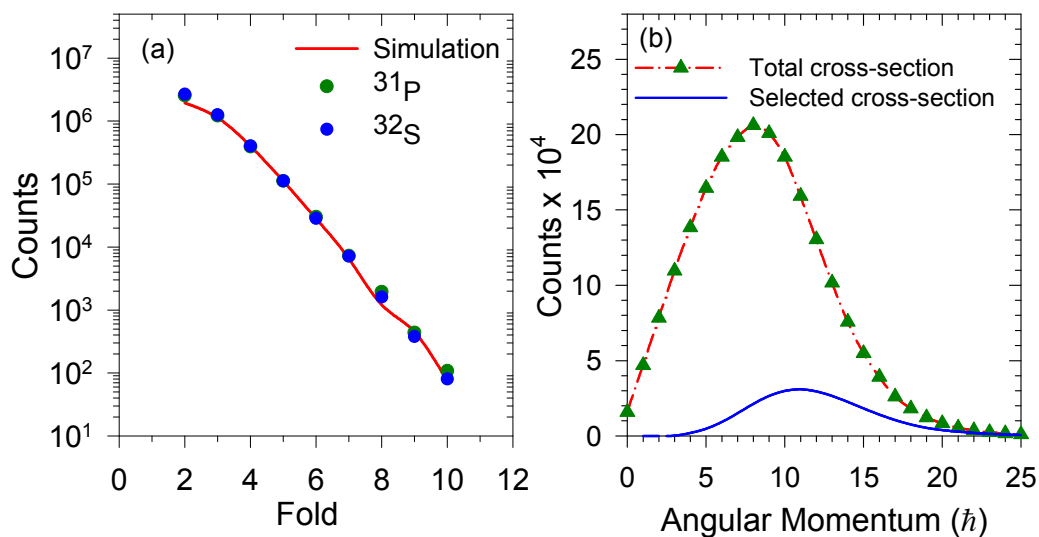


Figure 7.1: (a) Experimental fold distributions along with the simulated one. (b) The total fusion cross-section (arb. unit) (green solid triangles with red dot-dashed line) and the selected angular momentum distribution (solid blue line) for statistical model calculations.

numbers were properly taken care of. In this version of the CASCADE code the isospin was first included by Harakeh [Har86] and later it was modified by Behr [Beh91, Beh93]. The salient modifications that have been performed are

- (a) Each compound nuclear state was assigned with isospin and parity quantum numbers apart from the energy and angular momentum. Two lowest possible isospin states  $I_{<} \equiv |I, I = I_z\rangle$  and  $I_{>} \equiv |I + 1, I = I_z\rangle$  were considered in each nucleus.
- (b) The transmission co-efficient was multiplied by proper Clebsch-Gordan co-efficient for both particle and  $\gamma$  decay.
- (c) Level densities of each type of isospin states were calculated according to the prescriptions described in section (4.4.1).
- (d) Isospin splitting and strength distribution (described in section 3.4) for  $E1$   $\gamma$  transitions were properly taken care of.

As far as parity is concerned, it is not so important at high excitations as roughly both positive and negative parity states are populated equally. Also, it was assumed that the level densities are equally divided between both parity states. The isospin mixing was performed according to the prescription of Harney, Richter and Weidenmuller [Hrn86] (section 4.4.2). The fractions of  $\gtrsim$  states that goes to the  $\lesssim$  states by virtue of isospin mixing are given by

$$\alpha_{\gtrsim}^2 = \frac{\Gamma_{\gtrsim}^{\downarrow}/\Gamma_{\gtrsim}^{\uparrow}}{1 + \Gamma_{\gtrsim}^{\downarrow}/\Gamma_{\gtrsim}^{\uparrow} + \Gamma_{\lesssim}^{\downarrow}/\Gamma_{\lesssim}^{\uparrow}} \quad (7.2)$$

where  $\Gamma^{\downarrow}$  and  $\Gamma^{\uparrow}$  are the spreading width and the statistical decay width of the respective states. The mixed population cross sections are obtained from the cross sections of pure isospin states as follows

$$\begin{aligned} \tilde{\sigma}_{<} &= (1 - \alpha_{<}^2)\sigma_{<} + \alpha_{>}^2\sigma_{>} \\ \tilde{\sigma}_{>} &= (1 - \alpha_{>}^2)\sigma_{>} + \alpha_{<}^2\sigma_{<} \end{aligned} \quad (7.3)$$

where  $\sigma$  and  $\tilde{\sigma}$  are the pure and mixed population cross sections of the respective states. The simulated compound nuclear cross sections of  $^{31}\text{P}$  and  $^{32}\text{S}$ , properly normalized with the absolute value of the fusion cross section obtained from PACE4 calculations, were incorporated in the CASCADE code with the assumption that isospin is conserved i.e.  $\sigma_{<} \neq 0$  and  $\sigma_{>} = 0$ . Only  $\Gamma_{>}^{\downarrow}$  was incorporated as an input parameter and  $\Gamma_{<}^{\downarrow}$  and the decay widths were calculated within the CASCADE code. Once these quantities were calculated,  $\alpha_{\gtrsim}^2$  and  $\tilde{\sigma}_{\gtrsim}$  were deduced from Eqs. (7.2) and (7.3), respectively. The cross sections of the exit channels were then determined using these mixed population cross sections. These steps are followed at each and every step in the decay cascade.

The statistical model analysis for  $^{31}\text{P}$  was performed with the assumption that the isospin is fully conserved ( $\Gamma_{>}^{\downarrow} = 0$ ). First, the asymptotic NLD parameter ( $\tilde{a}$ ) was determined by comparing the measured evaporated neutron energy spectrum with the statistical model predictions. The calculated neutron

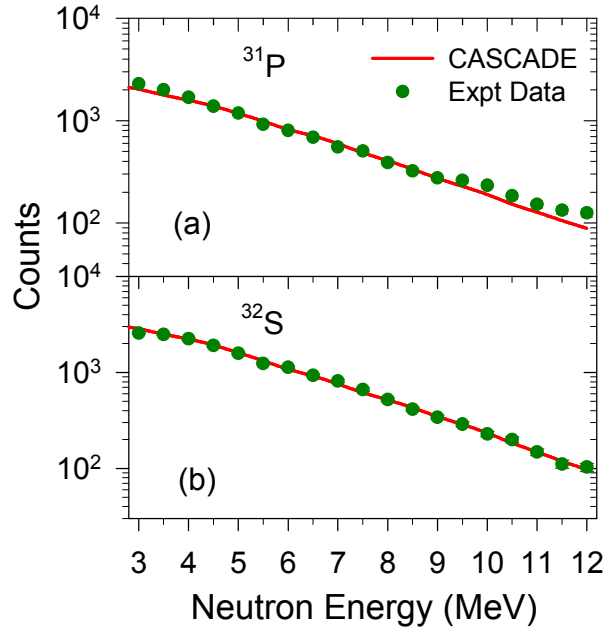


Figure 7.2: *Experimental neutron spectra (green filled circles) along with the CASCADE predictions corresponding to best values of  $\tilde{a}$  (red solid lines) for (a)  $^{31}\text{P}$  and (b)  $^{32}\text{S}$ .*

spectrum was corrected for detector efficiency and then was compared with the experimental spectrum. The Ignatyuk-Reisdorf level density prescription (section 4.3) was used and  $\chi^2$  minimization was performed in the energy range 4.0-10.0 MeV. The best fit value of  $\tilde{a}$  was found to be  $4.2 \pm 0.3 \text{ MeV}^{-1}$ . Similar analysis resulted in  $\tilde{a} = 3.9 \pm 0.1 \text{ MeV}^{-1}$  for  $^{32}\text{S}$ . The evaporated neutron energy spectra along with the CASCADE fit for both the nuclei are shown in Fig. (7.2).

In the next step, the IVGDR parameters were extracted by comparing the high-energy  $\gamma$  ray spectrum of  $^{31}\text{P}$  with the CASCADE calculations along with a small bremsstrahlung component parameterized as  $\sigma = \sigma(0)e^{-E_\gamma/E_0}$ . The slope parameter  $E_0 = 4.9 \text{ MeV}$  is consistent with the parameterization  $E_0 = 1.1[(E_{\text{beam}} - V_c)/A_p]^{0.72}$  [Nif90]. The deduced parameters were  $E_{\text{GDR}} = 17.8 \pm 0.2 \text{ MeV}$ ,  $\Gamma_{\text{GDR}} = 8.0 \pm 0.4 \text{ MeV}$  and  $S_{\text{GDR}} = 1.00 \pm 0.03$ . The uncertainties were obtained by  $\chi^2$  minimization procedure in the energy range 14 - 21 MeV.

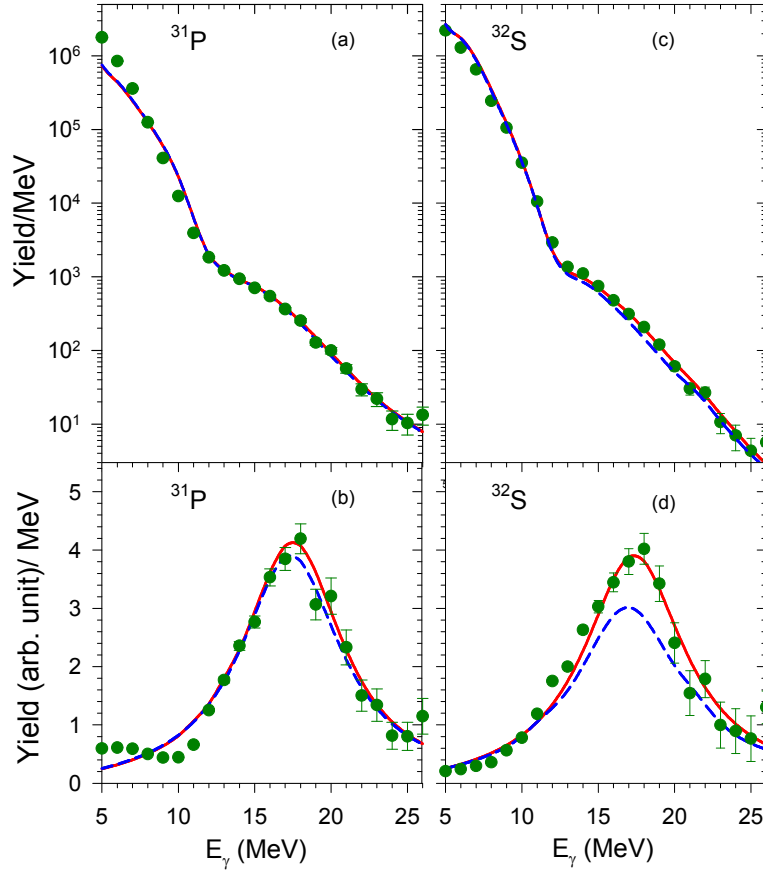


Figure 7.3: (a) Experimental high-energy  $\gamma$  ray spectra (green filled circles) along with CASCADE calculations for  $\Gamma_{>}^\downarrow = 0$  keV (blue dashed line) and  $\Gamma_{>}^\downarrow = 24$  keV (red solid line) for  $^{31}\text{P}$  (a) and  $^{32}\text{S}$  (c). The corresponding linearized plots are also shown for  $^{31}\text{P}$  (b) and  $^{32}\text{S}$  (d).

The experimental high-energy  $\gamma$  ray spectrum for  $^{31}\text{P}$  along with the CASCADE spectra, properly folded with the detector response function, are shown in Fig. (7.3a). In order to emphasize on the GDR region the corresponding linearized spectra are shown in Fig. (7.3b) using the quantity  $F(E_\gamma)Y^{\text{exp}}(E_\gamma)/Y^{\text{cal}}(E_\gamma)$ , where  $Y^{\text{exp}}(E_\gamma)$  and  $Y^{\text{cal}}(E_\gamma)$  are the experimental and the CASCADE spectra, while  $F(E_\gamma)$  is the Lorentzian having the above mentioned parameters.

Finally, the isospin mixing parameters were deduced utilizing the IVGDR parameters extracted from  $^{31}\text{P}$ . In order to increase the sensitivity of isospin

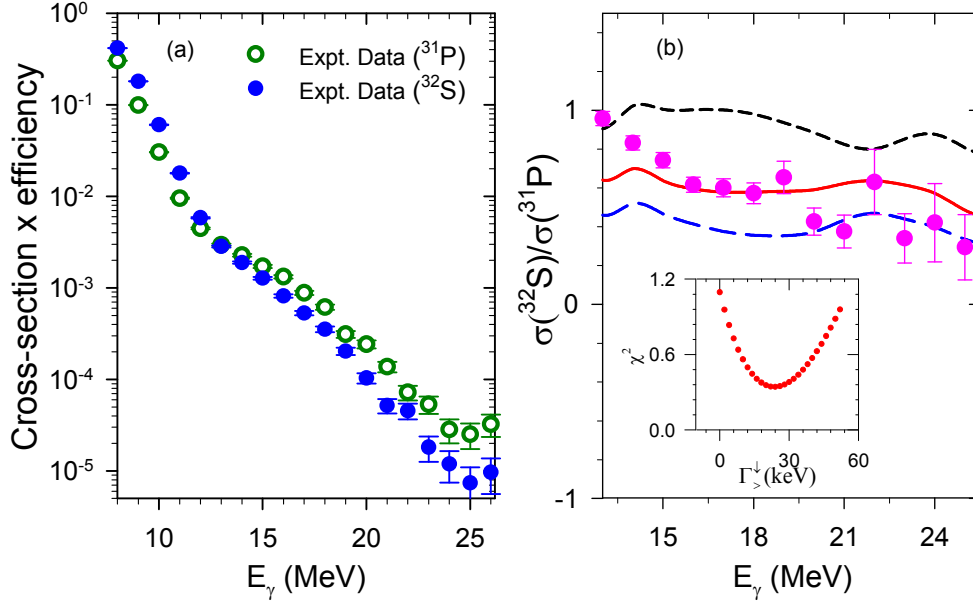


Figure 7.4: (a) Experimental  $\sigma_\gamma \times \epsilon_{in}$  for  $^{31}\text{P}$  (green open circles) and  $^{32}\text{S}$  (blue filled circles). (b) Experimental ratio (pink filled circles) of the  $\gamma$  ray cross section of  $^{32}\text{S}$  and  $^{31}\text{P}$  along with the CASCADE predictions for different  $\Gamma_\downarrow^\downarrow$ .  $\Gamma_\downarrow^\downarrow = 0$  keV for blue long-dashed line (zero mixing),  $\Gamma_\downarrow^\downarrow = 24$  keV for red solid line and  $\Gamma_\downarrow^\downarrow = 10$  MeV for black short-dashed line (full mixing).  $\chi^2$  as a function of  $\Gamma_\downarrow^\downarrow$  (inset Fig. b).

mixing and minimize the effects of statistical model parameters, isospin mixing parameters were deduced from the ratio of  $\gamma$  ray cross sections of  $^{32}\text{S}$  and  $^{31}\text{P}$  in the GDR region [Fig. (7.4b)]. We remark here that though we could simulate the response function of LAMBDA spectrometer, the absolute efficiency ( $\epsilon_{in}$ ) of the array is not known. So, we have taken the ratio of  $[\sigma_\gamma \times \epsilon_{in}]$  for both the nuclei and compared with the ratio of the CASCADE cross-sections properly folded with the detector response function. It should be highlighted here that  $\Gamma_\downarrow^\downarrow$  was the only parameter that was varied to match the experimental ratio with the CASCADE prediction. As  $\Gamma_\downarrow^\downarrow$  remains nearly temperature independent [Hrn86, Kuh79], the same  $\Gamma_\downarrow^\downarrow$  was used for all the decay steps. The best value for  $\Gamma_\downarrow^\downarrow$  was obtained by  $\chi^2$  minimization technique in the energy range 14-21 MeV and was found to be  $24 \pm 13$  keV. The resulting values of isospin mixing

Table 7.1: Experimentally determined values of isospin mixing parameter

Angular Momentum ( $\hbar$ )	Temperature (MeV)	Parameter	Value (%)
$\langle J \rangle = 12$	2.6	$\alpha_{<}^2$	$3.5 \pm 1.8$
$J = 1$	3.2	$\alpha_{>}^2$	$3.5 \pm 1.9$

parameters are given in table (7.1). The temperature was calculated using the relation  $T = \sqrt{(E^* - E_{\text{rot}} - \Delta P)/\tilde{a}}$ , where  $E_{\text{rot}}$  is the rotational energy and  $\Delta P$  is the pairing energy. The experimental high-energy  $\gamma$  ray spectrum for  $^{32}\text{S}$  along with the CASCADE fits for  $\Gamma_{>}^{\downarrow} = 0$  keV and  $\Gamma_{>}^{\downarrow} = 24$  keV are shown in Fig. (7.3c) and the corresponding linearized plots are shown in Fig. (7.3d). It is also interesting to observe from Figs. (7.3a) and (7.3b) that  $\Gamma_{>}^{\downarrow}$  does not affect the high-energy  $\gamma$  ray spectrum for  $^{31}\text{P}$  which reaffirms the fact that E1  $\gamma$  transitions in a non-self-conjugate nucleus are not influenced by isospin mixing. It should be emphasized that the presentations [Fig. (7.3)] depend on the normalization point of experimental and theoretical spectra; however, the extracted  $\Gamma_{>}^{\downarrow}$  from the ratio of the cross section of  $^{32}\text{S}$  and  $^{31}\text{P}$ , and the resulting isospin mixing parameters are completely independent of the normalization point. It should also be mentioned that isospin mixing parameters depend on  $J$ . This is because the intrinsic decay width of a nuclear state, which governs the values of isospin mixing parameters [Eq. (7.2)], depends on angular momentum. The variation of isospin mixing parameter with angular momentum is shown in Fig. (7.5).

The quoted errors in  $\Gamma_{>}^{\downarrow}$  and  $\alpha_{\lessgtr}^2$  correspond to the statistical errors as well as systematic errors owing to the presence of isotopic impurity in the  $^{28}\text{Si}$  target and the uncertainty in the determination of non-statistical bremsstrahlung component. The contributions due to isotopic impurity mainly come from  $^{29}\text{Si}$  and  $^{30}\text{Si}$ . As mentioned earlier the bremsstrahlung component was parameterized with exponential function  $\sigma = \sigma(0)e^{-E_{\gamma}/E_0}$ . The slope parameter  $E_0$  is

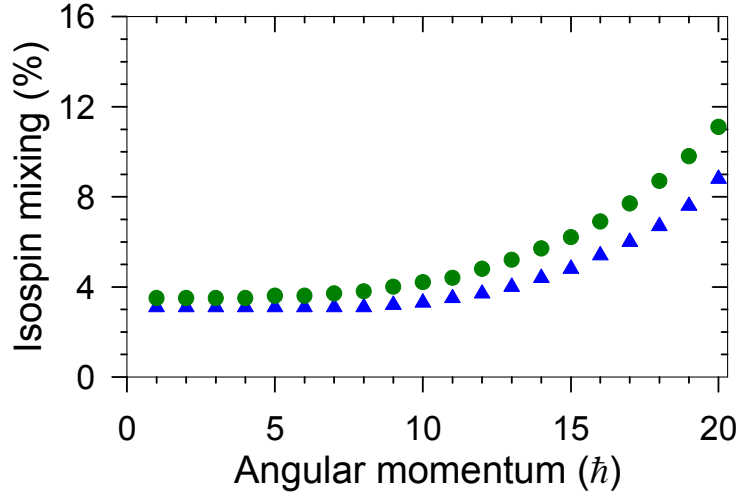


Figure 7.5: Variation of isospin mixing parameters with angular momentum. The green circles represent  $\alpha_{>}^2$ , while the blue triangles stand for  $\alpha_{<}^2$ .

determined from the angular distribution of high-energy  $\gamma$  rays. The value  $\sigma(0)$  depends on the number of n-p collisions [Nif90]. For the present systems the number of n-p pairs are small and  $\sigma(0)$  was determined by fitting the high-energy  $\gamma$  ray spectrum in  $\sim 20$ -25 MeV region through eye estimation. The contribution of bremsstrahlung was found to be less than 5% of the GDR  $\gamma$  ray contribution. As  $\Gamma_{>}^{\downarrow}$  was determined from the ratio of  $\gamma$ -ray cross sections of  $^{32}\text{S}$  and  $^{31}\text{P}$ , the effect of bremsstrahlung component is nearly nullified. However, the bremsstrahlung contribution is additive and can not be nullified completely. The quoted errors contain the maximum uncertainty owing to the selection of the bremsstrahlung component.

## 7.4 Results and discussions

The Coulomb spreading width ( $\Gamma_{>}^{\downarrow}$ ) for  $^{32}\text{S}$  extracted in this work is comparable with other measurements as shown in Fig. (7.6). The data points are comprised of the width of isobaric analog states (IAS) and the spreading width obtained

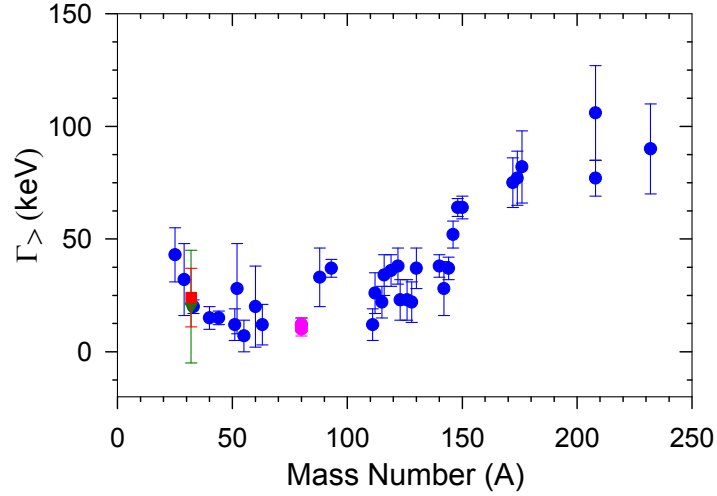


Figure 7.6: Variation of the Coulomb spreading width with mass number. The red square is the present measurement and the green circle is the measured datum of Ref. [Hab04] for  $^{32}\text{S}$ . The pink circles are the measured data for  $^{80}\text{Zr}$  [Cor11, Cer15]. (adopted from Ref. [Cer16]).

from compound nuclear reactions. The physical origin of both widths are the same i.e. mixing due to Coulomb interaction. It is obvious from Fig. (7.6), that the Coulomb spreading width remains roughly constant with nuclear mass. The slight increase at high mass region can be attributed to the increase in Coulomb interaction owing to the increase in proton number. It is also interesting to note that the present measured  $\Gamma_{>}^{\downarrow}$  (red square) is comparable to that obtained in Ref. [Hab04] (green circle) using the same formalism. This ([Hab04]) is the only other measurement available for  $^{32}\text{S}$  at temperature  $T = 2.85$  MeV which resulted in  $\Gamma_{>}^{\downarrow} = 20 \pm 25$  keV corresponding to  $\alpha_{<}^2 = 1.3 \pm 1.5\%$ . These results emphasize the fact that  $\Gamma_{>}^{\downarrow}$  indeed remains constant with temperature which was also observed for  $^{80}\text{Zr}$  [Cor11, Cer15]. Also, in Ref. [Hab04],  $^{32}\text{S}$  was populated using heavy ion reaction [ $^{20}\text{Ne}$  ( $E_{beam}=105$  MeV) +  $^{12}\text{C} \rightarrow ^{32}\text{S}$ ] for which the average angular momentum  $16\hbar$  (obtained using PACE4 calculations) as compared to the present measurement at average angular momentum  $12\hbar$ . Therefore, it could also be conjectured that the Coulomb spreading width remains constant with angular

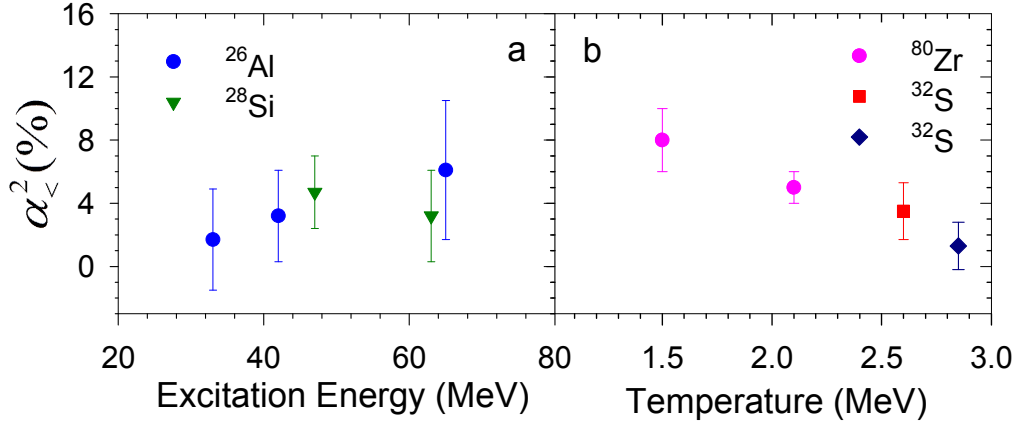


Figure 7.7: The isospin mixing parameter  $\alpha_z^2$  as a function of (a) excitation energy (b) temperature. In Fig. (b) the red square is the present measurement, while the dark blue diamond represents the measured datum of Ref. [Hab04] for  $^{32}\text{S}$ .

momentum.

As shown in Fig. (7.5), the isospin mixing parameter  $\alpha_z^2$  depend on angular momentum. In literature, therefore, weighted average of isospin mixing parameter is quoted, the weight being the yield of high-energy  $\gamma$  rays obtained as a product of fusion cross section and the  $\gamma$  branching ratio. In this thesis, the same convention has been followed and  $\alpha_z^2$  provides the average value of isospin mixing, unless mentioned otherwise. In Fig. (7.7) the measured isospin mixing parameters are compared with the other measurements performed using the same procedure [Beh93, Hab04, Cor11, Cer15] (i.e. the formalism of Harney, Richter and Widenmueller [Hrn86]). As isospin mixing depends on both temperature and nuclear charge ( $Z$ ), only those results have been considered for which measurements are available at different temperatures or excitation energies for a given system. In Fig. (7.7a), the results of the pioneering work of Behr *et al.* [Beh93] are presented as a function of initial excitation energy. By inclusive measurements, it has been shown that for  $^{28}\text{Si}$ , the isospin mixing decreases with the increase in excitation energy. However,  $^{26}\text{Al}$ , though with large errors,

isospin mixing was found to increase with excitation energy. As nuclear temperature is more fundamental quantity than excitation energy, in recent years, the results are quoted in terms of temperature. As can be seen from Figs. (7.7a) and (7.7b), the present measurement (red square) is comparable with the other measurements in this mass region and excitation energy. The present result, along with the result of Ref. [Hab04] (dark blue symbol in Fig. (7.7b)), suggests that isospin becomes a good quantum number at higher excitations for a given system. Similar results were observed for  $^{80}\text{Zr}$  [Cor11, Cer15]. These observations are in conformity with the Wilkinson conjecture [Wil56] which states that at high excitations the lifetime of the individual states becomes so small that they do not get sufficient time to mix, resulting in the restoration of isospin symmetry.

### 7.4.1 Comparison with the calculation at high temperature

It is interesting to compare the measured  $\alpha_{>}^2$  at minimum angular momentum( $1\hbar$ ) with the calculation of Sagawa *et al.* [Sag98]. According to the formalism (section 3.2.2)

$$\alpha_{>}^2 = \frac{1}{I_z + 1} \frac{\Gamma_{\text{IAS}}}{\Gamma_{\text{CN}} + \Gamma_{\text{IVM}}}, \quad (7.4)$$

where  $\Gamma_{\text{IAS}}$  is the spreading width of the IAS, which is equivalent to  $\Gamma_{>}^{\downarrow}$ .  $\Gamma_{\text{CN}}$  is the compound nuclear decay width and  $\Gamma_{\text{IVM}}$  is the width of the isovector monopole (IVM) state at the energy of the IAS. Since this formalism does not involve angular momentum, the measured  $\alpha_{>}^2$  has been considered at the lowest angular momentum. The value of  $\alpha_{>}^2$  was set at 0.7% at  $T = 0$  from the recent calculation of Satula *et al.* [Sat09] [Fig. (3.1)]. This results in  $\Gamma_{\text{IVM}} = 3.4$  MeV as  $\Gamma_{\text{CN}} = 0$  at  $T = 0$ . Next,  $\Gamma_{\text{CN}}$  was calculated using the CASCADE code at different temperatures using the best fit parameters. The resulting calculation

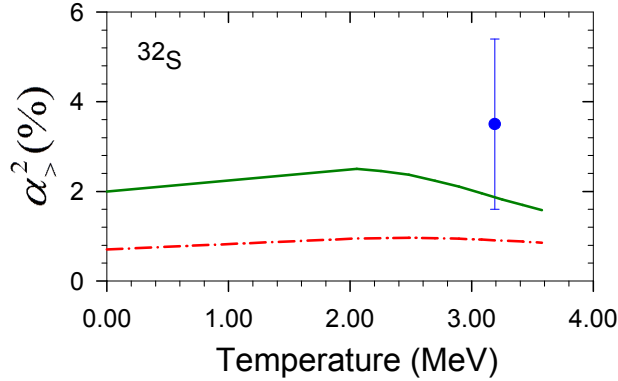


Figure 7.8: Comparison of  $\alpha_{>}^2$  with calculation at high temperature [Sag98].

is shown by red dot-dashed line in Fig. (7.8). It should be mentioned here that  $\Gamma_{\text{IVM}}$  was assumed temperature independent and  $\Gamma_{>}^{\downarrow}$  was given a weak linear dependence [Sag98] on  $T$  as  $\Gamma_{>}^{\downarrow}(T) = \Gamma_{>}^{\downarrow}(0)(1 + cT)$  where  $c = 0.2 \text{ MeV}^{-1}$ . The parameter  $c$  was calculated by assuming that  $\Gamma_{>}^{\downarrow}(T = 2.6 \text{ MeV}) = 37 \text{ keV}$  i.e.  $\Gamma_{>}^{\downarrow}$  remained within the experimental error bar. As can be seen from Fig. (7.8) that measured  $\alpha_{>}^2 = 3.5 \pm 1.9 \%$  remains well above the calculated value.

The value of  $\alpha_{>}^2$  at  $T = 0$  has also been extracted using the calculated value of  $\delta_c = 0.65 \%$  in  $^{34}\text{Cl}$  which nearly reproduces the corrected  $ft$  value [Har15]. At present, the corrected average  $ft$  value is  $3072.27 \pm 0.62 \text{ s}$ , while the corrected  $ft$  value in  $^{34}\text{Cl}$  obtained by using  $\delta_c = 0.65 \%$  is  $3070.70 \pm 1.75 \text{ s}$  [Har15].  $\alpha_{>}^2$  is extracted utilizing the formalism of Ref. [Aur09] with the assumption that  $\delta_c$  is same for  $^{34}\text{Cl}$  and  $^{32}\text{S}$ . According to this formalism  $\alpha_{>}^2$  is defined as

$$\alpha_{>}^2 = \frac{41\xi A^{2/3}}{4(I+1)V_1} \delta_c, \quad (7.5)$$

where  $V_1 = 100 \text{ MeV}$ ,  $\xi = 3$  [Aur09]. Eq. (7.5) yields  $\alpha_{>}^2 = 2.0 \%$  which in turn yields  $\Gamma_{\text{IVM}} = 1.2 \text{ MeV}$ .  $\alpha_{>}^2$  was extrapolated to higher temperatures using the same procedure described before. As can be seen from Fig. (7.8) the calculation (solid green line), though underpredicts, better explains the

measured datum. It should be highlighted in this context that Melconian *et al.* [Mel11] have found  $\delta_c$  to be as high as  $5.3 \pm 0.9$  % which was attributed to the presence of close lying  $I = 0$  and  $I = 1$  states near 7.0 MeV excitation energy in  $^{32}\text{S}$  and it was corroborated by the shell model calculations. So, it would be interesting to perform the statistical model analysis with the local effects but is beyond the scope of the present thesis. It should be highlighted here that, as mentioned therein, the formalism of Sagawa *et al.* [Sag98] may be valid only in medium-heavy and heavy nuclei. It could also be possible that at low mass region the isospin mixing has some finite value at zero temperature, then it gradually increases with temperature and then decreases in the statistical region (as is conceived qualitatively). Thus, in future, exclusive measurements in the transition region are called for better understanding on the variation of isospin mixing with temperature at low mass region.



# Chapter 8

## Summary, Conclusion and Outlook

The present thesis deals with the experimental study of two crucial aspects of atomic nuclei at finite temperatures utilizing the isovector giant dipole resonance as a probe. The first part contains a self-consistent experimental determination of the ratio of shear viscosity to entropy density for equilibrated finite nuclear matter from  $A \sim 30$  to  $A \sim 208$  at different temperatures, while the second part presents an experimental study of isospin mixing at high temperature in  $^{32}\text{S}$ . The high-energy  $\gamma$  ray spectra from the decay of GDR, evaporated neutron energy spectra, and the low-energy  $\gamma$  ray multiplicity have been measured using the LAMBDA spectrometer, neutron TOF detector and multiplicity filter, respectively.

This is the first self-consistent experimental determination of  $\eta/s$  for finite nuclear matter. The shear viscosity at finite temperature has been determined from measured GDR width and energy. The entropy density has been deduced from nuclear level density parameter and nuclear temperature, determined precisely by simultaneous measurements of evaporated neutron energy spectra and

angular momenta. The importance of this work lies in the fact that the parameters required for the determination of shear viscosity at finite temperatures have been extracted simultaneously with those required for the determination of entropy density. The deduced shear viscosities for all the systems have been reproduced quite well with the calculations based on the generalized Fermi liquid model, while the microscopic calculations of entropy density match well with extracted entropy density. The deduced values of  $\eta/s$  remain confined in the range (2.5-6.5)  $\hbar/4\pi k_B$  in the temperature range 0.8-2.1 MeV. Thus, this result establishes that the nuclear fluid conform to the KSS conjecture and strong fluidity is the universal characteristic of the strong interaction of the many-body nuclear systems. The present result, along the results of low-temperature quantum fluids and high-temperature quark gluon plasma, suggests that large fluidity could also possibly be the intrinsic characteristic feature of strongly coupled systems. It would be interesting to explore the variation of  $\eta/s$  with neutron-proton asymmetry as well as the lower bound of  $\eta/s$  proponed in literature. Also, the proposed variation of the energy of dynamic dipole resonance mode with  $\eta/s$  is an intriguing problem worth investigating in future.

In the second part of this thesis, exclusive measurement of isospin mixing in  $^{32}\text{S}$  at high temperature has been discussed. The compound nuclei  $^{31}\text{P}$  and  $^{32}\text{S}$  have been populated at the same excitation energy and angular momentum but with different entrance channel isospins to extract the isospin mixing probability in  $^{32}\text{S}$ . The GDR parameters have been extracted from the high-energy  $\gamma$  ray spectra of  $^{31}\text{P}$ . Utilizing these parameters the isospin mixing probability has been extracted from the ratio of high-energy  $\gamma$  ray spectra of  $^{32}\text{S}$  and  $^{31}\text{P}$ . Apart from that, the nuclear level density parameter and angular momentum have been determined for both nuclei from the measured evaporated neutron energy spectra and low-energy  $\gamma$  ray multiplicity, respectively. Thus, the nuclear

temperature which is crucial for proper interpretation of the experimental data has been determined precisely. This measurement, along with the previous ones performed utilizing the same procedure, suggests that the Coulomb spreading width indeed remains constant with both temperature and angular momentum. The isospin becomes a good quantum number with the increase in temperature. This is corroborated by Wilkinson's prescription which states that the lifetime of the individual states becomes so small that they do not get sufficient time to mix. However, the theoretical model of Sagawa *et al.*, which nicely reproduces the measured isospin mixing probability at high mass region, underpredicts the measured data at low mass region. This suggests that the prescription of Sagawa *et al.* may be valid, as mentioned by the authors themselves, in medium and heavy mass regions only. However, In future, systematic measurements for a given system and more theoretical insights are required for proper understanding of the variation of isospin mixing with temperature in lower mass region.



# Bibliography

- [Aam10] K. Aamodt *et al.* (ALICE Collaboration), Phys. Rev. Lett. **105** (2010) 252302.
- [Adl03] S. S. Adler *et al.* (PHENIX Collaboration), Phys. Rev. Lett. **91** (2003) 182301.
- [Ago03] S. Agostinelli *et al.* (Geant4 Collaboration), Nucl. Instr. and Meth. A **506** (2003) 250.
- [Aky71] R. O. Akyuev *et al.*, Phys. Rev. Lett. **27** (1971) 1016.
- [Alh88] Y. Alhassid *et al.*, Phys. Rev. Lett. **61** (1988) 1926.
- [Aue75] N. Auerbach *et al.*, Ann. Phys. (NY) **95** (1975) 35.
- [Aue09] N. Auerbach *et al.*, Phys. Rev. Lett. **103** (2009) 172501.
- [Aur09] N. Auerbach, Phys. Rev. C **79** (2009) 035502.
- [Axe62] P. Axel, Phys. Rev. **126** (1962) 671.
- [Bal14] Balaram Dey *et al.*, Phys. Lett. B **731** (2014) 92.
- [Bal15] Balaram Dey, PhD Thesis, HBNI, India, 2015.
- [Bal47] G. C. Baldwin *et al.*, Phys. Rev. **71** (1947) 3.

- [Bau98] T. Baumann *et al.*, Nucl. Phys. A **635** (1998) 428.
- [Bec69] F. D. Becchetti Jr. *et al.*, Phys. Rev. **182** (1969) 1190.
- [Beh91] J. A. Behr, PhD Thesis, University of Washington, 1991.
- [Beh93] J. A. Behr *et al.*, Phys. Rev. Lett. **70** (1993) 3201.
- [Ber75] B. L. Berman *et al.*, Rev. Mod. Phys. **47** (1975) 713.
- [Blo08] I. Bloch *et al.*, Rev. Mod. Phys. **80** (2008) 885.
- [Boh99] A. Bohr and B. R. Mottelson, *Nuclear Structure Vol II*, World Scientific Publishing (1999).
- [Boh99a] A. Bohr and B. R. Mottelson, *Nuclear Structure Vol I*, World Scientific Publishing (1999).
- [Bor98] P. F. Bortignon, A. Bracco, and R. A. Broglia, *Giant Resonances : Nuclear Structure at Finite Temperature*, Harwood Academic Publishers (Australia 1998).
- [Bot37] W. Bothe *et al.*, Z. Phys. **71** (1937) 236.
- [Bow82] T. J. Bowles *et al.*, Phys. Rev. Lett. **48** (1982) 986.
- [Bra89] A. Bracco *et al.*, Phys. Rev. Lett. **62** (1989) 2080.
- [Bra95] A. Bracco *et al.*, Phys. Rev. Lett. **74** (1995) 3748.
- [Bre07] M. Brekiesz *et al.*, Nucl. Phys. A **788** (2007) 224c.
- [Bri55] D. M. Brink, PhD Thesis, University of Oxford, 1955.
- [Bro59] G. E. Brown *et al.*, Phys. Rev. Lett. **3** (1959) 472.

- [Bro67] G. E. Brown *Unified Theory of Nuclear Models and Forces*, second edition, North-Holland, Amsterdam, (1967)
- [Bru86] R. Brun *et al.*, GEANT3, CERN-DD/EE/84-1, 1986.
- [Buc05] A. Buchel *et al.*, Nucl. Phys. B **707** (2005) 56.
- [Cer15] S. Ceruti *et al.*, Phys. Rev. Lett. **115** (2015) 222502.
- [Cer16] S. Ceruti, PhD Thesis, University of Milan, 2016.
- [Cer17] S. Ceruti *et al.*, Phys. Rev. C **95** (2017) 014312.
- [Che07] J. W. Chen *et al.*, Phys. Lett. B **647** (2014) 371.
- [Che08] A. Cherman *et al.*, J. High Energy Phys. **02** (2008) 026.
- [Cie15] M. Ciemala *et al.*, Phys. Rev. C **91** (2015) 054313.
- [Coh07] T. D. Cohen, Phys. Rev. Lett. **99** (2007) 021602.
- [Col95] G. Colo *et al.* Phys. Rev. C **52** (1995) R1175(R).
- [Cor11] A. Corsi *et al.*, Phys. Rev. C **84** (2011) 041304(R).
- [Cre11] S. Cremonini, arXiv:1108.0677
- [Cwi87] S. Cwiok *et al.*, Comp. Phys. Comm. **46** (1987) 379.
- [Dan11] N. D. Dang, Phys. Rev. C **84** (2011) 034309.
- [Dan12] N. D. Dang, Phys. Rev. C **85** (2012) 064323.
- [Dan84] P. Danielewicz, Phys. Lett. B **146** (1984) 168.
- [Dan98a] N. D. Dang *et al.*, Phys. Rev. Lett. **80** (1998) 4145.
- [Dan98b] N. D. Dang *et al.*, Nucl. Phys. A **636** (1998) 427.

- [Dav76] K. T. R. Davies *et al.*, Phys. Rev. C **13** (1976) 2385.
- [Deb16] Debasish Mondal *et al.*, Phys. Lett. B **763** (2016) 422.
- [Deb17] Debasish Mondal *et al.*, Phys. Rev. Lett. **118** (2017) 192501.
- [Dee10] Deepak Pandit *et al.*, Nucl. Instr. and Meth. A **624** (2010) 148.
- [Dee10a] Deepak Pandit *et al.*, Phys. Rev. C **81** (2010) 061302(R).
- [Dee12] Deepak Pandit *et al.*, Phys. Lett. B **713** (2012) 434 .
- [Den16] X. G. Deng *et al.*, Phys. Rev. C **94** (2016) 044622.
- [Die71] E. M. Diener *et al.*, Phys. Rev. C **3** (1971) 2303.
- [Die74] F. S. Dietrich *et al.*, Phys. Rev. C **10** (1974) 795.
- [Dob95] Jacek Dobaczewski *et al.*, Phys. Lett. B **345** (1995) 181.
- [Fal70] S. Fallieros *et al.*, Nucl. Phys. A **147** (1970) 593.
- [Fan14] D. Q. Fang *et al.*, Phys. Rev. C **89** (2014) 047601.
- [Far03] E. Farnea *et al.*, Phys. Lett. B **551** (2003) 56.
- [Gal87] M. Gallardo *et al.*, Phys. Lett. B **191** (1987) 222.
- [Gho16] C. Ghosh *et al.*, Phys. Rev. C **94** (2016) 014318.
- [Gio08] S. Giorgini *et al.*, Rev. Mod. Phys. **80** (2008) 1215.
- [Gol48] M. Goldhaber *et al.*, Phys. Rev. **74** (1948) 1046.
- [Hab04] M. Kicinska-Habior *et al.*, Nucl. Phys. A **731** (2004) 138.
- [Hab05] M. Kicinska-Habior, Acta Physica Polonica B **36** (2005) 1133.
- [Hab90] M. Kicinska-Habior *et al.*, Phys. Rev. C **41** (1990) 2075.

- [Har01] M. N. Harakeh and A. van der Woude, *Giant Resonances, Fundamental High – frequency Modes of Nuclear Excitation*, Clarendon Press, Oxford, 2001.
- [Har05a] J. C. Hardy *et al.*, Phys. Rev. Lett. **94** (2005) 092502.
- [Har05b] J. C. Hardy *et al.*, Phys. Rev. C **71** (2005) 055501.
- [Har15] J. C. Hardy *et al.*, Phys. Rev. C **91** (2015) 025501.
- [Har86] M. N. Harakeh *et al.*, Phys. Lett. B **176** (1986) 297.
- [Har99] K. M. O’Hara *et al.*, Phys. Rev. Lett. **82** (1999) 4204.
- [Hec03] P. Heckman *et al.*, Phys. Lett. B **555** (2003) 43.
- [Hei32] W. Heisenberg, Z. Phys. **77** (1932) 1.
- [Hrn86] H. L. Harney *et al.*, Rev. Mod. Phys. **58** (1986) 607.
- [Ign75] A. V. Ignatyuk *et al.*, Sov. J. Nucl. Phys. **21** (1975) 255 [Yad. Fiz. **21** (1975) 485].
- [Kat78] S. K. Kataria *et al.*, Phys. Rev. C **18** (1978) 549.
- [Kau07] K. Banerjee *et al.*, Nucl. Instr. and Meth. A **580** (2007) 1383.
- [Kau09] K. Banerjee *et al.*, Nucl. Instr. and Meth. A **608** (2009) 440.
- [Kau12] K. Banerjee *et al.*, Phys. Rev. C **85** (2012) 064310.
- [Kel99] M. P. Kelly *et al.*, Phys. Rev. Lett. **82** (1999) 3404.
- [Kol04] V. M. Kolomietz *et al.*, Phys. Rep. **390** (2004) 133.
- [Kov05] P. K. Kovtun *et al.*, Phys. Rev. Lett. **94** (2005) 111601.

- [Kra40] H. A. Kramers, *Physica* **7** (1940) 284.
- [Kub57] R. Kubo, *J. Phys. Soc. Jpn* **12** (1957) 570.
- [Kub66] R. Kubo, *Rep. Prog. Phys.* **29** (1966) 255.
- [Kuh79] E. Kuhlmann, *Phys. Rev. C* **20** (1979) 415.
- [Kus98] D. Kusnezov *et al.*, *Phys. Rev. Lett.* **81** (1998) 542.
- [Lah07] S. Laha *et al.*, arXiv:hep-ph/0702086.
- [Lam32] H. Lamb, *Hydrodynamics*, 6th ed., Dover Publications, New York, 1932, sect. 364.
- [Lev82] L. P. Levy *et al.*, *Phys. Rev. Lett.* **48** (1982) 1011.
- [Li11] S. X. Li *et al.*, *Phys. Rev. C* **84** (2011) 024607.
- [Liu06] H. Liu *et al.*, arXiv:hep-ph/0609034.
- [Mac58] William M. MacDonald, *Phys. Rev.* **110** (1958) 1420.
- [Maj04] A. Maj *et al.*, *Nucl. Phys. A* **731** (2004) 319.
- [Mas09] H. Masui *et al.*, *Nucl. Phys. A* **830** (2009) 463c.
- [Mcf66] L. Mcfadden *et al.*, *Nucl. Phys.* **84** (1966) 177.
- [Mel11] D. Melconian *et al.*, *Phys. Rev. Lett.* **107** (2011) 182301.
- [Mor94] David J. Morrissey *et al.*, *Annu. Rev. Nucl. Part. Sci.* **44** (1994) 27.
- [Mye74] W. D. Myers *et al.*, *Ann. Phys. (NY)* **84** (1974) 186.
- [New81] J. O. Newton *et al.*, *Phys. Rev. Lett.* **46** (1981) 1383.
- [Nif90] H. Nifenecker *et al.*, *Annu. Rev. Nucl. Part. Sci.* **40** (1990) 113.

- [Orm96] W. E. Ormand *et al.*, Phys. Rev. Lett. **77** (1996) 607.
- [Pal10] Subrata Pal, Phys. Rev. C **81** (2010) 051601(R).
- [Pau71] P. Paul *et al.*, Phys. Rev. Lett. **27** (1971) 1013.
- [Pau94] P. Paul *et al.*, Annu. Rev. Nucl. Part. Sci. **44** (1994) 65.
- [Pra13] Pratap Roy *et al.*, Phys. Rev. C **88** (2013) 031601(R).
- [Pra16] Pratap Roy *et al.*, Phys. Rev. C **94** (2016) 064607.
- [Pul77] F. Puhlhofer, Nucl. Phys. A **280** (1977) 267.
- [Pyw79] R. E. Pywell *et al.*, Nucl. Phys. A **318** (1979) 461.
- [Qua17] N. Quang Hung *et al.*, Phys. Rev. Lett. **118** (2017) 022502.
- [Ram96] E. Ramakrishnan *et al.*, Phys. Rev. Lett. **76** (1996) 2025.
- [Rei81] W. Reisdorf *et al.*, Z. Phys. A **300** (1981) 227.
- [Rep64] J. D. Reppy *et al.*, Phys. Rev. Lett. **12** (1964) 187.
- [Rou13] P. C. Rout *et al.*, Phys. Rev. Lett. **110** (2013) 062501.
- [Sag98] H. Sagawa *et al.*, Phys. Lett. B **444** (1998) 1.
- [Sat09] W. Satula *et al.*, Phys. Rev. Lett. **103** (2009) 012502.
- [Sch07] T. Schaefer, Phys. Rev. A **76** (2007) 063618.
- [Sch09] T. Schaefer *et al.*, Rep. Prog. Phys. **72** (2009) 126001.
- [Sch82] K. H. Schmidt *et al.*, Z. Phys. A **308** (1982) 215.
- [Shu08] E. Shuryak, arXiv:0807.3033.

- [Sou16] Soumik Bhattacharya *et al.*, DAE-BRNS Symp. on Nucl. Phys. **61** (2016) 98
- [Sup07] S. Mukhopadhyay *et al.*, Nucl. Instr. and Meth. A **582** (2007) 603.
- [Sup12a] S. Mukhopadhyay *et al.*, Phys. Lett. B **709** (2012) 9.
- [Sup12b] S. Mukhopadhyay, PhD Thesis, University of Calcutta, 2014.
- [Ste50] H. Steinwedel *et al.*, Z. Naturforsch. **5a** (1950) 413.
- [Suz96] T. Suzuki *et al.*, Phys. Rev. C **54** (1996) 2954.
- [Tow10] I. S. Towner *et al.*, Phys. Rev. C **82** (2010) 065501.
- [Van13] Vandana Tripathi *et al.*, Phys. Rev. Lett. **111** (2013) 262501.
- [Ver75] J. D. Vergados, Nucl. Phys. A **239** (1975) 271.
- [Wie06] O. Wieland *et al.*, Phys. Rev. Lett. **97** (2006) 012501.
- [Wil56] D. H. Wilkinson, Phil. Mag. **1**(1956) 379.
- [Wil69] D. H. Wilkinson, *Isospin in Nuclear Physics*, North-Holland Publishing Company - Amsterdam, 1969.
- [Wil96] J Wilks, *The Properties of Liquid and Solid Helium*, Clarendon, Oxford, 1996.
- [Woj06] E. Wojcik *et al.*, Acta Physica Polonica B **37** (2006) 207.
- [Woj07] E. Wojcik *et al.*, Acta Physica Polonica B **38** (2007) 1469.
- [Zho13] C. L. Zhou *et al.*, Phys. Rev. C **88** (2013) 024604.
- [Zho14] C. L. Zhou *et al.*, Phys. Rev. C **90** (2014) 057601.